ADDITIVELY MANUFACTURED THERMITE-BASED ENERGETICS: CHARACTERIZATION AND APPLICATIONS

By

Kelsay Neely

Dissertation

Submitted to the Faculty of the

Graduate School of Vanderbilt University

In partial fulfillment of the requirements

For the degree of

DOCTOR OF PHILOSOPHY

in

Mechanical Engineering

May 8, 2020

Nashville, Tennessee

Approved:

Alvin M. Strauss, Ph.D.

Kevin C. Galloway, Ph.D.

Kelsey B. Hatzell, Ph.D.

Kenneth Frampton, Ph.D.

Kenneth Pence, Ph.D.

ACKNOWLEDGEMENTS

This dissertation is the culmination of several years of work. I'd like to thank my advisor Dr. Alvin Strauss for his guidance on my academic career, my professional career, and this project. Similarly, I'd like to thank Dr. Kevin Galloway for all of his feedback and for helping me develop as a researcher and as an academic. I also appreciate the rest of my committee, Dr. Ken Frampton, Dr. Ken Pence, and Dr. Kelsey Hatzell for their advice and feedback on my dissertation. I'd like to thank all of my lab mates, specifically my unwavering safety buddies Adam Jarrell, Connor Strawn, Lucas Wilkins, Ben Snyder, Brayden Terry, and Jake Matthews. Finally, I'd like to thank the Tennessee Space Grant Consortium for funding me as a NASA Space Grant Fellow, and the Naval Sea Systems Command (NAVSEA) for funding me and my work through the Naval Engineering Education Consortium (NEEC).

On a personal note, there are a lot more people I need to thank, way too many to mention here but I'll try. I couldn't have done this without the unwavering support of my friends. I'd like to thank Darren Tinker, Dylan Shane, Melissa, Tyler, and Bella Keagle, and Chase Mu for keeping me from constantly working all the time.

I have to acknowledge that I couldn't have done this without the extensive love and support of my family. I'm eternally grateful to Courtney Mason and Forrest Edens for their unwavering support and encouragement at all times. Finally, I could not have started this degree, let alone completed it, without the love and support of my parents, Bill and Janet.

TABLE OF CONTENTS

Page

ACKNOWLEDGEMENTS i

LIST OF TABLES vi

LIST OF FIGURES vii

CHAPTER

I. INTRODUCTION 1

Literature Review 1

Additive Manufacturing 2

Additive Manufacturing of Highly Viscous Materials 6

Reactive Material Architectures 13

Reactive Material Architecture Applications 17

II. ADDITIVELY MANUFACTURED REACTIVE MATERIAL ARCHITECTURES AS A PROGRAMMABLE HEAT SOURCE 22

Abstract 22

Introduction 22

Materials and Methods 24

Results 30

Discussion 32

Conclusion 38

Acknowledgements 38

Author Disclosure Statement 38

Reference 38

III. MULTI-MATERIAL ADDITIVELY MANUFACTURED COMPOSITE ENERGETICS VIA CONTINUOUS FILAMENT DIRECT INK WRITING 41

Abstract 41

Introduction 41

Methods and Materials....42
Results and Discussion....44
Conclusions....53
Acknowledgments....54
References....54
IV. SOLDERED COPPER LAP JOINTS USING REACTIVE MATERIAL ARCHITECTURES AS A HEAT SOURCE....57
Abstract....57
Introduction....57
Methods....58
Results and Discussion....62
Conclusion....64
Funding....64
References....65
V. ADDITIVELY MANUFACTURED REACTIVE MATERIAL ARCHITECTURES FOR EXOTHERMIC BRAZING....67
Abstract....67
Introduction....67
Methods & Materials....69
Results & Discussion....71
Conclusion....78
Acknowledgements....78
References....79
VI. CHEMICAL EQUILIBRIUM SIMULATIONS....81
Introduction....81
Tested Thermite Compositions....81
Adiabatic Flame Temperature and Reaction Rate....82
Phase Changes....89
Products....92
Conclusion....94

VII. CONCLUSIONS AND FUTURE WORK 95
Conclusions 95
Future Work 99
REFERENCES 101
APPENDIX A: G-CODE 105

LIST OF TABLES

Table Page

1. Table showing ASTM defined AM process categories, technology examples, and materials. Adapted from [2]. 2

2. Tested dimensions for architecture 2 as depicted in Figure 16b. Four iterations of architecture 2 were tested, with different total turns, length, width, and centerline spacing 29

3. Common materials and their joining temperatures[18,19,20] 37

4. Tested mass ratios of aluminum-based thermite and titanium-based thermite 43

5. Tested compositions and their measured reaction rates and standard deviations 48

6. Mass of thermite and its corresponding sample number. The masses range from 7.1 to 10.1 grams 71

7. Tested thermite compositions and their corresponding mass ratio, O/F ratio, and weight percent Fe_2O_3 82

LIST OF FIGURES

Figure Page

1. Schematic of the binder jetting process. Adapted from [3] 3
2. Schematic of a material extrusion process. Adapted from [6] 4
3. Schematic of material jetting. Adapted from [8] 6
4. Schematic illustration of direct ink writing techniques: a) continuous filament writing and b) droplet jetting. Adapted from [10] 7
5. Particle laden inks and the printing process. Adapted from [15] 8
6. Printing process of Lunar and Martian regolith simulant inks (LRS and MRS) and the resulting structures. Adapted from [16] 9
7. Contour crafting process. Reproduced from [18] 10
8. 3D printing concrete on a non-flat surface with arbitrary curvature and height variations. Adapted from [19] 11
9. Comparison between a non-optimized (a) and optimized (b) printing path. Adapted from [20] 12
10. Examples of full-scale builds from various concrete printing methods. A) D-Shape, b) contour crafting, and c) concrete printing. Adapted from [20] 13
11. a) Optical image of the 3D printing process for channels (left) and hurdles (right) composed of nanoparticle ink. Adapted from [22] 14
12. The Purdue University logo printed in a) ABS and b) Al/PVDF. C) The STL file used for printing. Adapted from [25] 16

13. Representations of a) CAD cross sections of port geometries, and b) corresponding 3D-printed propellant grains. Adapted from [27] 18
14. Diagram of exothermic brazing setup from NASA Skylab experiment. Adapted from [34] 20
15. a) Shear rate and viscosity data for the uncured thermite paste. b) Nozzle and tubing configuration for the syringe printing setup. e,d) Uncured printed thermite structures ... 26
16. Reactive material architectures, where a) is a linear architecture used to determine propagation speed, b) is used to test propagation of reaction perpendicular to direction of reaction, and c) is used to test propagation of reaction parallel to direction of reaction .. 28
17. Thermite reaction propagation rates for different cross sectional areas 30
18. a) Depicts adjacent thermite ignition initiation 2, taking place across 0.17s and b) two instances of adjacent ignition initiation in architecture 3 31
19. a) Schematic of a thermite joint setup. b) Side view of thermite created joint and c) top view of thermite created joint 35
20. Printed geometry showing the first material, the transition stage, and the second material from an a) overhead view, b) overall cross-sectional view, and c) individual cross-sections 44
21. Fluid behavior during the extrusion process, with the syringes on top and the cross section of extruded material below. The leftmost side is the initial state of the syringe, with extrusion progressing to the right. 45
22. Cross section of cured syringes, with a) showing the described edge phemonenon at the outlet, and b) showing the parabolic flow shape away from the outlet 46

23. Reaction rate vs Mass Fraction Binder for both the aluminum-based thermite and the titanium-based thermite, showing clearly exponential behavior 48

24. Reaction rate with respect to position for sample 1, showing a region of high reaction rates, then a region of lower reaction rates, and again a region of high reaction rates. The vertical dashed lines indicate the transition from on composition to another..... 50

25. Reaction rate with respect to position for sample 2, showing a region of high reaction rates, then low reaction rates, and then again high reaction rates. The vertical dashed lines indicate a transition from one region of thermite to another 52

26. Measured temperature-mass relationship for printable thermite formulation 60

27. Setup for samples joined with thermite, consisting of two copper samples in a lap joint, with solder between the samples and thermite on the top surface of the uppermost copper samples.....61

28. Load at failure for sample joints and control joints. The experimental samples are labeled 1-8 for future reference 62

29. Broken lap joint samples showing the solder coverage. The control sample can be seen in a), with samples 1, 3, and 6 shown in b), c), and d) respectively 63

30. Schematic of joint setup showing the copper fitting over the copper pipe, with the thermite placed over the fitting, b) top view of thermite structure, and c) isometric view of thermite structure.....70

31. Printed thermite wall, with dimensions 10x0.5x3 cm.....72

32. Second high aspect ratio print, immediately before collapse 73

33. Cylindrical prints created using a) the method of sequential uncured prints and b) the print method of sequential cured prints 74

34. Select pipe joining samples. There is some slag and discoloration at and near the joint, caused by the thermite reaction....76
35. Maximum tensile load before failure for all tested pipe joints....77
36. Adiabatic flame temperature (K) with respect to weight percent Fe_2O_3. The diamond markers indicate experimental conditions....83
37. Adiabatic flame temperature (K) with respect to O/F ratio. The diamond markers indicate experimental conditions....84
38. Reaction rate (mm/s) with respect to weight fraction CaSO4. The diamond markers indicate specific cases....85
39. Adiabatic flame temperature (K) with respect to reaction rate (mm/s) for a range of O/F ratios and fixed weight percent iron oxide. The diamond markers indicate specific tested cases....86
40. Reaction rate (mm/s) with respect to O/F ratio, with the diamond markers indicating experimental measurements....87
41. Adiabatic flame temperature (K) with respect to reaction rate (mm/s) for a range of O/F ratios and fixed weight percent iron oxide. The diamond markers indicate specific tested cases....88
42. Mass fraction of species for varying O/F ratios and varying weight percent Fe_2O_3, with a) depicting Al, b) AlO, c) Al_2O, and d) Al_2O_3 (L)....89
43. Mass fraction of species for varying O/F ratios and varying weight percent Fe_2O_3, with a) showing Fe and b) showing Fe(L)....90
44. Adiabatic Flame Temperature (K) with respect to O/F ratio and weight percent Fe_2O_3...91

45. Predicted species and their corresponding mass fractions for each experimentally tested thermite mixture.....93

CHAPTER 1: INTRODUCTION

The terms reactive or energetic materials describes a class of material consisting of two or more nonexplosive solids that release large quantities of chemical and kinetic energies upon ignition. This dissertation centers around a class of reactions called thermite reactions. A thermite reaction is a reduction-oxidation (redox) reaction, characterized by a high reaction temperature, low gas production, and the production of molten slag. Notably, this reaction does not require atmospheric oxygen for combustion. Most thermite formulations are insensitive to corrosion, friction, spark, shock, contaminants, moisture, and variations in composition [1]. A common example of a thermite reaction, as seen below in equation 1.1, involves aluminum acting as the reducing agent for an iron oxide fuel.

$$Fe_2O_3 + 2Al \rightarrow 2Fe + Al_2O_3 \quad (1.1)$$

This reaction produces large amounts of heat, molten iron and aluminum oxides. Thermite reactions often reach temperatures of several thousand degrees Celsius [1].

The same reaction is the basis of a novel reactive material paste, the subject of interest for this dissertation. This body of work details the creation of the paste, its printing parameters, its reaction characteristics, and its joining applications.

Literature Review

The work presented here is highly interdisciplinary in nature: it touches on topics ranging from additive manufacturing techniques, highly viscous fluid flow, energetic materials, chemical

equilibrium analysis, and metal joining techniques. Consequently, background information is required for each of these fields.

Additive Manufacturing

Additive manufacturing (AM) is classified by process methodology, not necessarily by material type. Table 1 shows the ASTM defined AM technologies.

Process Categories	Technology	Materials
Binder Jetting	3D Printing Ink-Jetting S-Print M-Print	Metal Polymer Ceramic
Direct Energy Deposition	Direct Metal Deposition Laser Deposition Laser Consolidation Electron Beam Direct Melting	Metal Powder Metal Wire
Material extrusion	Fused Deposition Modeling	Polymer
Material Jetting	Polyject Ink-jetting Thermojet	Photosensitive polymers
Powder Bed Fusion	Selective Laser Sintering Selective Laser Melting Electron Beam Melting	Metal Polymer Ceramic
Sheet lamination	Ultrasonic Consolidation Laminated Object Manufacture	Hybrid Metal Ceramic
Vat photopolymerization	Stereolithography Digital Light Processing	Photopolymer Ceramic

Table 1 - Table showing ASTM defined AM process categories, technology examples, and materials. Adapted from [2].

These processes represent a wide array of bonding techniques and materials. However, for this work, the most relevant and analogous techniques are binder jetting, material extrusion, and material jetting.

Binder Jetting

Binder jetting is an additive manufacturing process where a liquid binding agent is selectively deposited onto a powder bed to create a final part. This process can be seen in Figure 1. A layer of powder is spread across a print bed. A printhead selectively deposits binder, creating a layer of the part. The next layer of powder is then spread across the print bed. The binding agent is then deposited again, and the process repeats until the full part is created.

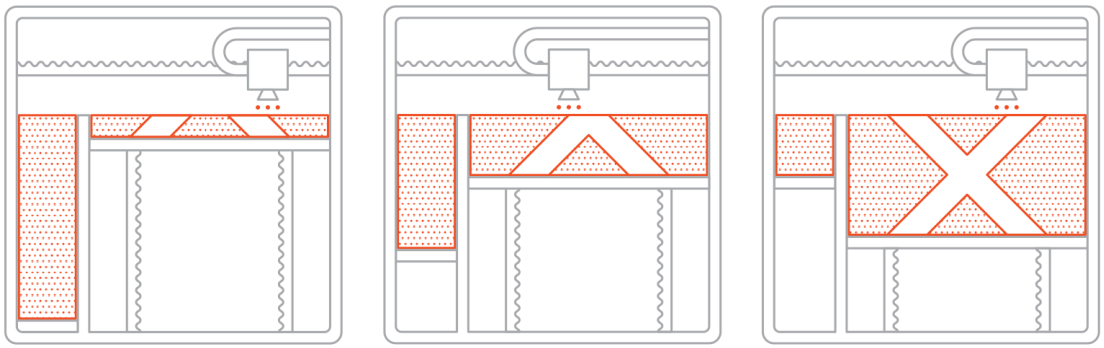

Figure 1 - Schematic of the binder jetting process. Adapted from [3].

Binder jetting is capable of creating parts out of a variety of materials, including metals, polymers, and ceramics. For polymers, the part is complete after the initial printing process; no additional processing is necessary. For metals and ceramics, an additional processing step is

necessary after the initial printing phase, generally a sintering or pressing phase to achieve high density materials.

In addition to standard polymer part manufacturing, binder jetting of metals and ceramics have seen application in the dental industry and in the creation of metal-ceramic hybrids [4-6].

Material Extrusion

Material extrusion is often the technique thought of when discussing 3D printing. Fused deposition modeling (FDM) consists of a thermopolymer filament being actuated through a heated nozzle and then deposited on a build plate. The print head deposits the filament into the shape of the manufactured part layer by layer. There is a wide variety of polymers available for FDM printing, but common material options include polylactic acid (PLA), acrylonitrile butadiene styrene (ABS), Nylon, polyether ether ketone (PEEK), and thermoplastic polyurethane (TPU).

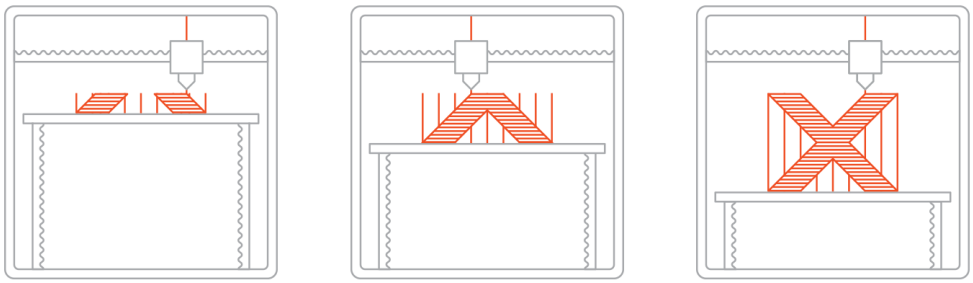

Figure 2 – Schematic of a material extrusion printing process. Adapted from [6]

Since FDM was invented in the 1980s, it's a mature field with an assortment of unique materials. A common variation on traditional FDM is to use filaments with high mass proportions of metal or ceramic polymers. These parts are created using an FDM printer, and then undergo post-processing. The Virtual Foundry recommends either polishing or sintering parts printed from their filament immediately after printing [7]. Markforged and Desktop Metal both recommend an intermediate step to remove the polymer before sintering.

Material Jetting

Material jetting consists of a printhead (similar to a standard inkjet printhead) depositing a droplet of photosensitive material onto a print surface and then immediately curing and solidifying the droplet with an ultraviolet light. This creates a part built first by droplets and then by layers. The materials most often used for material jetting are photosensitive polymers, but any particle, like metal or ceramic particles, suspended in a photosensitive polymer could theoretically be manufactured via material jetting.

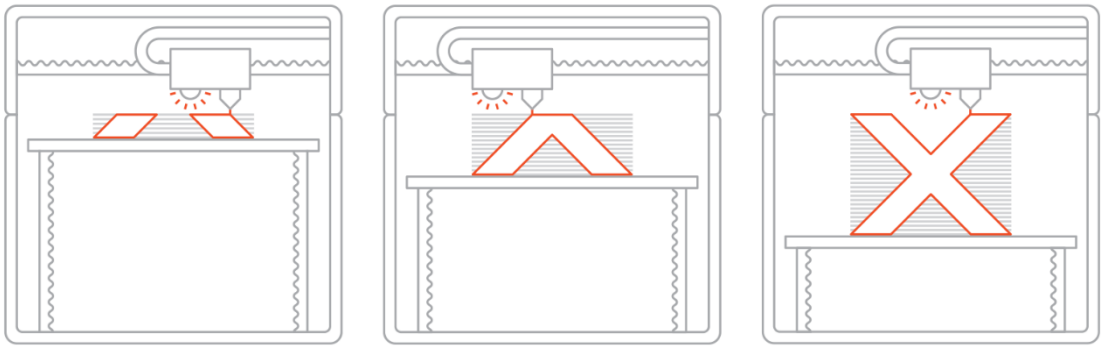

Figure 3 - Schematic of material jetting. Adapted from [8].

Additive Manufacturing of Highly Viscous Materials

All of the techniques discussed thus far are commercially accepted AM methodologies, and are easy for an end-user to purchase and operate. However, there exists extensive research into the additive manufacturing of highly viscous materials, like pastes and inks. These techniques often use a variation of a syringe (or other reservoir) and a nozzle to extrude the material, which then cures into a hardened state. This is most analogous to FDM printing, but comes with its own challenges and advantages and is thus considered completely separate for this work.

Direct Ink Writing

Direct ink writing is a manufacturing method consisting of a computer controlled stage and an ink-deposition nozzle that deposits patterns or architectures onto a bed or substrate [9]. This is a broad category that includes both droplet- and continuous filament-based methods.

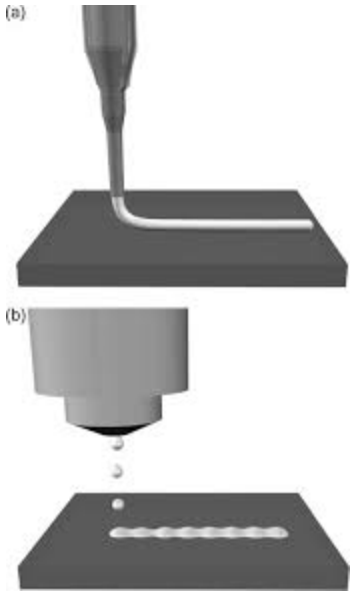

Figure 4 - Schematic illustration of direct ink writing techniques: a) continuous filament writing and b) droplet jetting. Adapted from [10].

In 2006, Lewis et al. created a series of colloidal inks capable of creating fine features and geometries (200 µm) using continuous filament writing techniques. These inks were also capable of creating large structures (>5mm in size) that exhibited gap spanning characteristics of 10mm [10]. These spanning characteristics are also seen in Ahn et al. for planar and 3D printing of conductive inks [11]. Direct ink writing has been used to create lithium ion batteries, to embed soft somatosensitive actuators in a 3D printed structure, and to print microfluidic circuitry [12-14].

Direct Ink Writing of Ceramics and Metals

Jakus et al. developed a method of 3D printing highly viscous inks into green-body structures that undergo a thermochemical transformation into sintered metallic parts. Metal-oxide and

metal powders are mixed with polylactic-co-glycolic acid (PLGA) and a solvent, creating a printable ink. These inks can be 3D printed under ambient conditions via extrusion and can create millimeter- and centimeter- scale structures. The resulting green bodies can be transformed into metallic structures via sintering [15]. The structures created through this process are highly complex and robust, as seen in Figure 5.

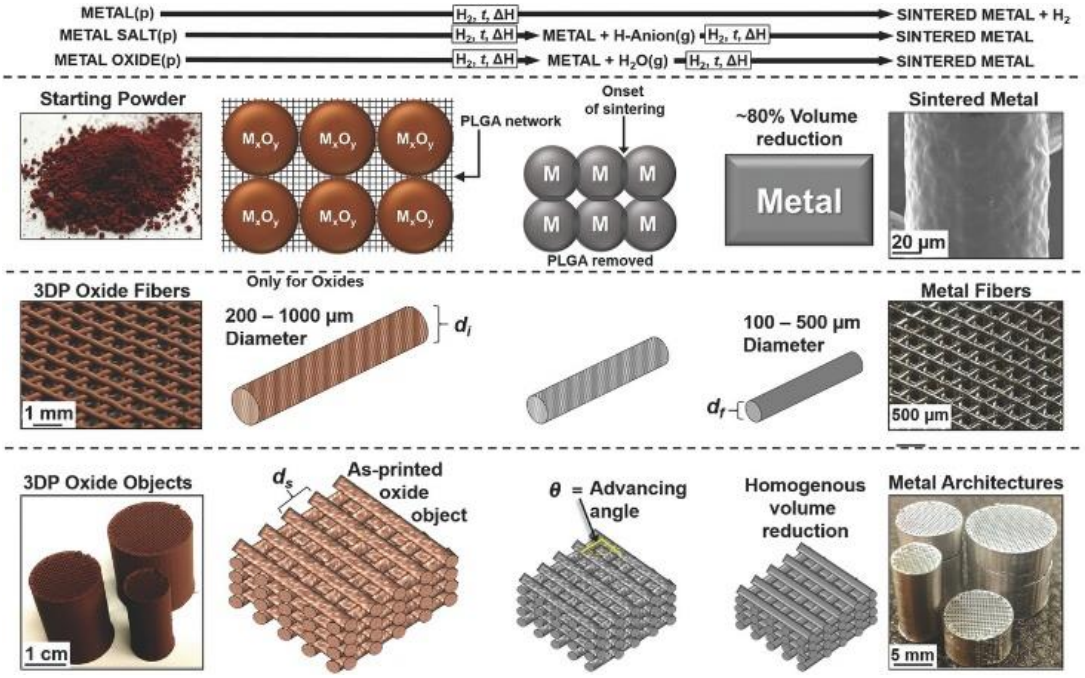

Figure 5 - Particle laden inks and the printing process. Adapted from [15]

This process has also been shown to work with Lunar and Martian regolith simulant inks (LRS and MRS, respectively). The PLGA is dissolved in a solvent, dichloromethane (DCM), and then Lunar or Martian regolith is mixed into the dissolved polymer. The resulting ink is printed using an ink-based technique, and then the resulting structured is sintered into a finished structure [16].

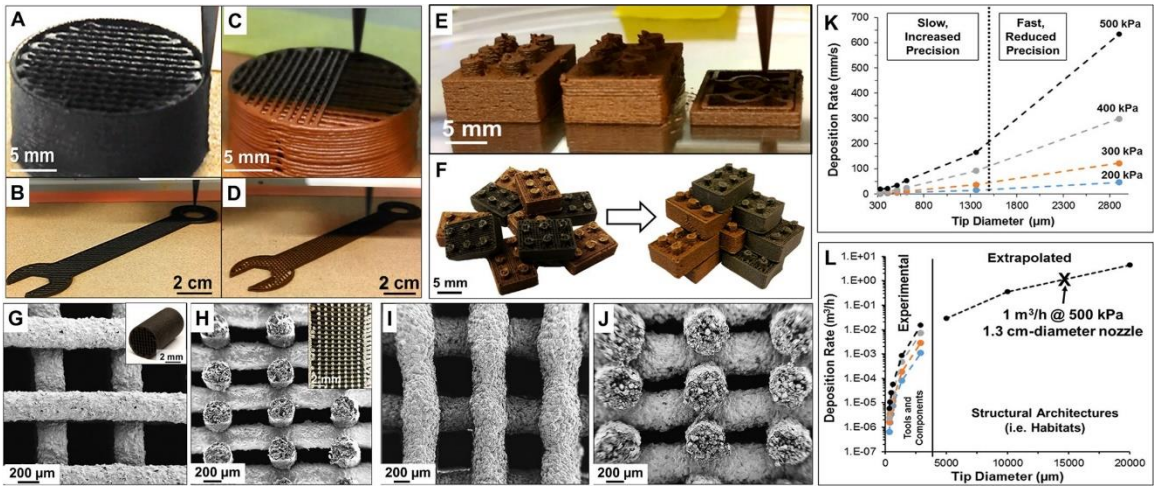

Figure 6 - Printing process of Lunar and Martian regolith simulant inks (LRS and MRS) and the resulting structures. Adapted from [16].

Direct ink write has also been used to create ceramic structures. Droplet-based techniques using wax-based colloidal inks have been used to produce ceramic structures with high aspect ratio walls, while continuous filament techniques have resulted in millimeter scale ceramic structures Lewis et al. have also shown that the green body produced by solvent-based colloidal fluids still contain enough polymeric binder to facilitate post-deposition handling while still being rapidly removed during heat treatment [17].

Concrete

In regards to printing methodology, some 3D printing concrete techniques are most similar to continuous filament direct ink writing. However, 3D printing concrete operates on a significantly larger scale than other direct ink write processes due to the nature of the applications. An early example of a continuous filament process in concrete was in 2004, with a contour crafting (CC) method.

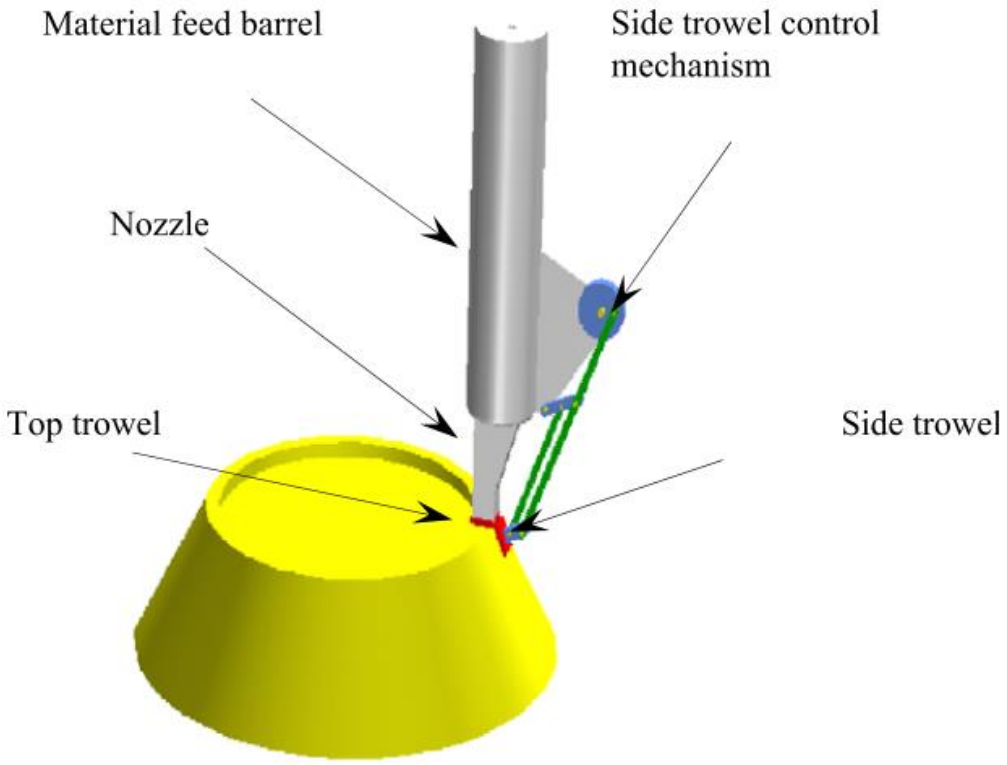

Figure 7 - Contour crafting process. Reproduced from [18]

The contour crafting process, as shown in Figure 7, consists of an extrusion process through a nozzle and a smoothing process with an attached trowel. The trowel is used to smooth the surfaces, which is necessary in a large scale process. Any surface defects or mass-related displacement will alter the placement of the next layer. A smoothing process ensures that the previous layer has a good printing surface for subsequent layers. This method could be used to rapidly create large-scale habitats and houses [18].

Unlike contour crafting, recent advancements in concrete 3D printing use in-process monitoring to ensure layer adhesion and print behavior instead of using a trowel to ensure adequate print

surfaces. Wolfs et al. use a real-time height measurement and feedback system to account for non-flat surfaces and to account for the printed structure deforming under its own mass. This results in uniform layers and eliminates any printing defects caused by excess nozzle height or insufficient nozzle height [19].

Figure 8 - 3D printing concrete on a non-flat surface with arbitrary curvature and height variations. Adapted from [19].

Another advance in 3D printing concrete comes through optimization of path-planning for 3D printing. Concrete is constantly extruded through the nozzle during the printing process, unlike FDM methods or polymeric ink-writing where quick starts and stops of material are possible. Because of this, traditional slicers are generally not optimized for a continuous flow. With more advanced slicing software, optimized printing paths are now able to be generated for concrete printing, resulting in stronger parts [20,21].

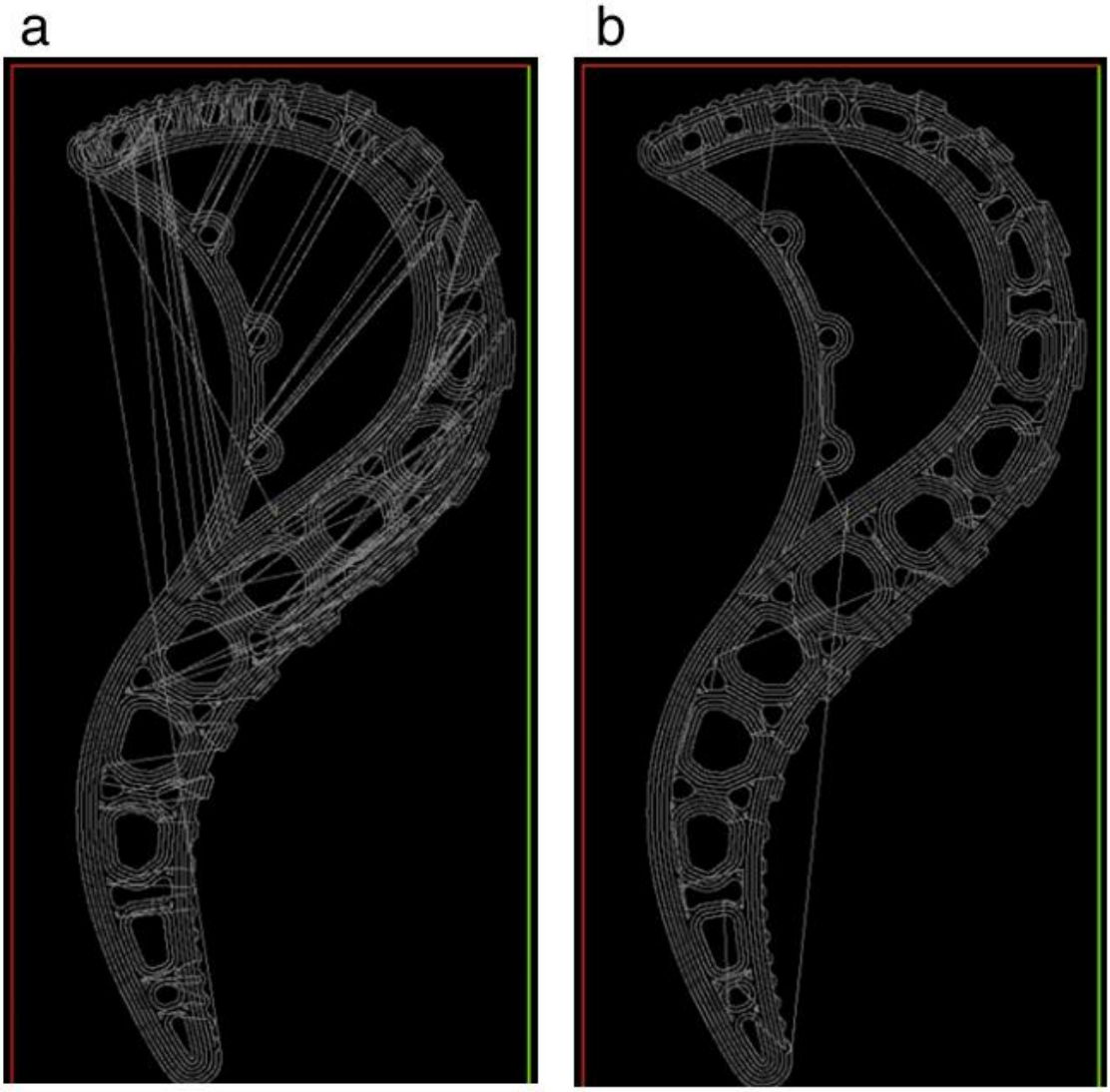

Figure 9 - Comparison between a non-optimized (a) and optimized (b) printing path. Adapted from [20]

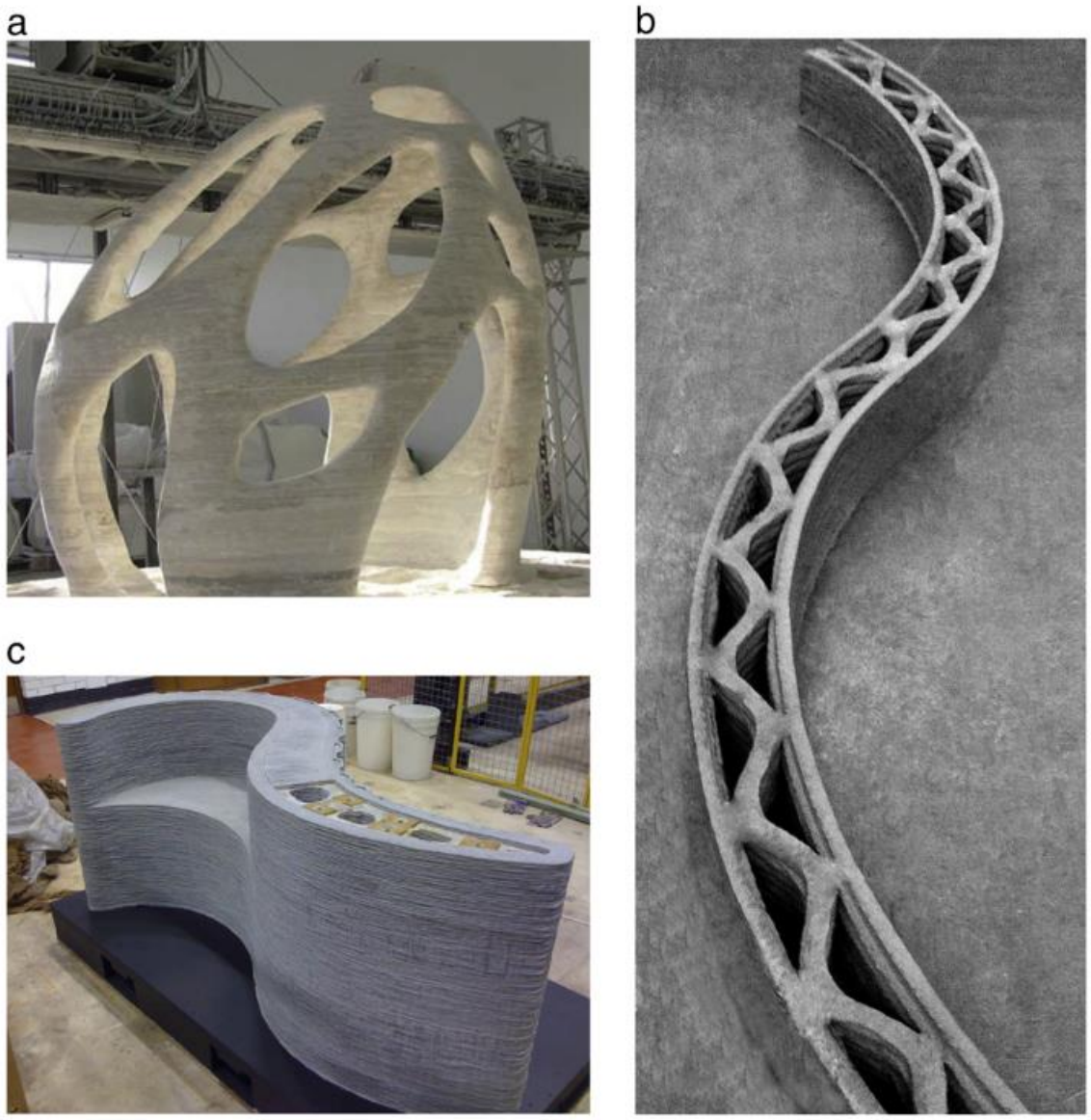

Figure 10 - Examples of full-scale builds from various concrete printing methods. A) D-Shape, b) contour crafting, and c) concrete printing. Adapted from [20].

Reactive Material Architectures

Reactive, or energetic, materials are defined as materials that store a high amount of chemical energy. This typically includes explosives, pyrotechnics, propellants, and fuels. The precision of additive manufacturing technology can be combined with reactive materials to create reactive

material architectures. Reactive material architectures (RMA's) are structures that can control reaction characteristics, like reaction rate and heat deposition, through internal voids and geometries in addition to changes in chemical composition. In a recent study, Sullivan et al. created thermite-based RMA's by 3D printing silver substrate architectures and depositing 26 and 156 µm thick nanothermite layers via electrophoretic deposition. These architectures are submillimeter in scale and has propagation velocities ranging from 7 to 35 m/s for thin films (26 µm) and 50-140 m/s for thick films (156 µm). Most notably, these architectures were able to successfully control reaction velocity through the creation of two geometries, hurdles and channels.

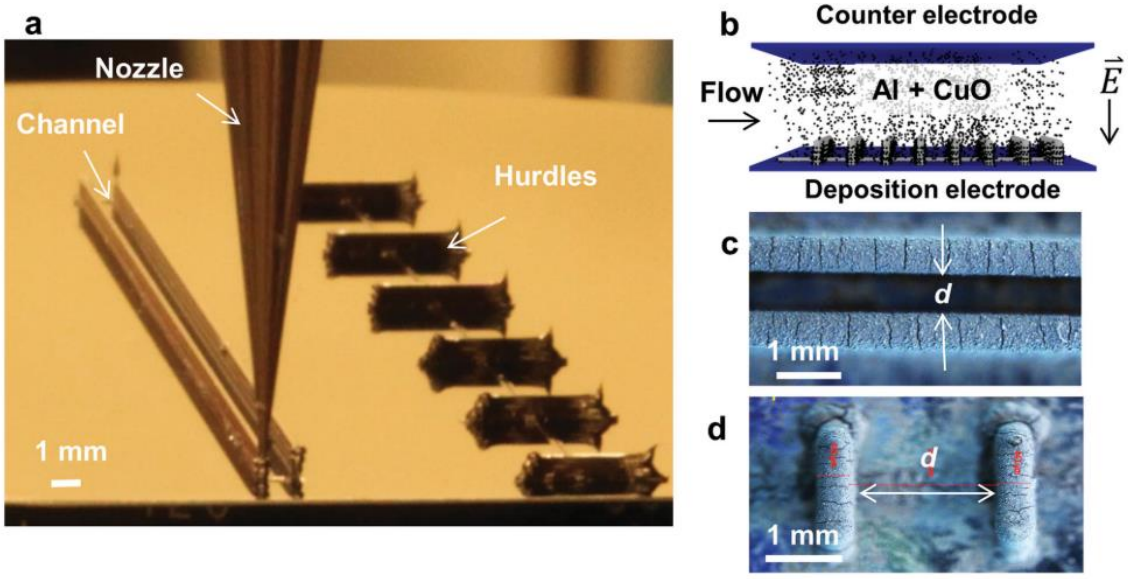

Figure 11 - a) Optical image of the 3D printing process for channels (left) and hurdles (right) composed of nanoparticle ink. Adapted from [22].

For channel-based RMA's, the decreasing the spacing increases the propagation velocity. The spacing could be altered to produce a peak propagation velocity of two- to three-times greater

than the baseline value. Hurdle-based RMA's showed the opposite effect, where increasing the spacing increases the propagation velocity, once again resulting in peak propagation values two- to three-times higher than the baseline velocity [22].

Murry et al. showed an interesting extension of inkjet printing techniques to create two-component additively manufactured nanothermite structures. Two inert colloidal suspensions of nanoaluminum and nanocopper (II) oxide in dimethylformamide with polyvinylpyrrolidone were sequentially deposited on a substrate using piezoelectric inkjet printing. The two materials were deposited such that the inks were adjacent and overlapping, resulting in in situ mixing of the materials. These samples reached reaction temperatures and reaction speeds comparable to samples printed from a single nozzle, thereby showing that in situ mixing is a viable technique for future energetic deposition. This allows for safer material handling, since the components are largely inert before mixing, and allows for the development of more sensitive energetic materials previously deemed unsuitable for inkjet printing [23].

Another ink-based method was developed by Ruz-Nuglo et al. using a fluropolymer based ink. The ink was developed with micron and nanoscale aluminum as the fuel. These ink traces were printed using direct ink writing using a pen technique, and resulted in material with combustion velocities of 30 ± 3 mm/s (micron scale aluminum) and 32 ± 2 mm/s (nanoscale aluminum). This indicates that the combustion rates and energy deposition can be tailored through architectures [24].

In addition to ink-based methods, there have been reactive material architectures created using filament-based techniques. Fleck et al. created a fluoropolymer based energetic to be used in fusion based material extrusion. The filament was composed of a polyvinylidene fluoride (PVDF) binder with a 20% mass loading of aluminum. This filament was then printed in a

commercially available printer, Makerbot Replicator 2X, and resulted in comparable reactivity and burning rates when compared to a non-printed energetic [25].

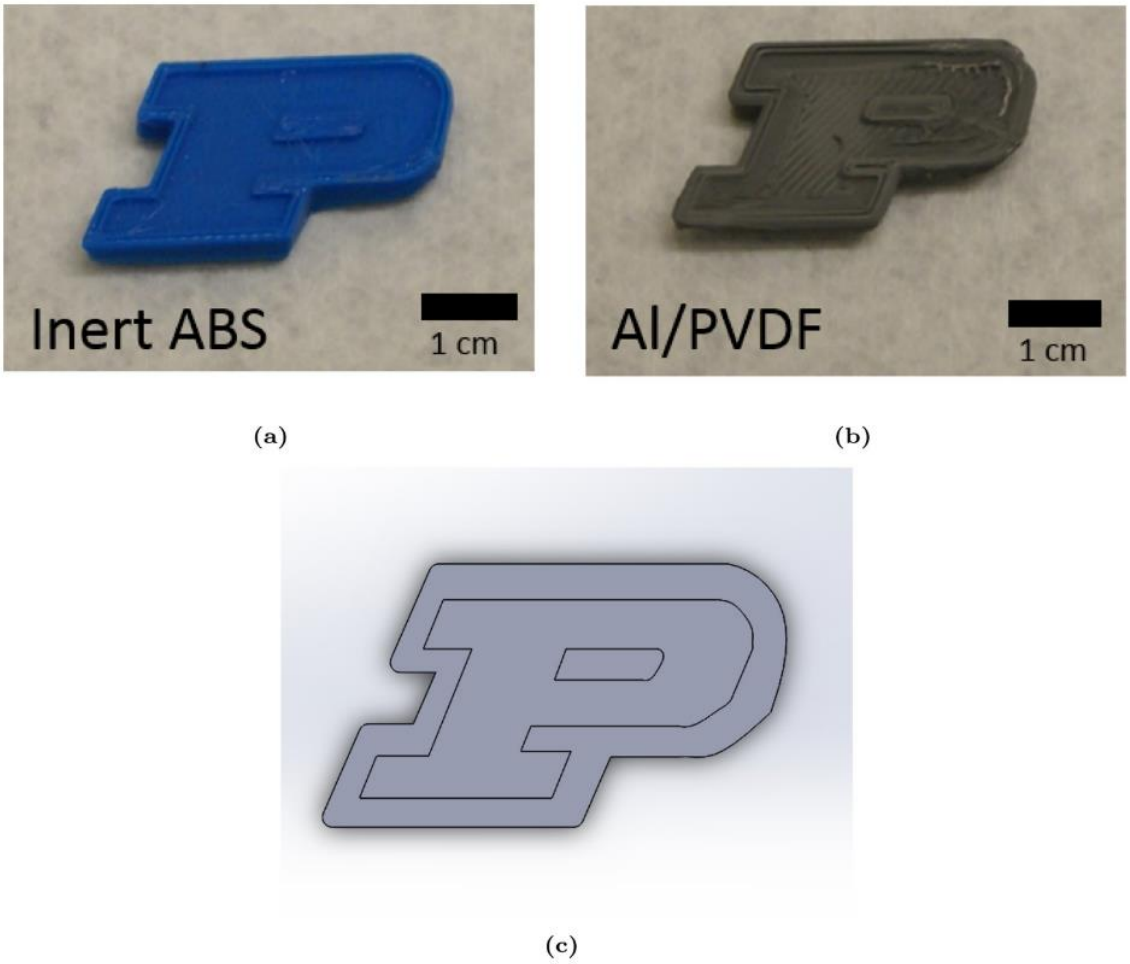

Figure 12 - The Purdue University logo printed in a) ABS and b) Al/PVDF. C) The STL file used for printing. Adapted from [25].

These results are significant because they significantly decrease the manufacturing complexity associated with RMA's. With a reactive filament, structures can be printed on a commercially

available desktop 3D printer, and structures can be created using commercially available slicing technology.

Reactive Material Architecture Applications

3D Printed Rocket Motors

An extension of RMA's is to create rocket motors. The concept of 3D printing rocket motors is not new; in 2015 Huang et al. detailed the electrospray deposition of energetic polymer nanocomposites with high mass particle loadings as a prelude to 3D printing rocket motors [26]. However, recent rapid developments in ink-based printing have led to similar developments in additively manufactured rocket propellant. In 2018, Chandru et al. created a propellant ink composed of aluminum perchlorate as the oxidizer, ferric oxide as a catalyst, hydroxyl-terminated polybutadiene (HTPB) as a fuel/binder, dioctyl adipate (DOA) as a plasticizer, and isophorone di-isocyanate (IPDI) as a curing agent. This mixture was extruded via a nozzle to create different 3D printed propellant grains [27].

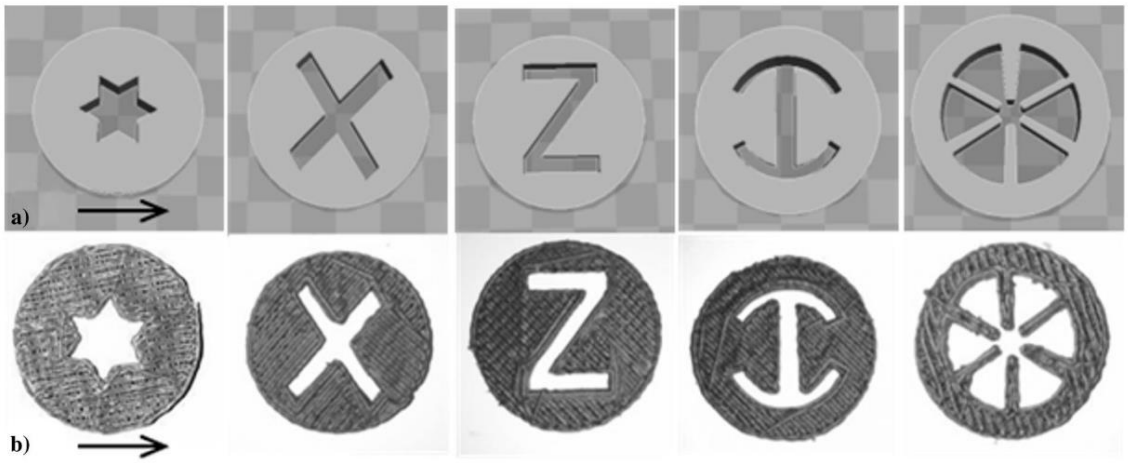

Figure 13 - Representations of a) CAD cross sections of port geometries, and b) corresponding 3D-printed propellant grains. Adapted from [27].

Recent work has shown the ability to print very high viscosity mixtures through a vibration assisted printing technique. Ultrasonic vibrations of a frequency of 30.3 kHz and a peak to peak amplitude of 8 μm were used to induce the flow rate of the propellant at the nozzle tip. This was used to print ammonium perchlorate composite propellants at 85% solids loading using HTPB and a UV-curable polyurethane binder. The resulting prints had some porosity due to gas generation, but overall the system can produce strands of composite propellant with high solids loading without additional processing chemicals. Additionally, complex grain geometries that were previously not possible due to the high viscosities are now possible [28].

Reactive Material Joining Applications

The traditional example of joining with reactive materials is thermite welding. A thermite reaction is a reduction-oxidation (redox) reaction, characterized by a high reaction temperature, low gas production, and the production of molten slag. Thermite rail welding was popularized in

the early 1900s as a method to quickly join and repair rail ties. The process remains relatively unchanged today. A crucible filled with a thermite composed of aluminum and iron oxide is suspended over the rail ties. The thermite mixture is ignited, creating molten iron and slag. The slag, composed primarily of aluminum oxide, floats to the surface, while the molten iron flows out the bottom of the crucible and onto the joint. The iron then solidifies, forming a new joint [29]. A similar process can be used to join large electrical cables, except the thermite is composed of aluminum and copper oxide. This mixture results in molten copper and slag, with the molten copper flowing down and forming the joint [30].

Another joining method related to reactive materials is exothermic brazing. Exothermic brazing using the heat generated from a solid-state or near solid-state reaction, like thermite, to melt a filler material for joining processes [31]. Exothermic brazing has previously been used to join hydraulic aircraft fittings, as well as underwater and in-space [32-34].

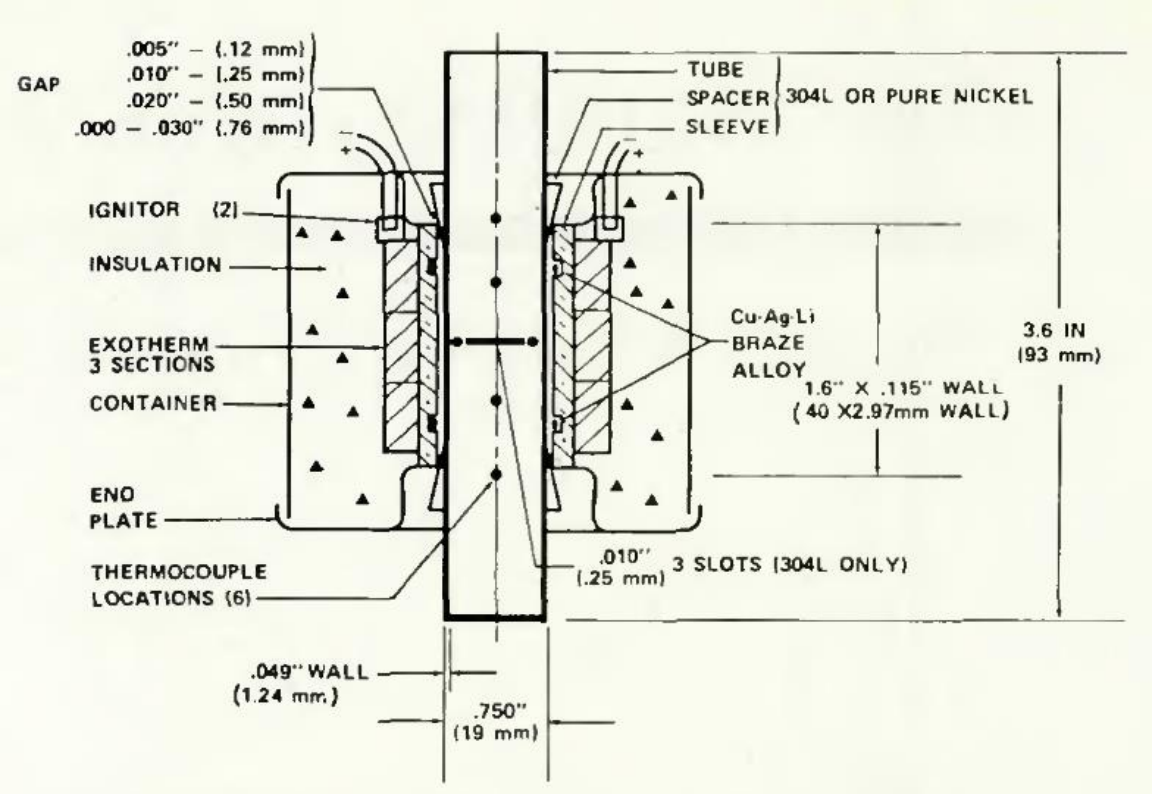

Figure 14 - Diagram of exothermic brazing setup from NASA Skylab experiment. Adapted from [34].

As seen in Figure 14, exothermic brazing traditionally required fixturing to hold the energetic around the joint. This adds a level of complexity for exothermic brazing.

However, with reactive material architectures, the fixturing formerly needed for exothermic brazing can be eliminated. Reactive material architectures can provide tailored heat deposition around a joint without the need for a skilled operator or fixturing. Additive manufacturing can create unique structures either through material deposition or direct ink writing techniques. These techniques are currently used in conjunction with energetic materials to create propellant technologies, but there are no applications in exothermic brazing. There exists a need for a low-cost, additively manufactured energetic capable of tailored heat deposition for joining. This

work details a novel solution, showing the properties of several thermite-based reactive material pastes, their printing properties, architecture specific behaviors, reaction rate, and heat deposition properties with respect to joining.

CHAPTER 2: ADDITIVELY MANUFACTURED REACTIVE MATERIAL ARCHITECTURES AS A PROGRAMMABLE HEAT SOURCE

The following work was previously published in *3D Printing and Additive Manufacturing* in Volume 6, issue 4.

Abstract

Until recently, the reactive properties of energetic materials have traditionally been tuned through chemical composition. However, with the emergence of additive manufacturing (AM) technology, the reaction can also be tuned through the construction of custom shapes known as reactive material architectures (RMA). In this work, we present the development and empirical evaluation of a thermite paste tuned for additively manufacturing reactive material architectures. The resulting architectures were ignited and recorded using a high speed camera to determine the influence of the architectural features on the speed of reaction and the ability of the reaction to jump to neighboring architectures. Additionally, in a constructive application, a sample lap joint was created using AM thermite architectures to demonstrate joining possibilities. The reaction characteristics were successfully shown to be controllable via architectures, which creates a wide range of opportunities for both constructive and destructive engineering applications.

Introduction

Advances in additive manufacturing technology have created a wide range of new applications including printing food for nutritional control[1], bioprinting of organs[2], and printing low-cost flexible sensors[3]. Traditional 3D printing has primarily been utilized for rapid prototyping in both polymers and metals. Recent developments in additive manufacturing have advanced the

concept of 4D printing[4], which introduces a time dependent component to a printed structure. A 4D printed structure has the ability to change shape or perform an action in response to a specific stimulus. Recent work by Tibbits et al and Raviv et al created structures that were printed out of a rigid polymer and a hydrophilic polymer that expands when in contact with water, creating parts that asymmetrically swell and self-assemble.[4,5] Similarly, structures have been printed using shape memory polymers that allow for temperature activated shape changes.[6] Outside the realm of stimuli dependent shape changes, there exists other 4D printing concepts and applications. A common biomaterials application aims to create a biocompatible scaffold that eventually undergoes a planned degradation, as seen in bone tissue engineering[7] and in other medical applications.[8]

One emerging application of additive manufacturing inspired by the stimulus-dependent response of 4D printing builds on a relatively old technology – thermite – where the precision of additive manufacturing is harnessed to create custom thermite shapes known as reactive material architectures (RMAs).[9] A thermite reaction is a highly exothermic redox reaction between a metal and metal oxide. This generates a large amount of energy and produces slag and an elemental metal. The traditional thermite reaction between iron oxide and aluminum is $Fe_2O_3 + 2Al \rightarrow 2Fe + Al_2O_3$. This reaction requires an ignition temperature of approximately 1650° C (typically burns at approximately 2200°C) and generates aluminum oxide slag and molten iron.[10] This specific formulation has traditionally been used in the rail road industry to weld tracks, where the molten iron generated by the thermite reaction flows into a void between rails, resulting in a new joint.[11]

Reactive material architectures enable a unique ability to control the reaction using internal voids and geometries in addition to changes in chemical composition. In recent work,

Sullivan et al. created thermitic RMAs by 3D printing silver substrate architectures and depositing 26 μm and 156 μm thick thermite layers using electrophoretic deposition. This approach can produce sub-millimeter scale architectures with architecture spacing on the scale of 10 mm and propagation velocities ranging from 7-35 m/s for thin films (26 μm) and 50-140 m/s for thicker films (156 μm). These architectures were able to successfully control the reaction velocity through material spacing.[9] Inkjet printing has also emerged as a method to create architectures on the scale of 100s-1000s of nanometers[12] using nanoaluminum and nanocopper (II) oxide. While Sullivan et al and Murray et al have presented technological demonstrations of RMAs, the proposed methods operate at limited scales and can only deposit small amounts of thermite, thus limiting the amount of reactive material energy that can be integrated into a structure. There has been work utilizing more traditional 3D printing methods on a macroscale. Ruz-Nuglo et al and Fleck et al have both shown success in printing fluoropolymer based reactive materials, creating structures at the macroscale (>0.5mm). These works demonstrate macroscale printing, but both require polymer synthesis techniques as well as refined filament creation techniques to avoid unintended ignition[13,14].

This work explores a new macroscale reactive material formulation and its applications in the joining of materials. We detail the development and characterization of a thermite paste suitable for additively manufacturing RMAs and demonstrate a constructive application where a RMA was ignited to join a lap joint.

Materials and Methods

The goal of this work is threefold: first, to develop and characterize a curing thermite paste and determine its printability; second, to evaluate the chemical reaction of a series of simple RMAs;

and third, present a use-inspired application of the RMA to harness the energy dense material for constructive purposes.

Creation of a Curing Thermite Paste

The thermite paste is composed of iron oxide (Fe_2O_3), aluminum powder, and calcium sulfate hemihydrate ($CaSO_4 \cdot 0.5\ H_2O$)—gypsum powder–in a 3:2:2 mass ratio. The iron oxide particles and aluminum particles are 30 microns in size, both supplied by Alpha Chemicals. Once the dry powder is thoroughly mixed, water is added in a ratio of 1.8 mL of water per gram of mixed powder. Water activates the gypsum powder binder, which immediately begins to cure. To slow the curing process, less than 0.1% by weight of tartaric acid is dissolved into the water before mixing. Tartaric acid is a known gypsum plaster retardant, and must be added to extend the working life of the paste.[15] Once the paste is mixed, there is approximately 45 minutes of working time before the mixture is too viscous to print. The exact cure time depends on ambient temperature, water temperature, and volume of paste. Generally, cooler temperatures and larger volumes result in longer curing times.

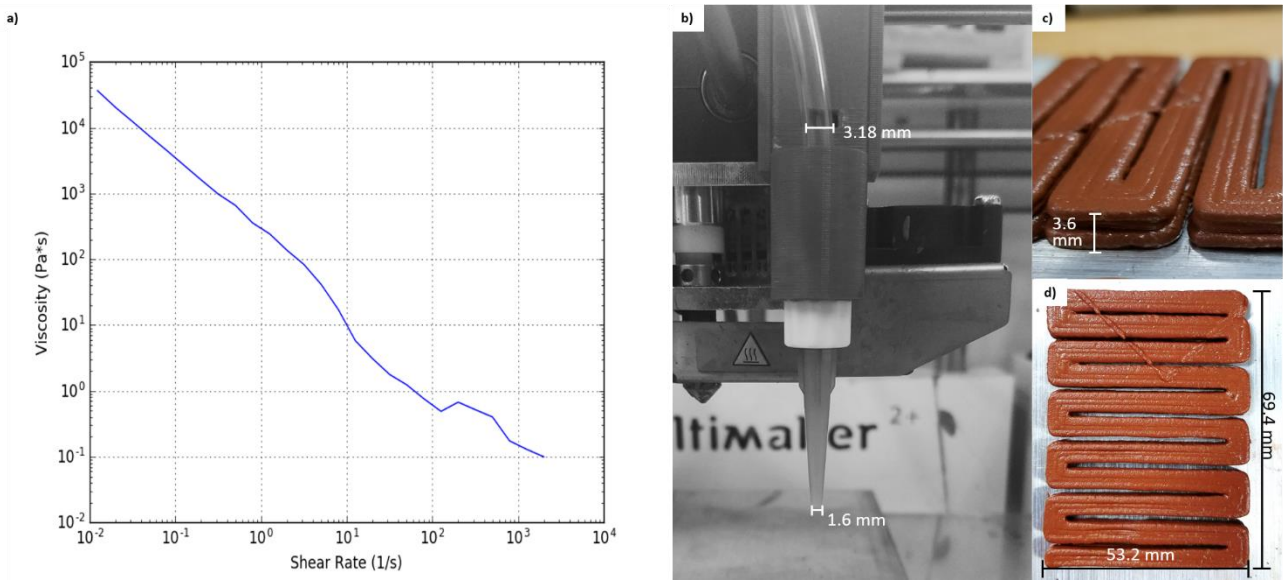

Figure 15 – a) Shear rate and viscosity data for the uncured thermite paste. b) Nozzle and tubing configuration for the syringe printing setup. e,d) Uncured printed thermite structures

Printing Parameters

The printing parameters depend greatly on viscosity. Figure 15a shows the viscosity profile of the thermite paste, which was tested using a stress controlled rheometer (TA-DHR3) in a 40 mm parallel plate configuration. The gap was 1 mm, and the shear rate swept from 2000 1/s to 0.01 1/s. To control for the effects of curing on the rheology, samples were tested immediately after creation. Each shear sweep took no longer than 16 minutes. The shear rate at the nozzle is calculated to be approximately 224 1/s, which corresponds to a viscosity of 0.64 Pa·s. Overall, the paste exhibits viscosity characteristics favorable for additive manufacturing, with the material holding its shape after extrusion but before curing.

The thermite mixture was printed using the Discov3ry 1.0, a syringe-based paste printing process by Structur3D Printing (Kitchener, ON, Canada) that was attached to an Ultimaker 2+ and used in place of the built-in extrusion system. The paste was loaded into a syringe and the plunger of

the syringe was depressed at a constant rate, moving the paste through .0125 inch inner diameter tubing and then extruding through a 1.6mm diameter nozzle (14 gauge) held in the Discov3ry. The deposited paste width, as coded and printed, was 1.6mm with a layer height coded at 1.5mm. The layer height was smaller than the diameter of the nozzle to promote adhesion between layers. All structures printed for this work were 3 layers in height (4.5mm tall cumulatively), though structures up to 5 layers (6mm) in height have been successfully printed.

Curing

Immediately after printing, the paste was cured in a forced air oven (Cascade Tek, model: CTF322). For a sample of dimensions 4.8x4.5mm, we observed the samples were fully cured after 20 minutes at 45°C and then 2 hours at room temperature. To determine the cured state, a series of samples of different cross sectional areas (50 mm^2 and 363 mm^2) were created. These samples were all cured under the same conditions until they reached a moisture content of 3-5%, as measured by a pin-type moisture meter (part #MMD4E, by General Tools). These samples were cross-sectioned to confirm that they were fully cured.

The curing process of the mixture is not a temperature dependent reaction, but rather is dependent on the presence of the calcium sulfate similar in manner to the process in which gypsum plaster cures. Consequently, a high temperature curing process partially accelerates the cure time, but can also produce the negative result of generating cracks. This is due to a phenomenon similar to plastic shrinkage cracking seen in concrete. If water evaporates from the surface faster than subsurface water can move to the surface, drying shrinkage will create cracks

on the surface of the material[16]. Significant shrinkage does not occur if the curing happens at a controlled rate, with any shrinkage phenomenon occurring at sub-millimeter scale.

Reactive Material Architecture Testing

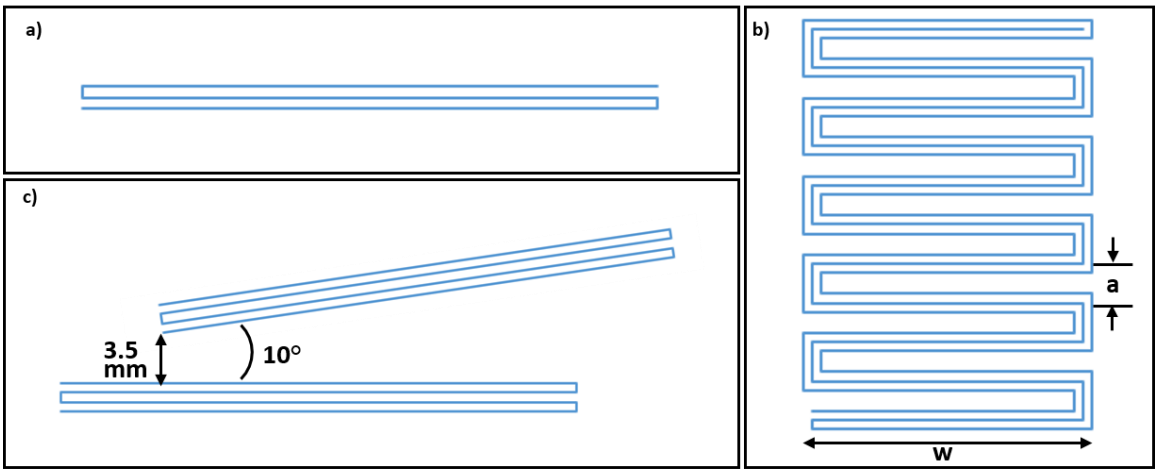

Figure 16 – Reactive material architectures, where a) is a linear architecture used to determine propagation speed, b) is used to test propagation of reaction perpendicular to direction of reaction, and c) is used to test propagation of reaction parallel to direction of reaction

Drawing inspiration from previous work by Sullivan et al, three RMA's were evaluated to explore the influence of the architecture on the reaction (depicted in Figure 16). The first architecture is a linear geometry, designed to measure the propagation rate of the thermite reaction. The second architecture consists of multiple 90° turns where the intent is to test the initiation and propagation of a new reaction that is perpendicular to the initial direction of reaction. Table 2 details the different tested dimensions for architecture 2. The third architecture is two linear geometries placed adjacent to each other at an angle. This architecture is intended

to test initiation and propagation of the reaction parallel to the direction of the initial reaction. All architectures are 3 printed layers in height (4.5 mm). In addition to the testing of these architectures, samples were prepared with parallel linear pieces to fully quantify the distance at which one architecture will ignite an adjacent architecture or feature, with the direction of reaction being perpendicular to the direction of propagation. Samples were also prepared with two linear pieces in series and a gap between them to quantify the gap length that propagation will span. These experiments were done for a single cross sectional area of 7x7mm. Furthermore, to eliminate potential variability between mixtures, a larger batch of thermite was prepared and poured into silicon molds (mold material: EcoFlex 00-30 by Reynolds Advanced Materials), which yielded 15 samples.

Parameters	**Iteration 1**	**Iteration 2**	**Iteration 3**	**Iteration 4**
Number of turns	3	5	10	10
Length	150 mm	150 mm	150 mm	70 mm
Width (w)	50 mm	50 mm	50 mm	50 mm
Centerline Spacing (a)	50 mm	30 mm	15 mm	7.5 mm

Table 2 - Tested dimensions for architecture 2 as depicted in Figure 16b. Four iterations of architecture 2 were tested, with different total turns, length, width, and centerline spacing.

The architectures were printed and ignited on 0.125" thick Al6061-T6 substrate. A small starter mass of 0.5 grams of mixed thermite and magnesium powder with a magnesium ribbon fuse (releasing approximately 1.4 kJ of energy) was used to ignite the cured architectures. All ignitions were filmed with at high speed camera (model: fps1000-720 by the Slow Motion Camera Company, Herfordshire, UK) at 1000 FPS and resolution of 1280x720, with a shade 5 welding filter.

Results

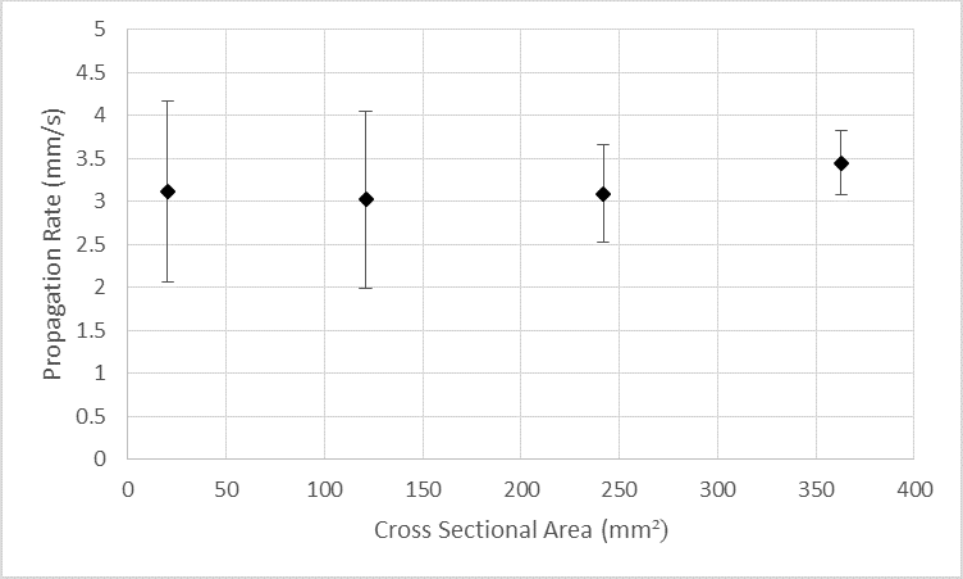

Figure 17 – Thermite reaction propagation rates for different cross sectional areas.

For our proposed thermite paste formulation, the average reaction rate across all cross sections was 3.19 ± 0.65 mm/s. Figure 3 shows the reaction rates for the four tested cross sectional areas, with a total of twelve tested samples. The average reaction rates for each cross sectional area are all within 0.3 mm/s of each other, with variability decreasing as cross sectional area increases. Sullivan et al reported different baseline reaction velocities for different film thicknesses, which indicates that a macroscale thermite mixtures behaves differently than a nanoscale nanothermite mixture.

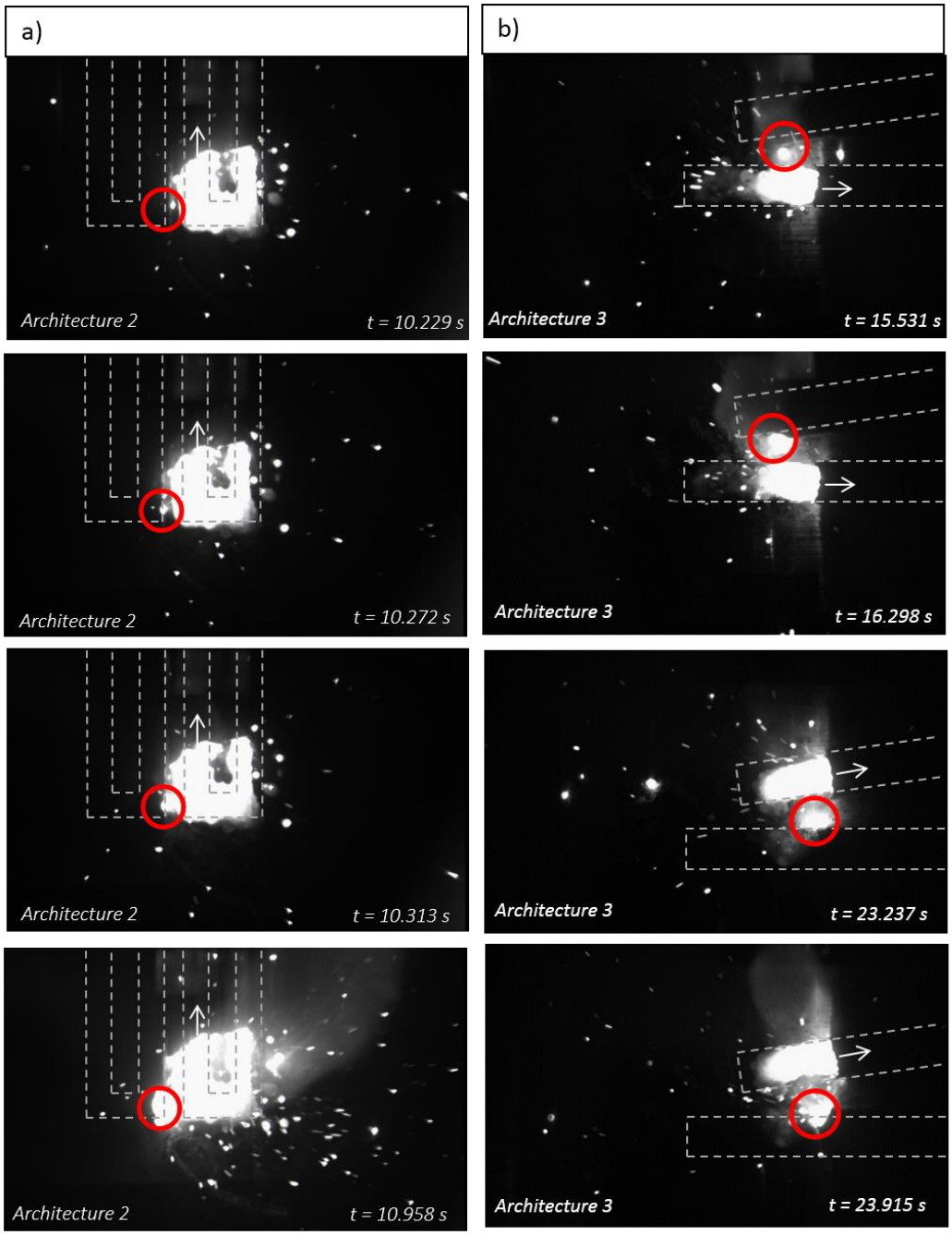

Figure 18 – a) Depicts adjacent thermite ignition initiation 2, taking place across 0.17s and b) two instances of adjacent ignition initiation in architecture 3

Figure 18 shows the described adjacent ignition phenomenon in two separate ignitions with two different architectures. Figure 18a presents an adjacent ignition beginning at the next turn of the

architecture, not in the direction of propagation (as indicated by the circled area). Figure 18b shows this phenomenon twice. The first two frames show the ignition of a separate section of thermite paste, which then propagates in parallel. The reaction in the bottom section of thermite then stops, but is reignited further down the line by the parallel piece.

In order to characterize propagation characteristics, we define the critical distance as the distance at which one ignited section of thermite will cross a gap and trigger a reaction in a non-ignited section of thermite. The critical distance for adjacent parallel ignition and the critical gap distance for series ignitions were determined for a single cross section of 49 mm^2 (7mm x 7mm). For adjacent parallel ignition, we have found that a critical gap distance for consistent parallel ignition was measured at 3mm, which is consistent with the edge to edge measurement found in the architecture 2 testing. We also observed that gaps of 5-7mm could occasionally cause adjacent ignitions, but the phenomenon is not consistent. In these pilot studies, we could not find a critical gap distance for series ignitions. We did not observe the ignition spanning a gap for this architecture in series.

Discussion

This project details the composition of a curing thermite paste, its printing characteristics, and architecture. The resulting paste is printable, has a high temperature reaction that produces molten iron, and the propagation characteristics can be controlled through RMAs. In this work, we define the reaction rate as the rate at which the reaction occurs in a linear scenario, independent of geometry. The propagation characteristics refer to the effects of architecture on reaction phenomena.

The baseline reaction rate of the curing paste, with all other conditions ideal, is dictated by the chemistry of the thermite reaction. Since the thermite reaction produces aluminum oxide ($Fe_2O_3 + 2Al \rightarrow 2Fe + Al_2O_3$)[10], any oxidation of the aluminum before the reaction pushes the paste closer to equilibrium. Aluminum already forms a passive oxide layer, but the oxidation of the aluminum is further promoted due to the presence of tartaric acid. This presence of oxidized aluminum likely slows the overall reaction rate. For this work, we focus on the first order demonstration of a curable and ignitable paste suitable for additive manufacturing, and leave the effects of the oxidation of aluminum for further study.

The reaction rate was observed to be primarily affected by curing, with under-cured samples reacting at slower rates and more uneven rates. In early experiments, we found that a sample with significant remaining moisture content would be unable to sustain its reaction. In under cured cases, we suspect the heat generated is not used to continue the reaction, but is instead being absorbed by the remaining water content inhibiting the reaction. Furthermore, extended (or over) curing periods do not increase reaction rate. We found that once the material had cured, the reaction rate was constant, and there was no advantage to extending curing time beyond the minimum. While the reaction rate is affected by curing, we found that it is not affected by the cross sectional area. Among the experiments we conducted, the rate remained at approximately 3.19 mm/s for all tested rectangular cross sectional areas between 21.6 mm^2 to 362.9 mm^2, as seen in Figure 3. Variability of the reaction rate decreases as the cross sectional area increases due to reaction characteristics eliminating the influence of environmental effects. Though overall, we observed that reaction rate is largely independent of cross sectional area for samples tested, which is an unusual and non-intuitive result that requires further study. However, given

this result, the speed at which the reaction traverses between two points can be controlled by increasing or decreasing the length of the path.

The thermite paste was printed using a paste printing technique. The primary obstacle when printing this thermite paste is premature curing in the syringe tubing and nozzle. The paste cures significantly faster in small volumes, which will create clogs in small diameter nozzles and in long sections of tubing. The paste has been successfully printed in a 0.84 mm diameter nozzle, but only as long as flow is continuously maintained to prevent clogs.

Generally, paste printing requires a layer height of half the nozzle diameter to ensure a clean, fully filled print. Since the thermite paste adheres to itself, it does not require a layer height less than the actual height of the paste. This prevents a buildup of cured paste around the nozzle, preserving print resolution and stopping nozzle clogging. Therefore, the layer height of 1.5mm is the actual height of the paste.

When the paste exits the nozzle it does not cure immediately, but instead remains in a plastic state for most of the print. Despite this, the paste is stable enough to support follow-on layers of the paste. Partial curing could be reached by way of a heated build plate, but is not necessary for smaller prints. A partial curing technique may be needed for larger structures, but this will be dependent on the nozzle size.

Propagation

The RMAs display interesting propagation characteristics. We found the thermite reaction propagates consistently along the printed lines. Furthermore, here exists a critical distance at which two separate lines of thermite essentially act as one, with the initial reaction starting a new

reaction in a new region, thereby skipping large sections of thermite. This new reaction appears to be caused by a combination of heat proximity and ejecta from the initial ignition. The heat proximity preheats the thermite and its baseplate, which allows the thermite section to be more easily ignited by a small amount of high temperature ejecta. The sparks alone are not enough to begin a new ignition, even if the same area is bombarded by a large number of sparks. We suspect there is a combination of heat and sparks that creates favorable ignition conditions; however, this topic requires further modeling and empirical evaluation and is outside the scope of this study.

Given our understanding of the thermite propagation properties, the critical distance and reaction rate can be combined to create geometries that span the same linear distance across a range of time scales. For example, a linear section of thermite will travel 111 mm in approximately 35 seconds. Using a variation of architecture 2 with a width of 30mm and an edge-to-edge gap of 8 mm (a = 15 mm), the same distance could be traversed in 121 seconds. This would allow for tailored and timed heat deposition, creating the basis of a programmable heat source.

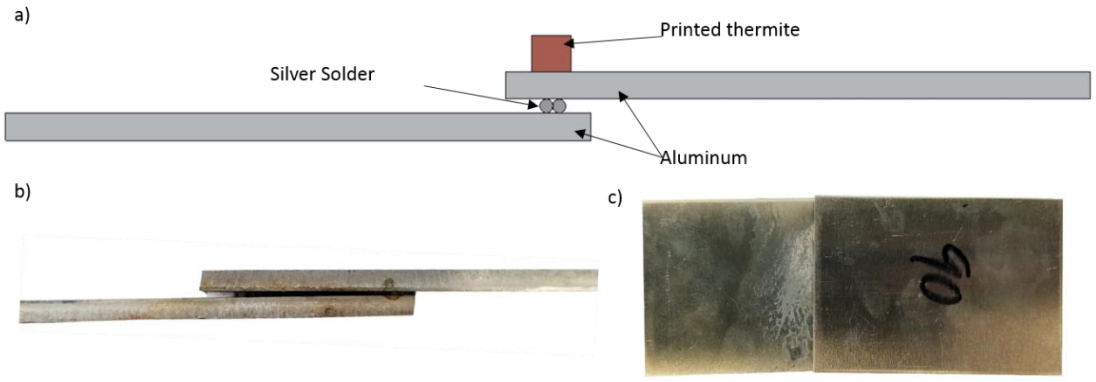

Figure 19 – a) Schematic of thermite joint setup. b) Side view of thermite created joint and c) top view of thermite created joint.

Thermite has a long tradition of playing an integral role in destructive and construction applications. In the following section, we present an example of the latter with a material joining proof of concept using the thermite architectures. Two 0.125" thick aluminum 6061-T6 pieces were placed in a lap joint configuration with Kapp LIQUID Golden Flux and KappAloy9 (91Sn/9Zn) solder, which has a melting point of 199°C, placed at the joint. A thermite architecture created through additive manufacturing (weighing 4 grams) was placed on top of the joint and ignited. The thermite served as a portable heat source for melting the solder. During the reaction, no pressure was applied to the solder site. The resulting joint and configuration can be seen in Figure 19. The heat generated by the reaction was uniform enough to melt the solder and create a joint, but the resulting temperatures were not high enough to damage the parent material. This first-order demonstration highlights the utility of a controllable thermite paste for in-situ joining operations. Using the reaction controlling characteristics of thermite structures, heat input into a joint could be easily controlled outside of a laboratory setting.

Joining Applications

The joining applications are limited by the reaction temperature of the cured thermite paste, which has a theoretical maximum reaction temperature of 2862°C for Fe_2O_3/Al thermite (assuming a complete adiabatic reaction)[10]. The actual reaction temperature is dictated by the mass of reactive material, with larger masses reaching higher temperatures[17]. Table 3 shows the temperatures needed for common plastic welding and metal brazing techniques.

Material	Joining Temperature
Polypropylene (PP)	300° C
Polyethylene (PE)	290° C
Acrylonitrile Butanadiene Styrene (ABS)	260° C
Polyvinyl Chloride (PVC)	275° C
Polyurethane (TPUR)	300° C
Copper	1095° C
Silver	705° C
Nickel	1040° C
Aluminum	580° C
Gold	980° C
KappAloy9	199° C

Table 3 - Common materials and their joining temperatures[18.19.20]

Thermite architectures can be tailored to create specific temperature profiles for the joining applications without damaging the parent material. Since the reaction rate of the proposed paste is relatively constant across different cross sections, so RMAs can be easily scaled up, therefore allowing more heat to be deposited in the same time frame. Additional heating characteristics can be tuned by changing the base thermite formulation. The current paste is primarily composed of iron oxide and aluminum powder, but other thermite formulations could be used.[10]

One potential application of RMAs as a portable heat source is for materials joining in austere environments, such as NASA's in-space exothermic brazing experiments[21] and Masubichi's underwater exothermic welding experiments[22]. Traditional welding techniques for underwater environments are dangerous and require a highly-skilled operator. RMAs as a portable heat source could make underwater welding safer and require less skilled labor, since the architectures could be printed (or pre-printed prior to deployment) on structures and ignited remotely. Furthermore, RMAs have the potential for rapid field repair of armored vehicles, once again eliminating the need for welding equipment, a power source, and skilled operators.

Conclusion

In this work we present a thermite paste formulation suitable for additive manufacturing. The formulated paste is composed of readily sourced materials, and is safe to create, print, and transport. We empirically demonstrated that the proposed thermite paste reacts at a relatively constant rate across a range of cross-sections. Lastly, this work demonstrates the potential of thermite RMAs as a programmable heat source for constructive or joining applications, especially in austere or dangerous environments.

Acknowledgements

The author wishes to thank Dr. Kelsey Hatzell and her students Marm Dixit and Brice Harkney for their assistance in obtaining rheological measurements. This work was funded by the NASA Tennessee Space Grant Consortium.

Author Disclosure Statement

No competing financial interests exist.

References

1. Sun J, Zhou W, Yan L, et al. Extrusion-based food printing for digitalized food design and nutrition control. J Food Eng. 2018;220:1–11. Available from: https://doi.org/10.1016/j.jfoodeng.2017.02.028

2. Murphy S V., Atala A. 3D bioprinting of tissues and organs. Nat Biotechnol. 2014;32(8):773–85. Available from: http://dx.doi.org/10.1038/nbt.2958

3. Leigh SJ, Bradley RJ, Purssell CP, et al. A Simple, Low-Cost Conductive Composite Material for 3D Printing of Electronic Sensors. PLoS One. 2012;7(11):1–6.

4. Tibbits S. 4D printing: Multi-material shape change. Archit Des. 2014;84(1):116–21.

5. Raviv D, Zhao W, McKnelly C, et al. Active printed materials for complex self-evolving deformations. Sci Rep. 2014;4:1–8.

6. Ge, Qi & Qi, H.Jerry & L. Dunn, Martin. (2013). Active materials by four-dimension printing. Applied Physics Letters. 103. 131901-131901. 10.1063/1.4819837.

7. Bose S, Vahabzadeh S, Bandyopadhyay A. Bone tissue engineering using 3D printing. Mater Today [Internet]. 2013;16(12):496–504. Available from: http://dx.doi.org/10.1016/j.mattod.2013.11.017

8. Goldstein TA, Smith LP, Smith BD, Grande DA, Zeltsman D. Integrating Biodegradable 3-Dimensional-Printing into Tracheal Reconstruction. 2015;(September):27–33.

9. Sullivan KT, Zhu C, Duoss EB,et al. Controlling Material Reactivity Using Architecture. Adv Mater. 2016;28(10):1934–9.

10. S.H. Fischer MCG. A Survey of Combustible Metals, Thermites, and Intermetallics for Pyrotechnic Applications. In: AIAA/ASME/SAE/ASEE Joint Propulsion Conference. 1996.

11. Lonsdale CP. Thermite rail welding: history process developments, current practice and outlook for the 21st century. Proc AREMA 1999 Annu Conf [Internet]. 1999;1895(C):18.

12. Murray AK, Isik T, Ortalan V, et al. Two-component additive manufacturing of nanothermite structures via reactive inkjet printing. J Appl Phys. 2017;122(18):1–6.

13. Ruz-Nuglo FD, Groven LJ. 3-D Printing and Development of Fluoropolymer Based Reactive Inks. *Adv Eng Mater*. 2018. doi:10.1002/adem.201700390

14. Fleck TJ, Murray AK, Gunduz IE, Son SF, Chiu GTC, Rhoads JF. Additive manufacturing of multifunctional reactive materials. *Addit Manuf*. 2017:176-182.

15. Knorre H, Langer M, Leidl P, inventors; Deutsche Gold- Und Silber-Scheideanstalt Vormals Roessler, assignee. Tartaric acid as a retardant for gypsum plaster. United States patent US 4,094,693 A. 13 June 1978.

16. H. Kosmatka S, L. Wilson M. Design and Control of Concrete Mixtures . Construction. 2011. 444 p.

17. Chekunov IP. Exothermal Brazing of Steel Piping with High Temperature Brazing Alloys. *Weld Prod (English Translation of Svar Proizv)*. 1972:39-42.

18. Plastic Welding with Steinel Heat Guns [Internet]. 2018 [cited 2018 Feb 4]. p. 1–4. Available from: https://www.eastwood.com/steinel-heat-gun-how-to-plastic-weld-plastic-welding-tool

19. The Brazing Guide. GH Induction Atmospheres. p. 1–10.

20. KappAloy ™ Tin-Zinc Solders for Aluminum-to-Aluminum [Internet]. 2018 [cited 2018 Apr 2]. p. 3–4. Available from: http://www.kappalloy.com/aloy-solder.php

21. Skylab Results: Volume 1. In: *Third Space Processing Symposium*. ; 1974.

22. Masubuchi, K., & Anderssen, A. H. (1973, January 1). Underwater Application Of Exothermic Welding. Offshore Technology Conference. doi:10.4043/1910-MS

CHAPTER 3: MULTI-MATERIAL ADDITIVELY MANUFACTURED COMPOSITE ENERGETICS VIA CONTINUOUS FILAMENT DIRECT INK WRITING

The following work has been submitted to *Additive Manufacturing*.

Abstract

Advances in multi-material additive manufacturing have enabled advancements in the manufacture of composite materials. In this work, a family of thermite-based reactive materials is created and evaluated for the suitability as composite energetic structures. The burn rate with respect to binder ratio is observed to be highly predictable and exponential (coefficients of determination of $r_{Ti}^2 = 0.984$ and $r_{Al}^2 = 0.973$), with composites transitioning from one binder mass fraction to another. To create composites, a single layered syringe and nozzle are used in conjunction with continuous filament direct ink writing. The resulting prints show success in composite structure with a transition zone between printed materials. These results show both a variety of thermite-based energetics with easily modifiable reaction rates and a technique to print said reactive materials to create composite structures.

Introduction

Advances in multi-material additive manufacturing have enabled advancements in the manufacture of composite materials. In this work, a family of thermite-based reactive materials is created and evaluated for the suitability as composite energetic structures. The burn rate with respect to binder ratio is observed to be highly predictable and exponential (coefficients of

determination of $r_{Ti}^2 = 0.984$ and $r_{Al}^2 = 0.973$), with composites transitioning from one binder mass fraction to another. To create composites, a single layered syringe and nozzle are used in conjunction with continuous filament direct ink writing. The resulting prints show success in composite structure with a transition zone between printed materials. These results show both a variety of thermite-based energetics with easily modifiable reaction rates and a technique to print said reactive materials to create composite structures.

Methods and Materials

Multi-Material Printing

Before printing, the syringe was initially loaded in layers in the syringe. Water content was adjusted for each mixture in order to approximately match viscosities. To test the transition, a single layer geometry was printed. To visualize the flow inside the syringe, material was filled in layers, partially extruded, and then left to cure in the syringe for 48 hours. Once cured, the syringe was cut in half and sanded to show the flow structure.

All printed samples were manufactured using a Hyrel3D System 30M SR printer with an SDS-60 print head and an 8 gauge (3.43mm inner diameter) nozzle. The aluminum-based thermite samples were based on Neely et al. and the titanium-based thermite samples were derived from Neely et al. in combination with previously established thermite compositions [3, 20] For both mixtures, the binder was calcium sulfate hemihydrate.

Effects of Binder Mass Fraction on Reaction Velocity

To test the effects of decreased binder mass fraction and establish a baseline reaction rate for the new mixtures, a series of molded samples were created. The samples were molded rather than printed to ensure uniformity within each batch of thermite. Prior work has shown no difference between printed and molded samples [3]. For each mass ratio combination shown in Table 4, three 5 inch molded samples were created and tested. Each reaction was filmed using a high speed camera with a shade 5 welding filter at a frame rate and resolution as specified below.

Mixture Type	Mass Ratio	Frame Rate	Resolution
Aluminum	$Fe_2O_3 : Al : Ca_2SO_4$		
	0:2:3	1,000	1280x720
	3:2:2	1,000	1280x720
	3:2:1	4,000	640x360
	3:2:0.5	10,000	640x120
	3:2:0.1	20,000	640x60
Titanium	$Fe_2O_3 : Ti : Ca_2SO_4$		
	0:3:1	1,000	1280x720
	2:3:1	8,000	1280x60
	2:3:0.5	10,000	640x120
	2:3:0.25	20,000	640x60

Table 4 – Tested mass ratios of aluminum-based thermite and titanium-based thermite

Composite Energetics

To test the reaction transition behavior of composite energetics, two multi-material samples were molded. These samples were molded to minimize mixing at the interface regions, thereby only testing the reaction behavior and the transition behavior in the most extreme case. Each sample consisted of three distinct material sections to create regions of different reaction rates. The first sample, consisting of titanium-based thermite, had a region of 2:3:0.5 mass ratio, then a region of

0:3:1 mass ratio, and then again a region of 2:3:0.5 mass ratio. The second sample consisted of an aluminum-based thermite in three stages. The first stage consisted of a 3:2:0.1 mass ratio, the second a 0:2:3 mass ratio, and the third stage of a 3:2:0.1 mass ratio.

Results and Discussion

Multi-Material Printing

The printed structures showed three phases: the first material, a transition state consisting of both materials, and then the second material. These stages can be clearly seen in Figure 20.

Figure 20 – Printed geometry showing the first material, the transition stage, and the second material from an a) overhead view, b) overall cross-sectional view, and c) individual cross sections

The transitional phase does not consist of a uniform mixing, but instead consists of the second mixture encased by the first mixture. This is due to the behavior of the two fluids within the syringe, which is visualized in Figure 21.

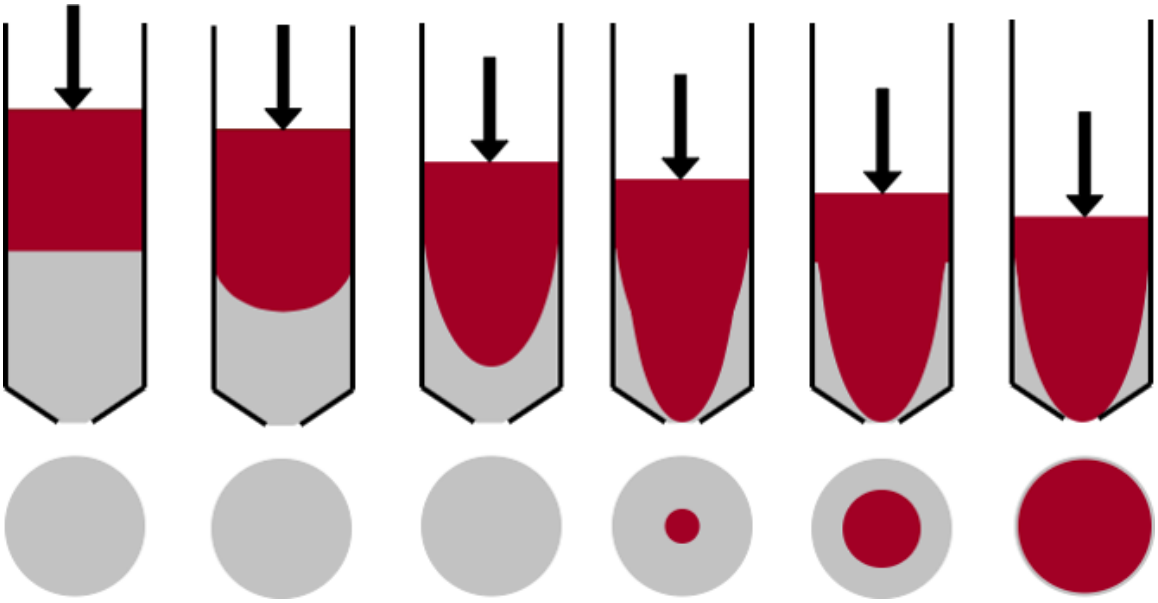

Figure 21 – Fluid behavior during the extrusion process, with the syringes on top and the cross section of extruded material below. The leftmost side is the initial state of the syringe, with extrusion progressing to the right.

The syringe starts with the two fluids layered, with the bottom layer designated as material 1 and the next layer designated as material 2. As the plunger for the syringe is depressed, material 1 is exclusively extruded. The Reynolds number is below 2100, which is indicative of laminar flow. In turn, a parabolic velocity profile forms downstream of the plug flow induced by the plunger. Under frictionless conditions, the plug flow would force all of material 1 out of the syringe before material 2 is observed. However, due to the no-slip condition of the walls and friction within the boundary layers, a Poiseuille flow begins to develop. Flow from material 2 moves

inward by a fluid-dynamic nozzle created by the boundary layer of material 1, lending to material 1 being "pierced" by material 2. Concisely stated, when material 2 initially reaches the nozzle, material 1 still remains along the edges. This results in an extruded cross section composed of material 2 in the center, surrounded by material 1 (Figure 21, fourth image from the left). This cross section was confirmed by experimental results, as seen in Figure 20c.

The parabolic fluid flow in the syringe can be both intuited and confirmed by the velocity profile derived from the Hagen-Poiseuille equation, as can the dominate edge effects near the outlet of the syringe. This was also confirmed experimentally, as seen in Figure 22, by letting material cure within a syringe after some extrusion.

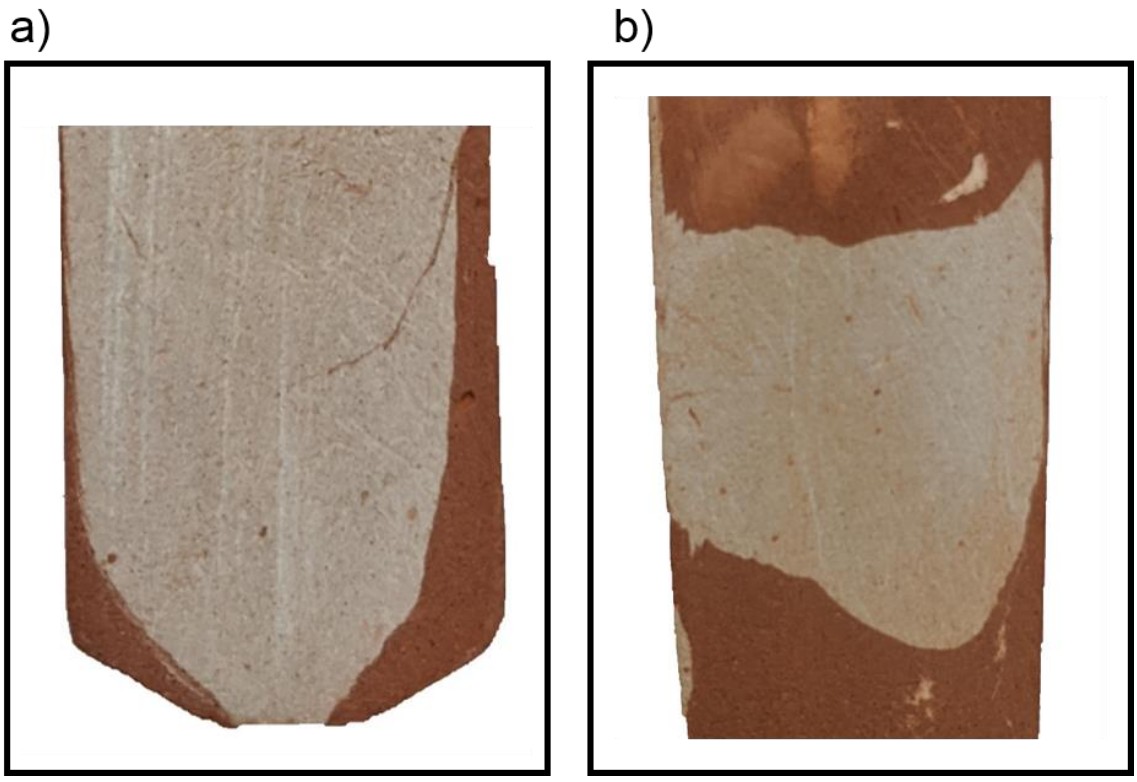

Figure 22 – Cross section of cured syringes, with a) showing the described edge phenomenon at the outlet and b) showing the parabolic flow shape away from the outlet

Figure 22a clearly shows the edge effects near the syringe outlet. This extrusion would result in an inner core of material 2 surrounded by material 1. Figure 22b shows the parabolic flow within the syringe. This flow is asymmetric due to the difficulties of evenly distributing material through the filling process. If a more symmetric filling method can be identified, we suspect the flow would be more symmetric.

Effects of Binder Mass Fraction on Velocity

The reaction rate of these mixtures is influenced by two simultaneous reactions. The first reaction is the thermite reaction, which in this work is either aluminum and iron oxide ($2Al + Fe_2O_3$) or titanium and iron oxide ($3Ti + Fe_2O_3$). The second reaction is the reaction between the fuel, titanium or aluminum, and the binder, calcium hemihydrate. The binder affects its structural integrity, but also decreases the reaction rate. Table 5 shows the tested compositions and their respective reaction rates.

The measured reaction rates show that the reaction rate increases as the binder mass ratio decreases. Plotting reaction rate against the binder mass proportion indicates a decaying exponential relation. High coefficients of regression are calculated when applying an exponential fit to each data set, where the aluminum-based thermite has $R^2 = 0.973$ and the titanium-based thermite has $R^2 = 0.984$.

Mixture Type	Mass Ratio	Reaction Rate (mm/s)	Standard Deviation (mm/s)	Standard Deviation (%)
Aluminum	$Fe_2O_3 : Al : Ca_2SO_4$			
	0:2:3	1.79	0.25	13.97%
	3:2:2	3.17	0.17	5.36%
	3:2:1	26.14	2.29	8.76%
	3:2:0.5	64.95	3.93	6.05%
	3:2:0.1	159.91	13.50	8.44%
Titanium	$Fe_2O_3 : Ti : Ca_2SO_4$			
	0:3:1	6.01	0.33	5.49%
	2:3:1	39.44	5.64	14.3%
	2:3:0.5	105.21	10.85	10.31%
	2:3:0.25	212.58	13.87	6.52%

Table 5 – Tested compositions and their measured reaction rates and standard deviations

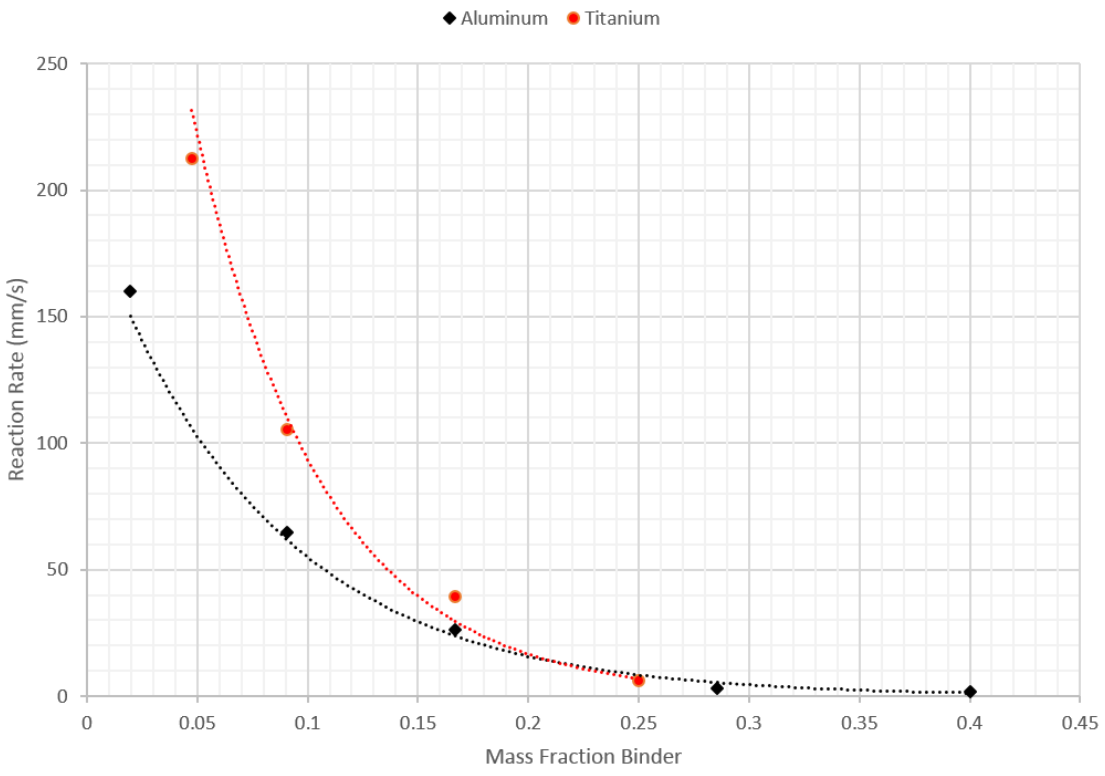

Figure 23 – Reaction Rate vs Mass Fraction Binder for both the aluminum-based thermite and the titanium-based thermite, showing clearly exponential behavior

The mass fraction of the binding agent limits the overall reaction rate. Logically, the thermite reaction is not inhibited when the binding agent is a smaller fraction of the mixture. As with the vast majority of reactions, dissociation of molecules first takes place to form radicals instead of through a direct reaction. The chain initiating step of dissociating reactants is highly endothermic, requiring large activation energies to propagate. Addition of binder inhibits the reaction by either creating unreactive molecular species or creating radicals with lower energy than needed to continue the reaction. Intermediate ferrous structures of $Al+Fe_2O_3$ reactions are known to require high energy for propagation, which leads to the conclusion of the binder acting as an inhibiting agent.

Binding agent mass fractions of 0.25 (Ti) and 0.40 (Al) were the limits in creating material compositions with self-propagating reaction. Structures near this limit exhibited the highest integrity and are likely to be used in more complex or intricate structure design at the expense of a slower reaction rate. Lower binder mass fractions result in qualitatively weaker structures, yet all tested ratios were strong enough to be handled and were printable. Theoretically, a minimum binder ratio at which the mixture is no longer printable (or no longer structural) exists, but was not explored in this work due to the hardware limitations for measuring reaction rate.

Composite Energetics

The tested composites contained a single type of thermite (aluminum-based or titanium-based), and variable binding agent mass fractions. Resulting samples were ignited and filmed at 10,000 frames per second at a resolution of 640x120, with their velocities measured with respect to their absolute position along the sample. The first sample consisted of a titanium-based thermite with

three stages, first a 2:3:0.5 section, then a 0:3:2, then again 2:3:0.5. For ease of reference, these regions are denoted as stages 1, 2, and 3. The reaction rates are shown in Figure 24, with the vertical lines indicating the transition from one energetic composition to another.

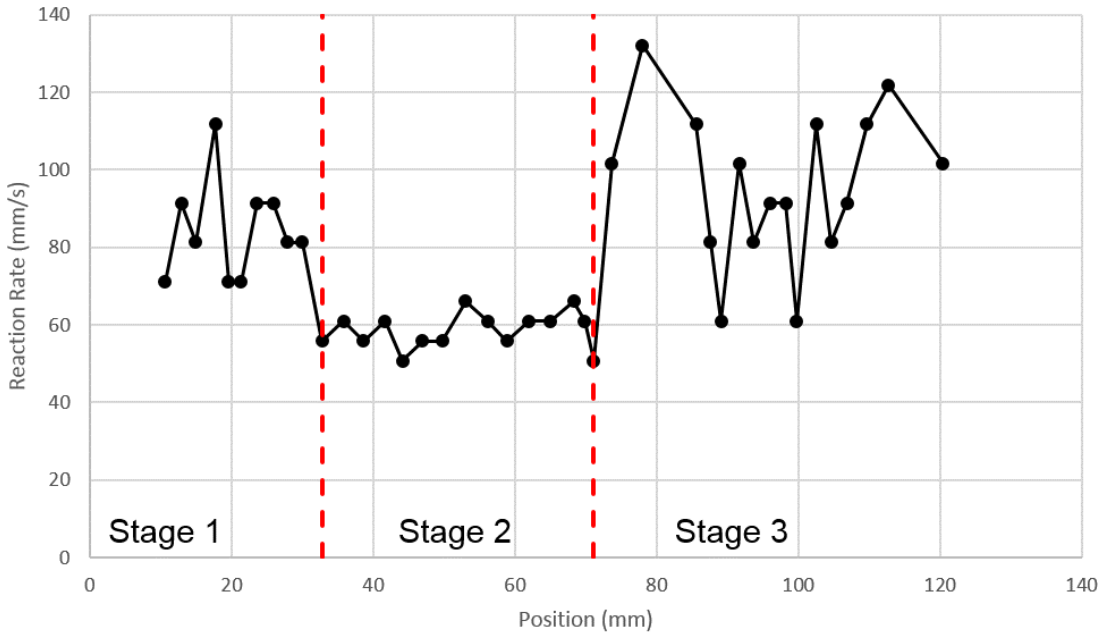

Figure 24 – Reaction rate with respect to position for sample 1, showing a region of high reaction rates, then a region of lower reaction rates, and again a region of high reaction rates. The vertical dashed lines indicate the transition from one composition to another.

Given the composition of the sample, the composite reaction rates should be, on average, be 105.21 mm/s for stages 1 and 3, and 6.01 mm/s for stage 2. However, the average reaction rate for stage 1 is 84.33 mm/s, for stage 2 is 58.59 mm/s, and for stage 3 is 95.89 mm/s. The faster sections, stages 1 and 3, reach reaction rates near the average of 105.21 mm/s. The reaction rate for stage 2 is significantly faster than the baseline rate of the material of 6.01 mm/s. This is likely due to the heat build-up from the preceding energetic, which is conducted through the

metal plate supporting the sample and through the sample itself. The characteristics of stages 1 and 3 are dominated by the aluminum-based thermite chain reactions (as opposed to the inhibiting reactions of the binder intermediates), which creates a significant amount of heat. Excess heat from this highly exothermic reaction preheats stage 2 via conduction through the sample and through the metal substrate, which increases the reaction rate. It is worth nothing that hardware limitations affect the precision, less so accuracy, of measurements as well. High frame rates reduce resolution, which results in a reaction rate variance of ±5.08 mm/s per pixel.

Sample 2 consisted of three stages of an aluminum-based thermite. The first stage had a mass ratio of 3:2:0.1, a second stage of 0:2:3, and a third stage of 3:2:0.1. This sample should also show a region of a faster reaction rate, then a slower rate, and then again a faster rate. Figure 25 shows the reaction rate with respect to position for sample 2, with vertical dashed lines indicating the transition from one composition of thermite to another.

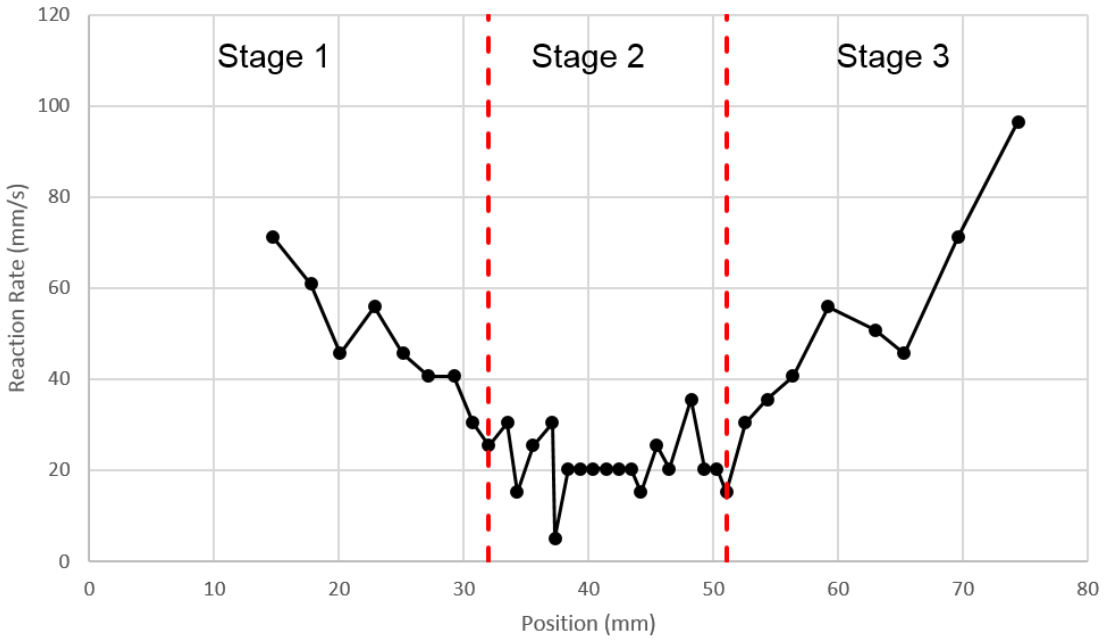

Figure 25 – Reaction rate with respect to position for sample 2, showing a region of high reaction rates, then low reaction rates, and then again high reaction rates. The vertical dashed lines indicate a transition from one region of thermite to another.

For sample 2, the average reaction rates for each segment are 42.28 mm/s for stage 1, 21.17 mm/s for stage 2, and 53.34 mm/s for stage 3. However, the reaction rates for these compositions should be 64.95 mm/s for stages 1 and 3, and 1.79 mm/s for the second stage. Stages 1 and 3 are near the appropriate reaction rate, but the second stage is once again higher than previously measured reaction rates. This is also likely the influence of the built-up heat from the previous segment of reaction, which is conducted through both the metal substrate and through the sample itself.

The molded composite samples show a sharper transition than a printed sample will, assuming the sample is printed from a single layered syringe. As seen in Figure 7, there is a transition region in the extruded material where both materials are present. This region would result in a

larger transition zone with an in-between reaction rate. For large samples, the effects of the transition rate will be negligible, but the transition effects could dominate the behavior of a small sample.

Conclusion

Multi-material printing is possible from a single syringe with similar fluid viscosities. While the transition from one material to the next currently involves a transition zone. An optimized syringe (with low friction walls) could potentially minimize the transition zone. The current technique is not ideal if sharp transitions are needed or if the materials have different viscosities. However, the advantages of being able to layer materials in a syringe for a single continuous print are clear. Printing from a single syringe eliminates start- and stop- points for multiple nozzles, which eliminates the need for complex ink control systems and increases the strength of the resulting part.

The binding agent mass fraction significantly affects reaction speed. Decreasing the binder amount results in increased reaction rate for both the aluminum-based and titanium-based thermite. The relationship between mass binder proportion and reaction speed is strongly exponential and will allow materials to be tuned to specific reaction rates by altering the binder content to easily create custom printable energetics.

These custom energetic ratios can be combined to create composite energetics with different reaction rates and heat deposition in different segments of a single structure. These structures can transition from one energetic to another regardless of reaction rate in the preceding or anteceding energetic. However, the behavior of generally slower energetics may be influenced

by the surrounding energetics. Regardless, composite energetics are possible using these mixtures and can be easily printed using a single syringe-based print system.

Acknowledgements

This work was supported by the Naval Engineering Education Consortium (N00174-19-1-0020).

References

1. Sullivan K, Zhu C, Duoss E, Gash A, Kolesky D, Kuntz J et al. Controlling Material Reactivity Using Architecture. *Advanced Materials.* 2015;28(10):1934-1939.
2. Murray A, Isik T, Ortalan V, Gunduz I, Son S, Chiu G et al. Two-component additive manufacturing of nanothermite structures via reactive inkjet printing. *Journal of Applied Physics.* 2017;122(18):184901.
3. Neely K, Galloway K, Strauss A. Additively Manufactured Reactive Material Architectures as a Programmable Heat Source. *3D Printing and Additive Manufacturing.* 2019;6(4):210-216.
4. Fleck T, Murray A, Gunduz I, Son S, Chiu G, Rhoads J. Additive manufacturing of multifunctional reactive materials. *Additive Manufacturing.* 2017;17:176-182.
5. Li L, Saedan M, Feng W, Fuh J, Wong Y, Loh H et al. Development of a multi-nozzle drop-on-demand system for multi-material dispensing. *Journal of Materials Processing Technology.* 2009;209(9):4444-4448.

6. Khan A, Rahman K, Kim D, Choi K. Direct printing of copper conductive micro-tracks by multi-nozzle electrohydrodynamic inkjet printing process. *Journal of Materials Processing Technology.* 2012;212(3):700-706.
7. Sochol R, Sweet E, Glick C, Venkatesh S, Avetisyan A, Ekman K et al. 3D printed microfluidic circuitry via multijet-based additive manufacturing. *Lab on a Chip.* 2016;16(4):668-678.
8. Hardin J, Ober T, Valentine A, Lewis J. Microfluidic Printheads for Multimaterial 3D Printing of Viscoelastic Inks. *Advanced Materials.* 2015;27(21):3279-3284.
9. Kim H, Park E, Kim S, Park B, Kim N, Lee S. Experimental Study on Mechanical Properties of Single- and Dual-material 3D Printed Products. *Procedia Manufacturing.* 2017;10:887-897.
10. Li T, Wang L. Bending behavior of sandwich composite structures with tunable 3D-printed core materials. *Composite Structures.* 2017;175:46-57.
11. Melenka G, Cheung B, Schofield J, Dawson M, Carey J. Evaluation and prediction of the tensile properties of continuous fiber-reinforced 3D printed structures. *Composite Structures.* 2016;153:866-875.
12. Li N, Li Y, Liu S. Rapid prototyping of continuous carbon fiber reinforced polylactic acid composites by 3D printing. *Journal of Materials Processing Technology.* 2016;238:218-225.
13. Dimas L, Bratzel G, Eylon I, Buehler M. Tough Composites Inspired by Mineralized Natural Materials: Computation, 3D printing, and Testing. *Advanced Functional Materials.* 2013;23(36):4629-4638.

14. Hou Z, Tian X, Zhang J, Li D. 3D printed continuous fibre reinforced composite corrugated structure. *Composite Structures.* 2018;184:1005-1010.
15. Leigh S, Bradley R, Purssell C, Billson D, Hutchins D. A Simple, Low-Cost Conductive Composite Material for 3D Printing of Electronic Sensors. *PLoS ONE.* 2012;7(11):e49365.
16. Truby R, Wehner M, Grosskopf A, Vogt D, Uzel S, Wood R et al. Soft Somatosensitive Actuators via Embedded 3D Printing. *Advanced Materials.* 2018;30(15):1706383.
17. Gallant F, Bruck H, Prickett S, Cesarec M. Graded polymer composites using twin-screw extrusion: A combinatorial approach to developing new energetic materials. *Composites Part A: Applied Science and Manufacturing.* 2006;37(6):957-969.
18. Bruck H, Gallant F, Gowrisankaran S. Development of a Novel Continuous Processing Technology for Functionally Graded Composite Energetic Material using an Inverse Design Procedure. 2006.
19. Young G, Bruck H, Gowrisankaran S. Modeling of Rocket Motor Ballistics for Functionally Graded Propellants. In: JANNAF Combustion Meeting. 2003.
20. Fischer S, Grubelich M. A Survey of Combustible Metals, Thermites, and Intermetallics for Pyrotechnic Applications. In: 32nd AIAA/ASME/SAE/ASEE Joint Propulsion Conference. 1996.

CHAPTER 4: SOLDERED COPPER LAP JOINTS USING REACTIVE MATERIAL ARCHITECTURES AS A HEAT SOURCE

The following work previously appeared in *Manufacturing Letters*, Volume 24 (April 2020).

Abstract

Traditional welding and joining techniques require an independent heat source and a skilled operator, which makes complex joints and welding in remote environments difficult. Additively manufactured reactive material architectures can be used as a programmable heat source, minimizing both the joining equipment and any operator hazards. This work demonstrates the feasibility of using reactive material architectures as a programmable heat source to create soldered copper lap joints and compares these joints to traditionally soldered joints.

Introduction

Joining in austere environments is challenging. Traditional welding or brazing requires a skilled operator and heavy equipment that is difficult to power, maintain, and transport in harsh environments. To overcome the cost and complexity of traditional methods, energetic materials are used a heat source, commonly known as exothermic brazing. Exothermic brazing utilizes the heat produced from a solid-state or near solid-state reaction to melt filler material for joining processes. It can be used to create joints in isolated environments or in physically complex or inaccessible joints [1].

Previous work has shown the success of exothermic brazing in space and underwater [2][3]. Exothermic brazing has also been successfully used for pipe brazing and exothermically brazed hydraulic fittings in aircraft [4][5]. However, this work has been limited by the need for complex fixturing of both the joint and the surrounding energetic. With the advancement of additive manufacturing technology, structurally-sound energetics with complex geometries are now generated effortlessly. Energetics manufactured with digital fabrication tools are known as reactive material architectures (RMA's) and enable new field expedient joining techniques [6][7].

RMA's are structures designed to control reaction rates and heat generation through geometric features rather than changes in chemical composition alone. An example of this control can be seen in the creation of solid rocket fuel grains using additive manufacturing techniques, resulting in printed fuel grains with comparable burn rates to their cast counterparts [8][9]. Additive manufacturing techniques can also create unique geometries with features that cannot be cast (e.g. overhangs, undercuts, infill porosity). There have been some applications of RMA's in joining at the nano-level for on-chip joining, but there exists a need for macro-level architectures for macro-level joining [10]. This paper shows a low-temperature proof-of-concept using reactive material architectures as a heat source for copper-to-copper soldering. The resulting joint, while suboptimal, is comparable to traditionally soldered joints. Results indicate for scalability for joining processes requiring higher temperatures.

Methods

The selected energetic for this work is a highly viscous thermite paste composed of iron oxide (Fe_2O_3), aluminum powder, and calcium hemihydrate ($CaSO_4 \bullet 0.5H_2O$) in a 3:2:2 mass ratio.

All samples were lit using a small starter mass of thermite and magnesium powder with a magnesium ribbon fuse, as originally described in previous work [11]. Samples were printed using a Hyrel Engine SR printer with an SDS-60 syringe-based print-head.

Temperature Measurement

Thermites follow a characteristic curve that relates mass and temperature, with higher masses resulting in higher temperatures [4]. Therefore, the maximum temperature reached by the thermite, which is a key parameter in joining, can be estimated by the mass of the material. To determine this relationship for this new energetic, a series of temperature measurements were taken.

Thermite samples were molded to have the same projected footprint (0.75x1.75”), but different masses. These samples were placed on top of a piece of 2x2x0.040” copper, with a k-type thermocouple (Omega HH-KK-24-SLE) beneath. These samples were then ignited, recording time and temperature data for each set. A new piece of copper was used for each ignition. The resulting temperature and mass data can be seen below in Fig. 26.

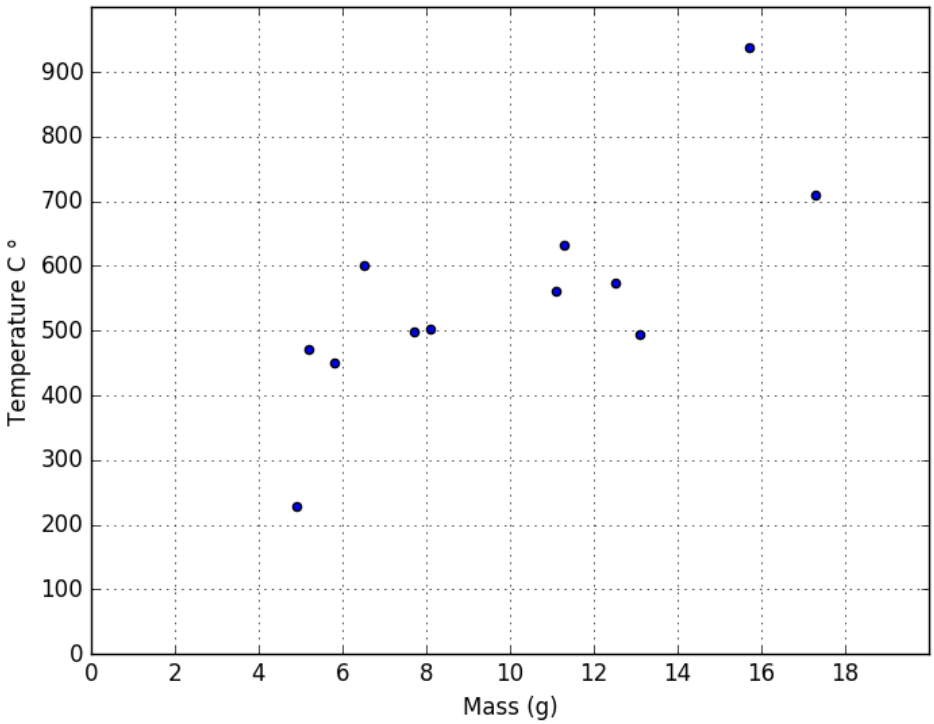

Figure 26 – Measured temperature-mass relationship for printable thermite formulation

Mass Selection

The plot in Figure 26 shows a relationship between mass and maximum temperature that can be used to guide mass selection for joining. As expected, the maximum measured temperature increased as mass of thermite increased. Smaller masses of thermite have a smaller thermal inertia, which causes reaction characteristics to be more sensitive to mixing and environmental effects. For this study, thermite masses between 3 and 5 grams were selected, as these masses resulted in temperature higher than the melting temperature of the solder (221°-246° C), but not high enough to damage the copper substrate.

Joint Setup

Each joint comprised of two 2x2x0.040” copper coupons arranged in a lap joint. Each joint was cleaned with acetone, and then prepared with flux. Four 2 inch lengths of solder (KappZapp4, 96Sn/4Ag Solid Wire solder for copper) were placed in the lap joint. A printed thermite sample was placed on top of the joint, with the entire setup on a bed of sand. A metal spacer was placed beneath the top copper coupon to account for the melting of the solder, making the top copper sample and bottom copper sample parallel after ignition. This configuration can be seen below in Figure 27. Additional parent samples were made and prepared in an identical fashion, except it was placed in an oven at 240°C for 2 hours. Four thermite joints and three parent oven samples were created.

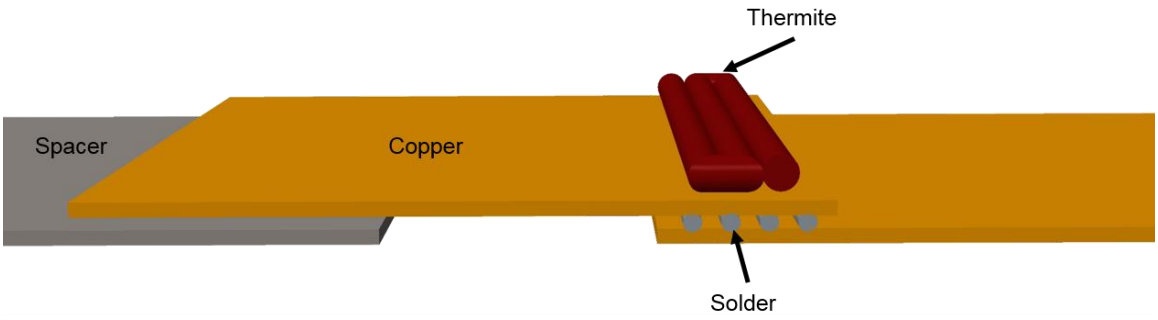

Figure 27 – Setup for samples joined with thermite, consisting of two copper samples in a lap joint, with solder between the samples and thermite on the top surface of the uppermost copper sample

Joint Testing

Each joint was cut into two 1 inch wide samples and tensile tested with a fixed elongation rate of 2 mm/min.

Results and Discussion

The full experimental conditions and resulting tensile strengths can be seen below in Figure 28.

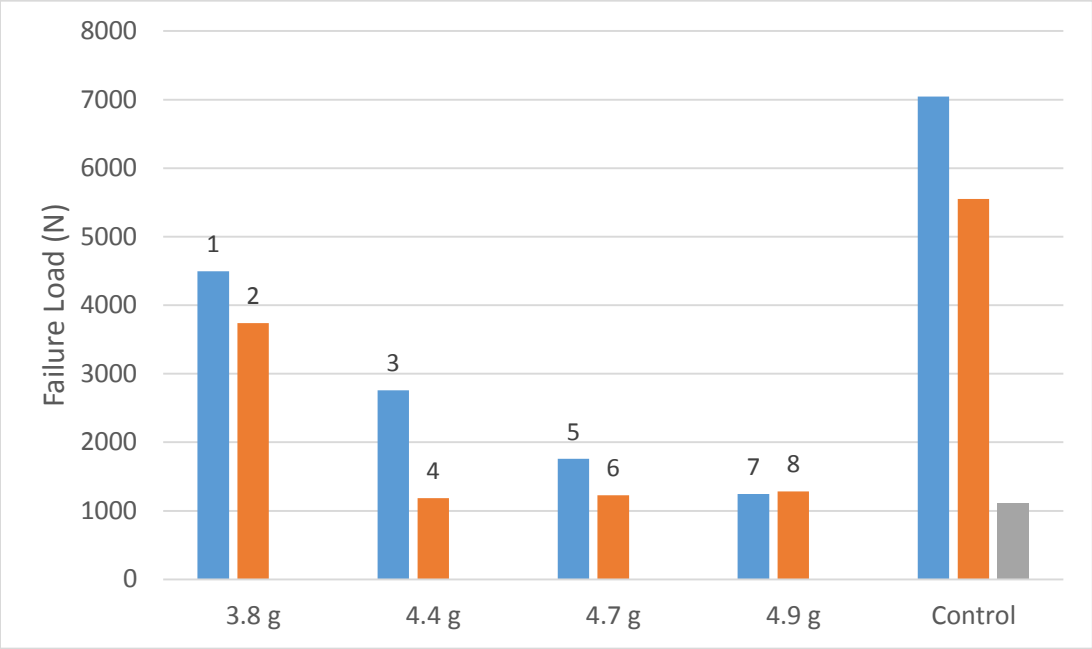

Figure 28– Load at failure for sample joints and control joints. The experimental samples are labeled 1-8 for future reference.

The resulting thermite joint strengths are comparable to the control joint strengths, with the strongest thermite joint breaking at a load of 4497 N, or 63.8% of the maximum parent strength sample. The average joint strength was 2212 N.

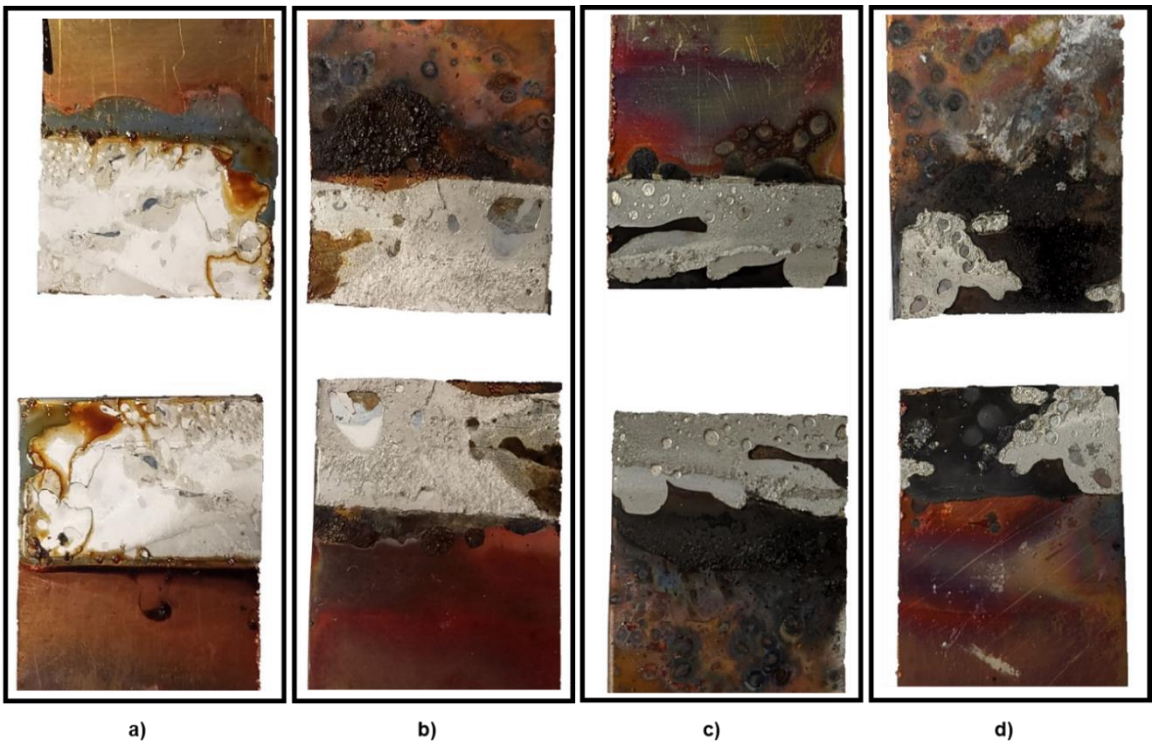

Figure 29 – Broken lap joint samples showing the solder coverage. The control sample can be seen in a), with samples 1, 3, and 6 shown in b), c), and d) respectively

Joint strength appears to be principally dictated by the solder dispersal at the joint. Figure 29 shows the solder coverage on four samples, three experimental and one control. Sample 1, seen in Figure 29b had excellent joint strength and almost complete coverage, much like the control sample seen in Figure 29a. Figure 29c shows sample 3, which has moderate solder coverage. This corresponds well with the sample's joint strength of 2760 N. Figure 29d shows an example of poor solder coverage. The corresponding sample (sample 5) had a strength of only 1225 N. The solder dispersal is controlled by both the heat source and by the setup of the joint. Since all of the experimental samples had similar heat sources, as generated by the thermite reaction, it is likely that the poor solder dispersal is caused by the joint setup itself. The experimental samples

did not have any fixturing to ensure even forces or flow, so an optimization of joint setup may decrease the variability in joint strength.

The post-ignition samples showed warping of the base material (less than 2mm out of plane). This deformation is due to the effects of the rapid and inherently uneven heating of the thermite ignition. However, the warping is trivial considering the thickness of the copper (.040") and the magnitude of the temperatures (upwards of 600°C at thermite-copper interface). We anticipate that this warping will likely not occur for thicker substrates. Even with the presence of warping, the resulting strength shows promise as a field expedient joining solution.

Conclusion

This work shows the viability of thermite-based reactive material architectures as a heat source for joining applications. The resulting soldered lap joints have an average strength of 2212 N, with sample strength strongly dependent on solder coverage. These samples show the potential of RMA's as a heat source for joining, creating viable joints with no specialized equipment and without a skilled operator. This process could be optimized for other materials and filler materials, as well as more complex joints and unique scenarios, like underwater or in-space joining.

Funding

This work was supported by the Naval Engineering Education Consortium (N00174-19-1-0020) and by the Tennessee Space Grant Consortium.

References

1. ASM (International). Van Nostrand's Sci. Encycl., 2005. doi:10.1002/0471743984.vse0687.

2. Siewert TA, Heine RW, Adams CM, Williams JR. The Skylab Brazing Experiment. Weld J 1977.

3. Masubuchi, K., & Anderssen, A. H. (1973, January 1). Underwater Application Of Exothermic Welding. Offshore Technology Conference. doi:10.4043/1910-MS

4. Chekunov IP. Exothermal Brazing of Steel Piping with High Temperature Brazing Alloys. Weld Prod (Eng Transl Svar Proizv 1972:39–42.

5. Weare NE, Long RA. Exothermically Brazed Hydraulic Fittings for Aircraft. Proc. AWS Natl. Fall Meet., 1966, p. 28–38.

6. Sullivan KT, Zhu C, Duoss EB, Gash AE, Kolesky DB, Kuntz JD, et al. Controlling Material Reactivity Using Architecture. Adv Mater 2016;28:1934–9. doi:10.1002/adma.201504286.

7. Fleck TJ, Murray AK, Gunduz IE, Son SF, Chiu GTC, Rhoads JF. Additive manufacturing of multifunctional reactive materials. Addit Manuf 2017:176–82. doi:10.1016/j.addma.2017.08.008.

8. McClain MS, Gunduz IE, Son SF. Additive manufacturing of ammonium perchlorate composite propellant with high solids loadings. Proc Combust Inst 2019;37:3135–42. doi:10.1016/j.proci.2018.05.052.

9. Chandru RA, Balasubramanian N, Oommen C, Raghunandan BN. Additive manufacturing of solid rocket propellant grains. J Propuls Power 2018;34:1090–3. doi:10.2514/1.B36734.

10. Braeuer J, Besser J, Tomoscheit E, Klimm D, Anbumani S, Wiemer M, et al. Investigation of different nano scale energetic material systems for reactive wafer bonding. ECS Trans 2012;50:241–51. doi:10.1149/05007.0241ecst.

11. Neely KE, Galloway KC, Strauss AM. Additively Manufactured Reactive Material Architectures as a Programmable Heat Source. 3D Print Addit Manuf 2019;00:1–7. doi:10.1089/3dp.2018.0077.

CHAPTER 5: ADDITIVELY MANUFACTURED REACTIVE MATERIAL ARCHITECTURES FOR EXOTHERMIC BRAZING

The following work has been submitted to *Additive Manufacturing*.

Abstract

Exothermic brazing uses the heat generated by an exothermic reaction to melt and flow filler material, but generally involves a fixture placed around the joint to hold the energetic material. Additive manufacturing can replace the fixture by creating a reactive material architecture that acts as a programmable heat source for the brazing process. This work demonstrates the additive manufacturing capabilities of a thermite-based reactive material architecture and shows its potential as a heat source for brazed copper joints.

Introduction

Exothermic brazing uses the heat generated by a solid-state or near solid-state reaction to melt and flow the filler material [1]. Exothermic brazing can be performed in austere environments, such as space or underwater, but has historically required complex setup or fixturing to hold the energetic material near the joint [2, 3, 4]. We hypothesize that the traditional and complex setup can be replaced with reactive material architectures (RMA's). Reactive material architectures are energetic material structures that control reaction characteristics through geometric characteristics – spacing, size, aspect ratio, etc. – rather than solely through changing the chemical composition of the energetic material.

Sullivan et al. showed that reaction rate could be controlled through the creation of thermite-based RMA's called hurdles and channels, but this deposition technique is limited to small nano-scale structures [5]. Fleck et al. and Ruz-Nuglo et al. also create thermite-based RMA's, but at a larger and more complex scale with polymer-based materials [6, 7].

Polymer-based additive manufacturing methods, such as FDM and resin based methods, are capable of printing complex geometries with high aspect ratios, overhangs, and unsupported angled builds. Continuous filament methods for polymer-based inks are also capable of high-aspect ratio prints, gap-spanning behavior, and overhangs [8,9].

Complex geometries are more difficult to print for materials with ceramic- or concrete-like behavior; however, recent advances in concrete 3D printing have resulted in complex structures. Gosselin et al. and Wolfs et al. have shown that real-time monitoring systems and other feedback controls can lead to stable, large scale prints [10, 11, 12]. Lim et al. also address the need for optimized path planning for each layer of concrete-based printing [13]. The field is maturing with paste based systems, which creates a wider range of possibilities for additively manufactured parts.

Most recently, we have developed and demonstrated a thermite-based reactive material paste with properties suitable for both printing and joining [14]. Our formulation, which exhibits a slow burn rate (3.19 mm/s), deposited sufficient for low-temperature soldering of copper lap joints [15]. This work presents multiple printing techniques for large-scale, high-aspect ratio printed structures using a thermite-based paste, and demonstrates an application of these structures towards high temperature brazing within copper joints.

Methods & Materials

3D Printing

The printing capabilities of the paste were explored in this work. The first print was a single-layer thick wall, printed until failure or until out of material. The first printed wall geometry was one layer in width (approximately 0.5 cm) and 10 cm in length. The second printed wall was also one layer in width, but 7 cm in length.

To expand printing capabilities beyond a single syringe, two other printing techniques were tested. The first consists of multiple sequential prints, from multiple syringes. First, a single cylindrical structure was printed. Immediately after the print concluded, the print head was leveled to the top of the previous print and a new print began with a new syringe of material. The structure does not cure between prints. For ease of reference, this will be referred to as sequential-uncured prints.

The second method consists of multiple sequential prints, allowing the structure to cure between each sub-structure. A single cylindrical structure was printed and allowed to fully cure on the build plate. After the structure cured, the print head was leveled to the top of the print and a new print began. The structure cures between print. This method will be referred to as sequential-cured printing

Brazing

To assemble the copper joint, 0.5 inch (12.7mm) copper pipe was cut into sections, cleaned with acetone and abraded, and then brazing paste with a melt temperature of 650 °C (Fusion STL-1205-655 Brazing Paste) was applied to the last 0.5 inches (12.7 mm) of each pipe. A copper

fitting was placed over the pipes to complete the joint. A cylindrical thermite architecture was placed over the fitting. The printed architectures have an inner diameter of 13.5 mm and are four layers in height (7.2 mm in height). The thermite paste used in this work is a 3:2:2 mass ratio of iron (II) oxide to aluminum to calcium hemihydrate, as outlined in previous work [14].

The cylindrical thermite piece was then placed over the entire assembly and the thermite fuse ignited with a blowtorch. A schematic of the joint setup can be seen in Figure 30.

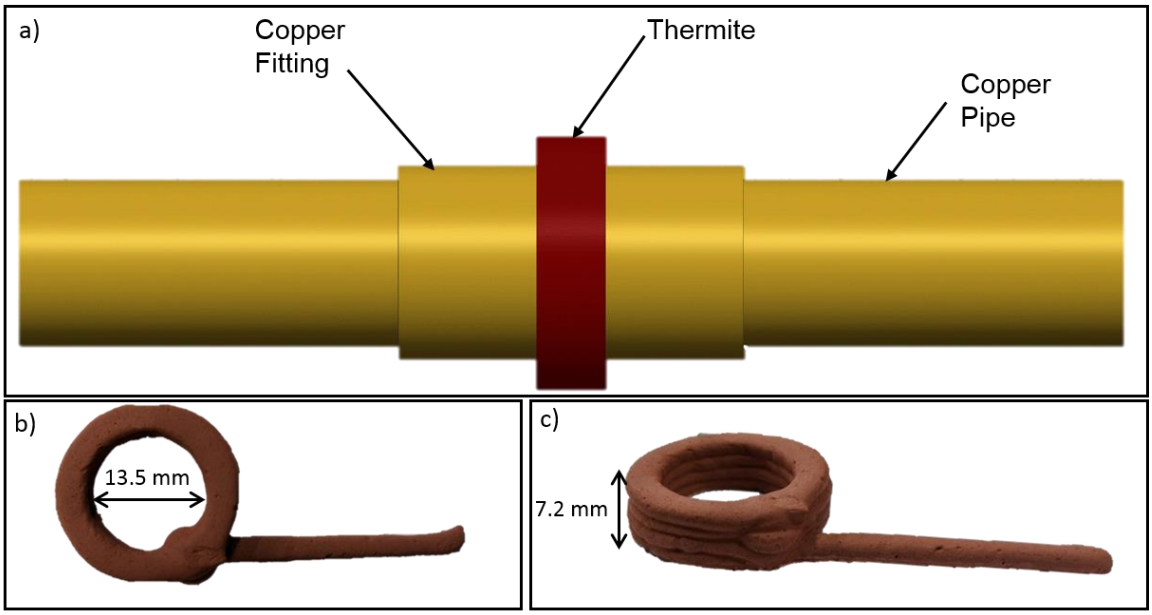

Figure 30 - Schematic of joint setup showing the copper fitting over the copper piper, with the thermite placed over the fitting, b) top view of thermite structure, and c) isometric view of thermite structure

Nine samples were created and tested, with the corresponding thermite mass shown in Table 6. Mass of thermite highly corresponds with maximum temperature, with mass selections guided by both the size of the pipe and by temperature data collected in [15]. For this work, thermite

masses of approximately 7-10 grams were previously experimentally determined to achieve temperatures near 650 °C.

Sample	Mass Thermite (g)
1	8.9
2	8.4
3	8.0
4	8.6
5	8.3
6	7.2
7	7.1
8	9.7
9	10.1

Table 6 – Mass of thermite and its corresponding sample number. The masses range from 7.1 to 10.1 grams.

Tensile Testing Brazed Copper Joints

All the brazed copper pipe joints were tested in a tensile tester at a rate of 2 mm/min. To secure the joints in the tensile tester, the ends were clamped flat using an arbor press and then clamped into the tensile tester.

Results & Discussion

3D Printing

The first successful thin wall, with dimensions of 10x0.5x3 cm, can be seen in Figure 31.

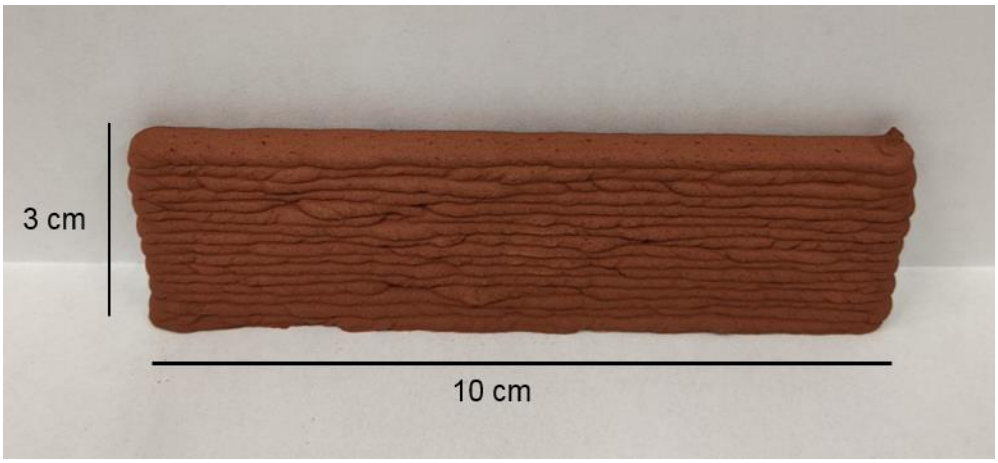

Figure 31 – Printed thermite wall, with dimensions 10x0.5x3 cm

This print was stopped not because the wall became unstable, but because the syringe ran out of material. From these results, a second wall was printed with base dimensions of 7x0.5 cm. This structure reached 26 layers in height (4.68 cm) before it became unstable and fell over. Figure 32 shows the structure immediately before collapse.

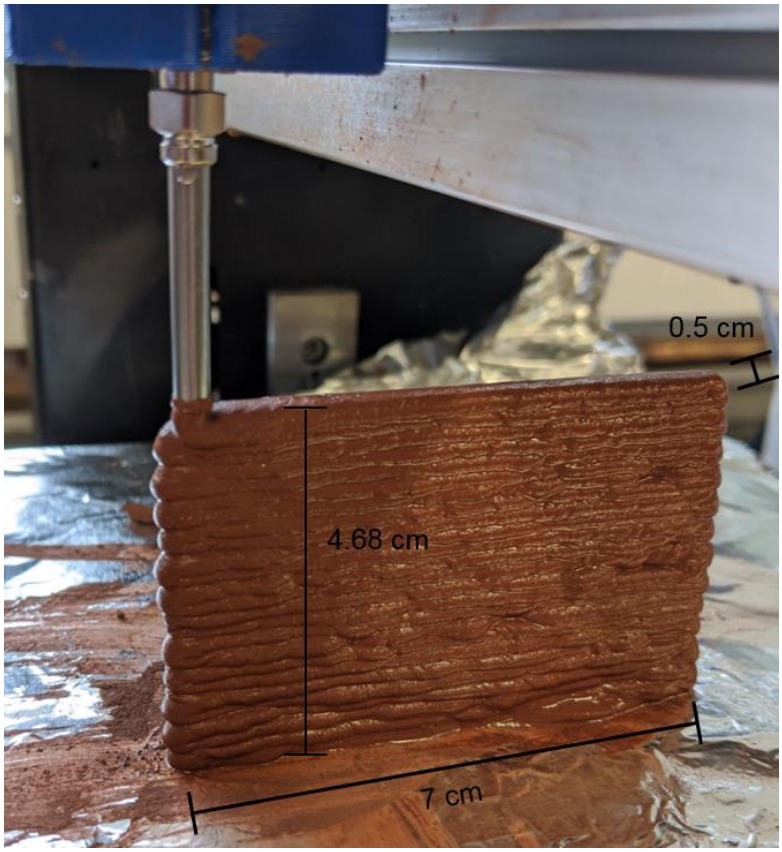

Figure 32 – Second high aspect ratio print, immediately before collapse

The sequential-uncured and sequential-cured printing techniques are similar. The sequential-uncured method consists of multiple immediately sequential uncured prints. The sequential-cured technique also consists of multiple sequential prints, but the structures are allowed to cure between prints. These methods can be used to print structures that require more paste volume than can currently be contained in a single syringe.

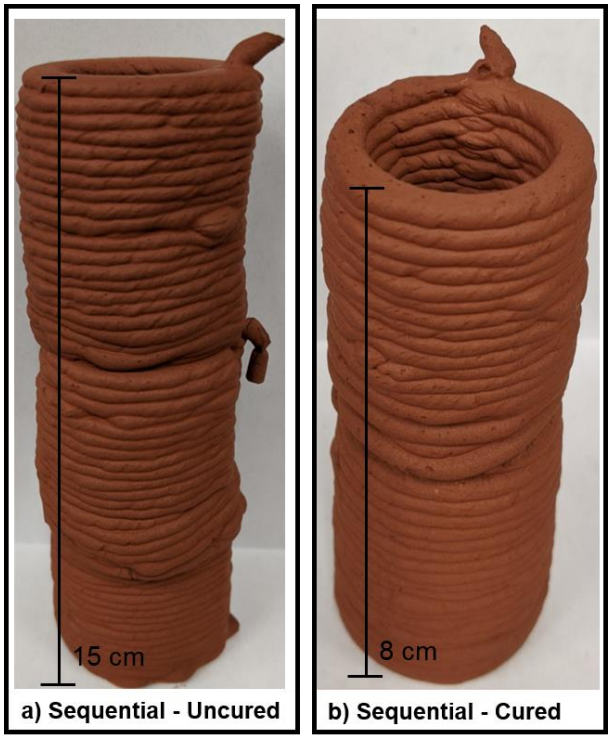

Figure 33– Cylindrical prints created using a) the method of sequential uncured prints and b) the print method of sequential cured prints

Figure 33a shows a cylinder printed using the sequential-uncured technique, with the structure reaching a height of 15 cm. There is some sagging and deformation of the print along the z-axis. This is because the structure itself is composed of multiple consecutive prints on an uncured base. The base itself can deform in the z-direction from the weight of additional layers. It can also shift in the x- and y-direction as the bed moves. This, combined with the leveling step between prints, results in the current print not being perfectly aligned with the previous print. However, the paste has a tendency to self-correct while printing, filling in any gaps or voids caused by insufficient paste extrusion or shifting of the base layer.

The structure printed with sequential-cured technique, shown in Figure 4b, results in a more uniform structure without significant sagging or deformation of the print along the z-axis. The

cured structure is more stable than the uncured sample, so the base doesn't shift from the weight of additional layers or from the bed movement. The second print can also be leveled more precisely because there is no danger of shifting the original print with the nozzle.

Overall, this thermite-based paste is capable of creating large structures. The sequential-uncured technique is valuable when large structures need to be created in a short period of time. However, the parts are prone to mass-related deformation and sagging along the z-axis. The sequential-cured technique is also capable of creating large structures without significant mass-related deformation and sagging at the expense of a longer overall print time. If a larger print reservoir can be integrated into a print system, then these techniques will only be necessary for very large prints.

Brazing

Nine pipe joining samples were created for the purpose of testing the functionality of thermite architectures in two criteria: as a heat source for high temperature joining and as a heat source for unique joint configurations.

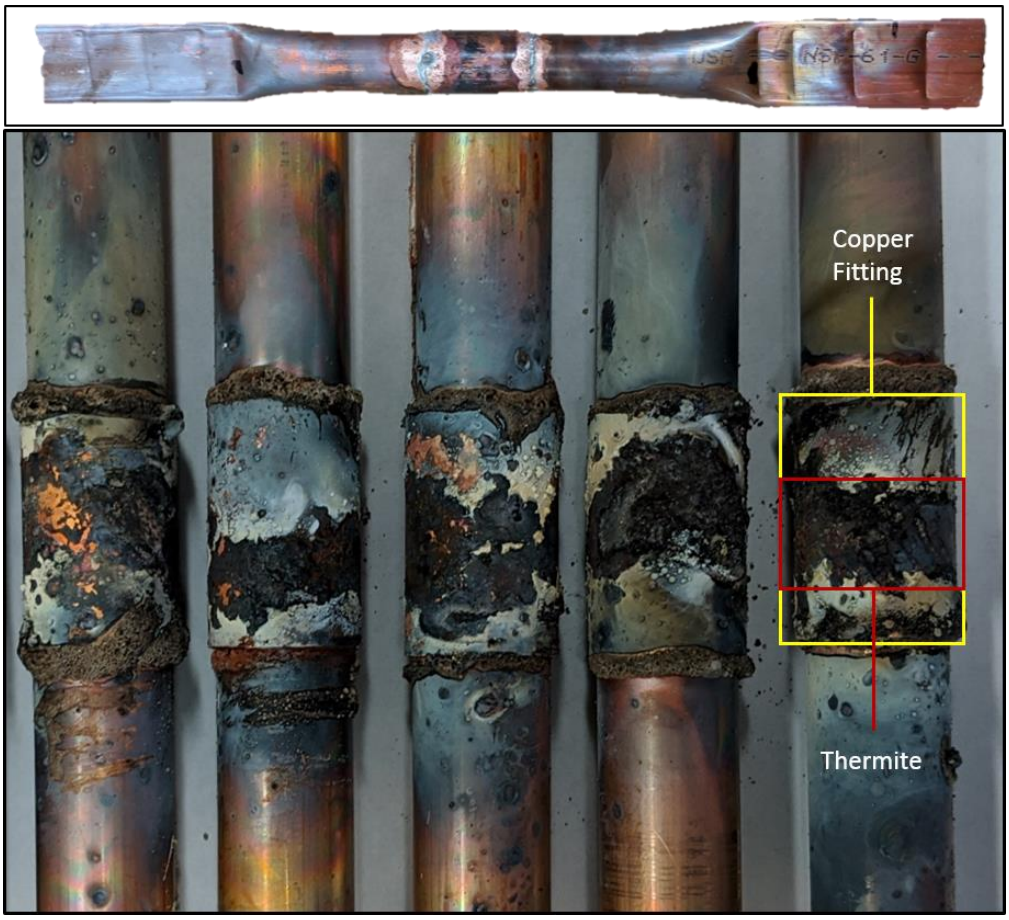

Figure 34 - Select pipe joining samples. There is some slag and discoloration at and near the joint, caused by the thermite reaction.

Figure 34 shows selected pipe joining samples before tensile testing. The thermite reaction causes a brief, intense heat at the joint. This generates enough heat through the copper fitting to melt the brazing paste. Since copper is highly thermally conductive, this heat is also transmitted further down the pipe, causing some of the copper oxidation related discoloration seen in Figure 34. The lighter discoloration is caused by the gas emitted by the thermite reaction. Overall, the joined region is visually messy, but the joint integrity is not affected by these discolorations.

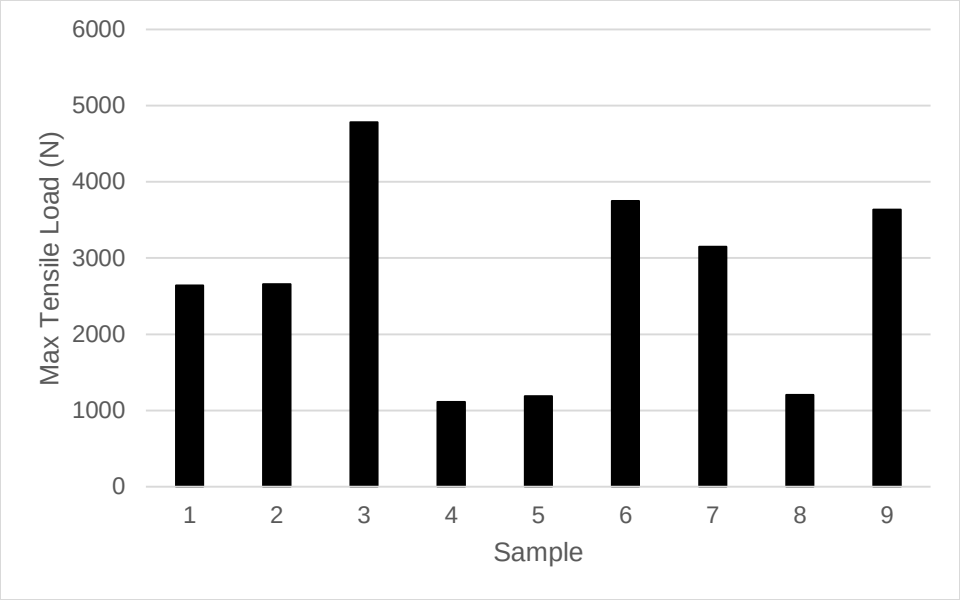

Figure 35 – Maximum tensile load before failure for all tested pipe joints

The tensile testing results can be seen in Figure 6. The average measured joint strength is 2680 N, with a maximum measured joint strength of 4781 N and a minimum. The joint strength does not vary with mass, but likely varies based on brazing paste coverage. The thermite reaction is highly energetic, so the uneven heating and cooling could cause an uneven dispersal of brazing paste in the joint. To avoid this uneven dispersal, more brazing paste should be applied at the joint and on the edges of the copper fitting. Additionally, these samples were all tested in tension, with the ends of the pipe pressed flat to fit into the tensile tester. The samples were clamped flat far from the joint area, but the pressing could still impart a stress at the joined area. If the samples were tested in their round shape, the joint strength would likely be higher.

Conclusion

This work shows the viability of several different printing methods used to created larger architectures than previously shown. The two techniques are outlined in this work, sequential-uncured printing and sequential-cured printing, can be used to create prints of larger volume than a single syringe. These techniques could also be used to create more complicated prints. Using the sequential-cured printing method, an initial print could be created, cured, then rotated and then printed a different surface.

These printing techniques can be used to create architectures used in exothermic brazing. The work here has demonstrated the capabilities of thermite-based RMA's as a programmable heat source for high-temperature joining. While the joints created here were made with copper, a highly thermally conductive material, the work could be scaled to less conductive materials by using larger RMA's or higher masses of thermite.

Overall, this thermite-based reactive material paste shows great potential as a programmable heat source for exothermic brazing. These RMA's could replace the fixtures holding the energetic material that has previously been used in exothermic brazing, potentially simplifying the process. This, combined with sequential-cured and sequential-uncured printing processes, has expanded the potential applications of this thermite-based reactive material paste.

Acknowledgements

The author wishes to thank Garrett Thorne and the Laboratory for Systems Integrity and Reliability for their assistance in obtaining tensile data. This work was funded by the United

States Naval Sea Systems Command (NAVSEA) through the Naval Engineering Education Consortium (NEEC) Grant #N00174-19-1-0020.

References

[1]ASM (International), in: Van Nostrand's Sci. Encycl., 2005. doi:10.1002/0471743984.vse0687.

[2]T.A. Siewert, R.W. Heine, C.M. Adams, J.R. Williams, The Skylab Brazing Experiment, Weld. J. (1977).

[3]I.P. Chekunov, Exothermal Brazing of Steel Piping with High Temperature Brazing Alloys, Weld. Prod. (Eng. Transl. Svar. Proizv. (1972) 39–42.

[4]N.E. Weare, R.A. Long, Exothermically Brazed Hydraulic Fittings for Aircraft, in: Proc. AWS Natl. Fall Meet., 1966: pp. 28–38.

[5]K.T. Sullivan, C. Zhu, E.B. Duoss, A.E. Gash, D.B. Kolesky, J.D. Kuntz, J.A. Lewis, C.M. Spadaccini, Controlling Material Reactivity Using Architecture, Adv. Mater. 28 (2016) 1934–1939. doi:10.1002/adma.201504286.

[6]T.J. Fleck, A.K. Murray, I.E. Gunduz, S.F. Son, G.T.C. Chiu, J.F. Rhoads, Additive manufacturing of multifunctional reactive materials, Addit. Manuf. (2017) 176–182. doi:10.1016/j.addma.2017.08.008.

[7]F.D. Ruz-Nuglo, L.J. Groven, 3-D Printing and Development of Fluoropolymer Based Reactive Inks, Adv. Eng. Mater. (2018). doi:10.1002/adem.201700390.

[8]Ahn BY, Walker SB, Slimmer SC, Russo A, Gupta A, Kranz S, et al. Planar and three-dimensional printing of conductive inks. J Vis Exp 2011:1–8. doi:10.3791/3189.

[9]Lewis JA. Direct ink writing of 3D functional materials. Adv Funct Mater 2006;16:2193–204. doi:10.1002/adfm.200600434.

[10]C. Gosselin, R. Duballet, P. Roux, N. Gaudillière, J. Dirrenberger, P. Morel, Large-scale 3D printing of ultra-high performance concrete - a new processing route for architects and builders, Mater. Des. 100 (2016) 102–109. doi:10.1016/j.matdes.2016.03.097.

[11]R. Wolfs, F. Bos, E. van Strien, T. Salet, A Real-Time Height Measurement and Feedback System for 3D Concrete Printing, High Tech Concr. Where Technol. Eng. Meet - Proc. 2017 Fib Symp. 1 (2017) v. doi:10.1007/978-3-319-59471-2.

[12]F. Bos, R. Wolfs, Z. Ahmed, T. Salet, Additive manufacturing of concrete in construction: potentials and challenges of 3D concrete printing, Virtual Phys. Prototyp. 11 (2016) 209–225. doi:10.1080/17452759.2016.1209867.

[13]S. Lim, R.A. Buswell, T.T. Le, S.A. Austin, A.G.F. Gibb, T. Thorpe, Developments in construction-scale additive manufacturing processes, Autom. Constr. (2012). doi:10.1016/j.autcon.2011.06.010.

[14]K.E. Neely, K.C. Galloway, A.M. Strauss, Additively Manufactured Reactive Material Architectures as a Programmable Heat Source, 3D Print. Addit. Manuf. (2019). doi:10.1089/3dp.2018.0077.

[15]K.E. Neely, K.C. Galloway, A.M. Strauss, Soldered copper lap joints using reactive material architectures as a heat source, Manuf. Lett. (2020). doi:10.1016/j.mfglet.2020.02.002.

CHAPTER 6: CHEMICAL EQUILIBRIUM SIMULATIONS

Introduction

NASA CEAM uses several equations and assumptions, which are detailed here. First, all gases are assumed ideal, and that interactions between phases are negligible. These assumptions can be considered correct even when small amounts of condensed species are present. The reactants considered for NASA CEAM can be seen below,

$$Al + Fe_2O_3 + CaSO_4 \qquad (2)$$

where aluminum is the oxidizer, and both iron oxide and calcium sulfate are the fuel. Calcium sulfate also acts as the binder for additive manufacturing. For NASA CEAM, the salient parameters are the oxidizer to fuel ratio (O/F) and the fuel composition. Since the fuel is composed of two components, we can express the fuel composition as weight percent iron oxide (Fe_2O_3). The weight percent calcium sulfate is and weight percent iron oxide must sum to 100%. It is important to note that this is the weight percent of the fuel only.

Tested Thermite Compositions

The work in this dissertation shows several successful thermite compositions. Table 7 shows each thermite composition and its corresponding O/F ratio and weight percent iron oxide.

Mass Ratio $Fe_2O_3 : Al : CaSO_4$	O/F ratio	Fuel Weight Percent		Mass Fraction		
		Fe_2O_3	$CaSO_4$	Fe_2O_3	Al	$CaSO_4$
0:2:3	1.5	0%	100%	0.00	0.40	0.60
3:2:2	2.5	60%	40%	0.43	0.29	0.29
3:2:1	2	75%	25%	0.50	0.33	0.17
3:2:0.5	1.75	85.7%	14.3%	0.55	0.36	0.09
3:2:0.1	1.55	96.8%	3.2%	0.59	0.39	0.02

Table 7 – Tested thermite compositions and their corresponding mass ratio, O/F ratio, and weight percent Fe_2O_3

With the goal of evaluating what mixtures were both printable and reactive, an array of variables had to be examined independently. Initial reactants were composed of a constant mass of Fe_2O_3 and Al, with decreasing levels of calcium sulfate. Each tested condition has a different O/F ratio and a different fuel weight percent Fe_2O_3. To determine the effects of o/f ratio and weight percent Fe_2O_3, three sets of simulations were calculated. The first set of simulations tested a range of weight percent Fe_2O_3 from 0-100% and held O/F ratio constant. The second tested a range of O/F ratios from 1-3 and held weight percent Fe_2O_3 constant. The final simulation tested a combination of all O/F ratios from 1-3 and all weight percent Fe_2O_3 values from 0-100%. Simulation results include adiabatic flame temperature, and mass fraction of products.

Adiabatic Flame Temperature and Reaction Rate

The first parameter examined is adiabatic flame temperature, the temperature from a complete combustion assuming constant volume and constant pressure. Figure 36 shows the adiabatic flame temperature for a range of weight percent Fe_2O_3 and for select isolines of the O/F ratio, while Figure 37 shows the adiabatic flame temperatures for a range of O/F ratios and select weight percents Fe_2O_3.

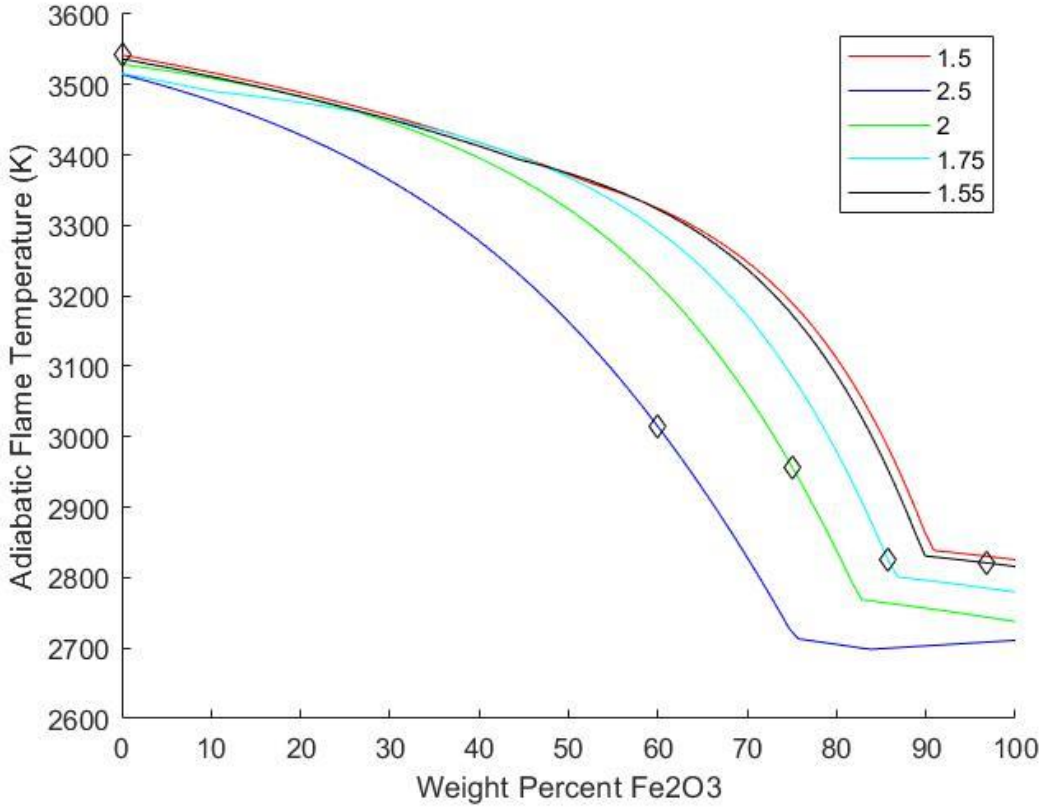

Figure 36 - Adiabatic flame temperature (K) with respect to weight percent Fe_2O_3. The diamond markers indicate experimental conditions

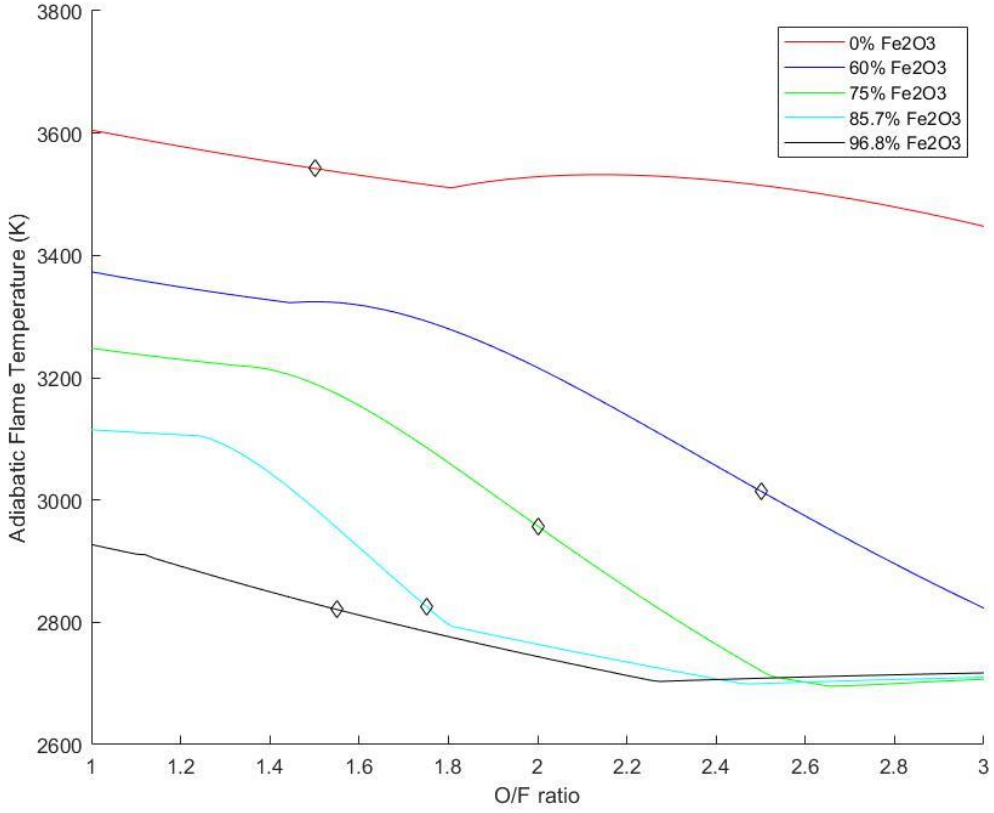

Figure 37 - Adiabatic flame temperature (K) with respect to O/F ratio. The diamond markers indicate experimental conditions.

These two figures show noteworthy trends. Weight percent Fe_2O_3 and adiabatic flame temperature are inversely proportional. However, the mixtures were not selected to optimize adiabatic flame temperature, nor were they selected for specific combinations of O/F ratio or fuel weight percent Fe_2O_3. These mixtures were selected to test the effects of weight percent $CaSO_4$ (plaster) on the reaction rate. Generally, a lower weight percent binder resulted in a faster reaction rate, with a decreasing exponential relationship. This is shown in Figure 38, with the diamond markers indicating experimental reaction rates. The line denotes simulation results estimated reaction rates for different weight percent $CaSO_4$. More detail on how this information

was obtained is discussed in Chapter III. As expected, fuel composition and reaction rate are correlated, as well as fuel composition and adiabatic flame temperature. A less intuitive result is observed for the relationship between reaction rate and adiabatic flame temperature is shown in Figure 39.

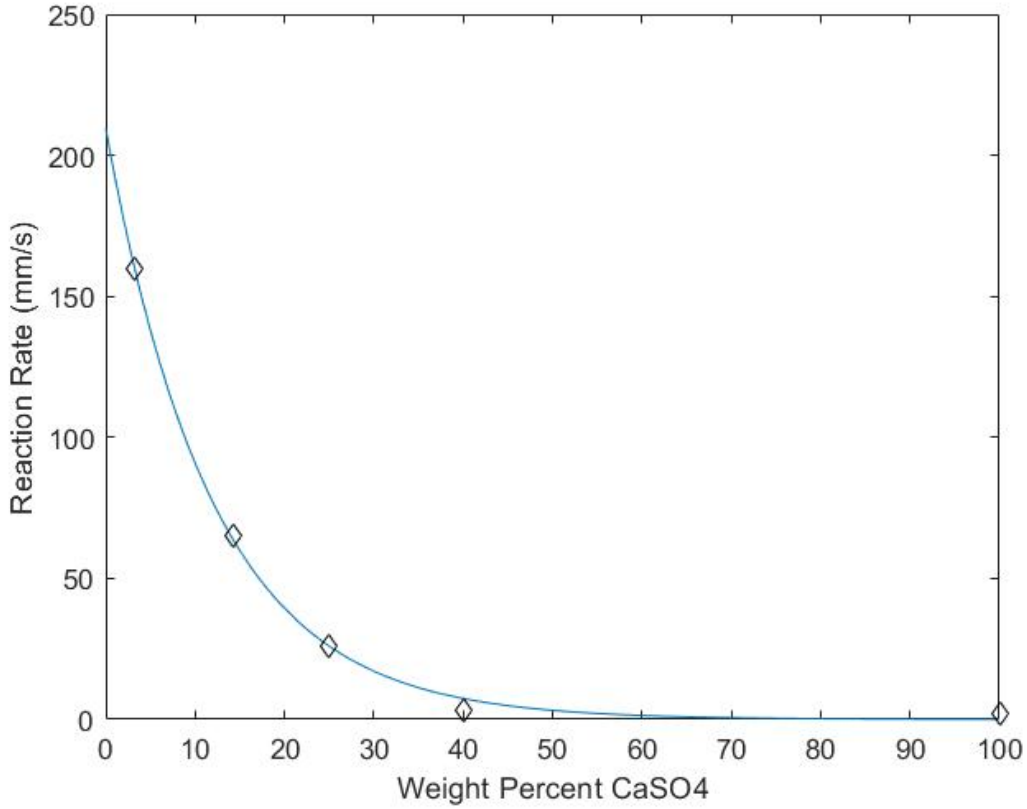

Figure 38 - Reaction rate (mm/s) with respect to weight fraction $CaSO_4$. The diamond markers indicate the specific measured cases.

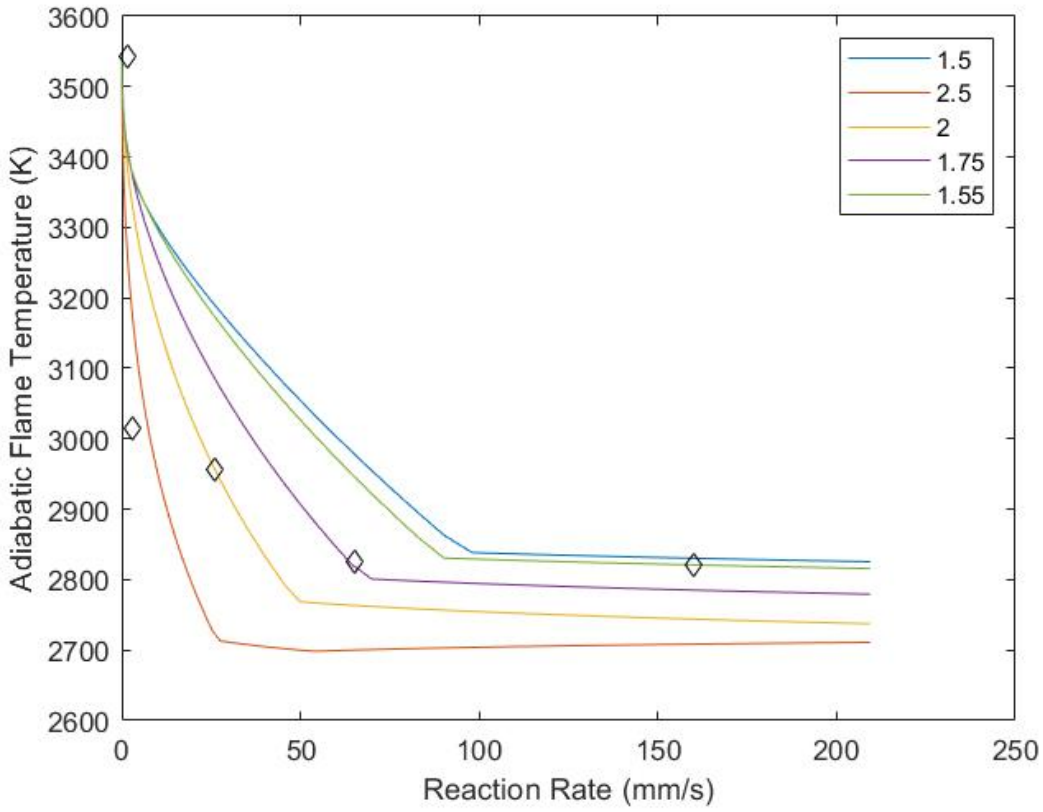

Figure 39 - Adiabatic flame temperature (K) vs reaction rate (mm/s). The diamond markers indicate specific cases.

Figure 39 provides insight to the oxidation of the two separate fuels in tandem. This reaction is composed of two separate reactions, aluminum and iron oxide and aluminum and calcium sulfate. The behavior of the overall process is dependent on the dominating reaction. When the calcium sulfate reaction dominates, reaction rates are very slow, but the adiabatic flame temperature is very high. When the iron oxide reaction dominates, temperatures are lower, but the reaction rates are orders of magnitude higher. The figure also shows an interesting discontinuity for each O/F ratio simulated. For each case, the adiabatic flame temperature

decreases until reaching this point and then remains fairly constant. The reaction rate then continues to increase despite the nearly constant temperature.

Figures 40 and 41 show relationships between weight percent binder, reaction rate, and adiabatic flame temperature for a series of constant O/F ratios. Creating mixtures with O/F ratios other than those tested will likely result in more information regarding the relationship between reaction rate and temperature. If the experimental case with no iron oxide is neglected, there is a measured experimental relationship between O/F ratio and reaction rate, with $R^2 = 0.99$.

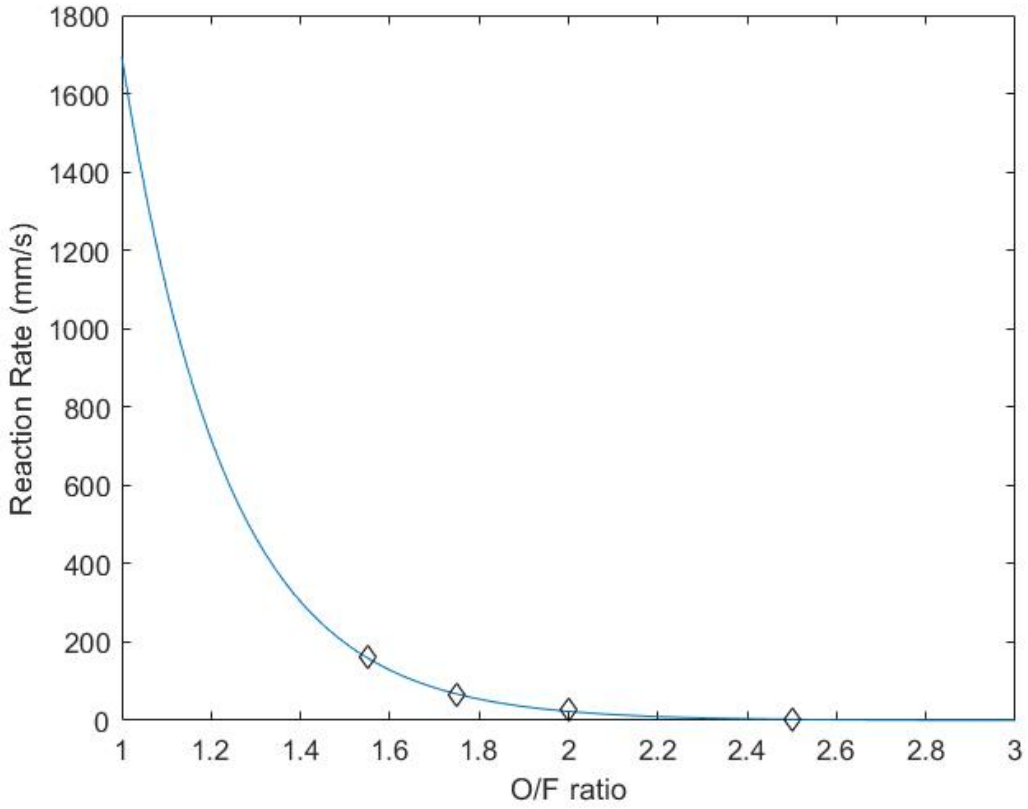

Figure 40 - Reaction rate (mm/s) with respect to O/F ratio, with the diamond markers indicated experimental measurements

Once again, this shows a relationship between reaction rate, O/F ratio, and adiabatic flame temperature.

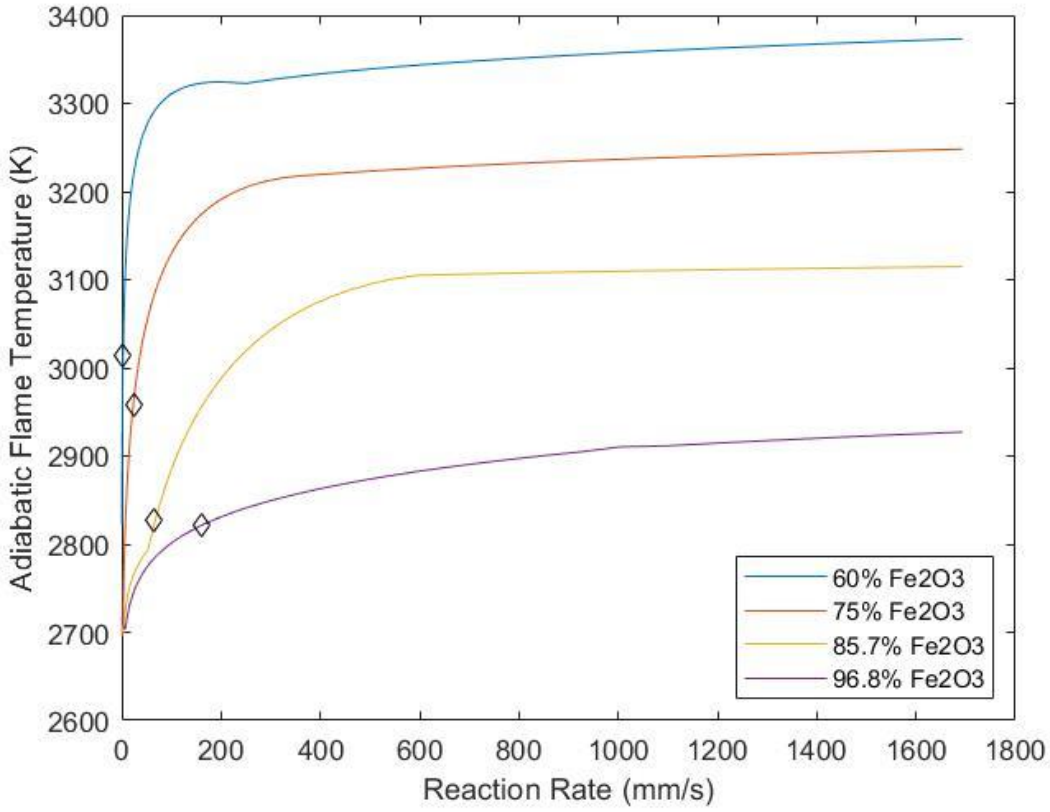

Figure 41 - Adiabatic flame temperature (K) with respect to reaction rate (mm/s) for a range of o/f ratios and fixed weight percent iron oxide. The diamond markers indicate specific tested cases.

Figure 41 shows that for a given weight percent iron oxide (therefor fixed weight percent binder and a variable O/F ratio), reaction rate increases as temperature increases. This relationship is unlikely to increase drastically and infinitely, as the figure shows, but nevertheless the trend appears to hold in the experimentally tested range.

Phase Changes

Figures 39 and 41 reveal interesting discontinuities with respect to adiabatic flame temperature and reaction rate. These temperature discontinuities are likely caused by phase changes of major species during the reaction.

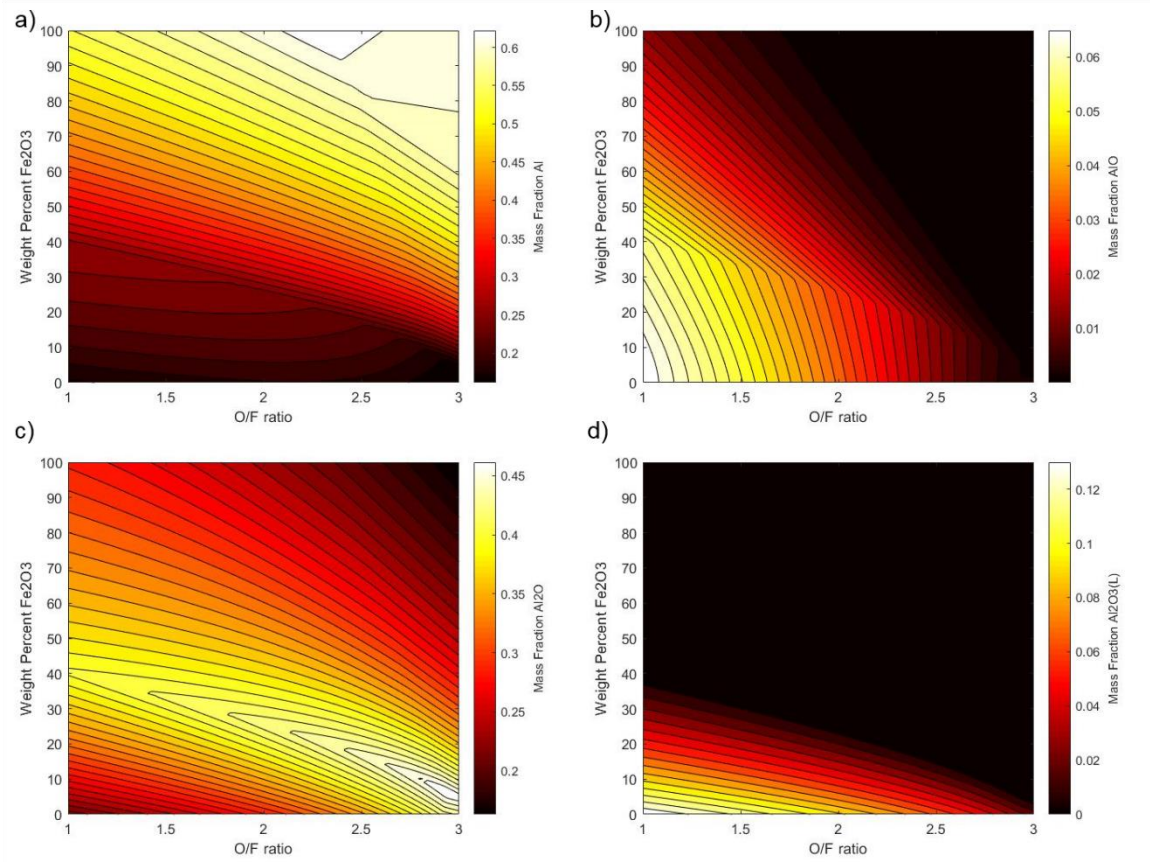

Figure 42 - Mass fraction of species for varying O/F ratios and varying weight percent Fe_2O_3, with a) depicting Al, b) AlO, c) Al_2O, and d) Al_2O_3 (L)

Figure 42 show the mass fraction of aluminum (Al), aluminum (I) oxide (Al_2O), aluminum (II) oxide (AlO), and the liquid form of aluminum (III) oxide (Al_2O_3). Darker areas correspond to low mass fraction of the species and the lighter areas correspond to a higher mass fraction.

These results illuminate the temperature discontinuities shown in earlier figures (1-2, 4, 6). As the excess reactant, aluminum mass fraction is a logical variable to first examine for these discontinuities. Three separate bands are observed. The first is a lower plateau near 0.30, which turns to a sharp gradient until a mass fraction of roughly 0.5 is reached. Here the third band, an upper plateau, begins to extend. Turning to other aluminum compounds – typically unstable gaseous intermediates such as AlO and Al_2O – the lower plateau of the aluminum surface is outlined. The high concentration of intermediates indicates excess energy (therefore high temperatures), but do not fully explain the temperature discontinuity. Instead, the leveling of temperature is explained by melting of Al_2O_3 and required energy absorption.

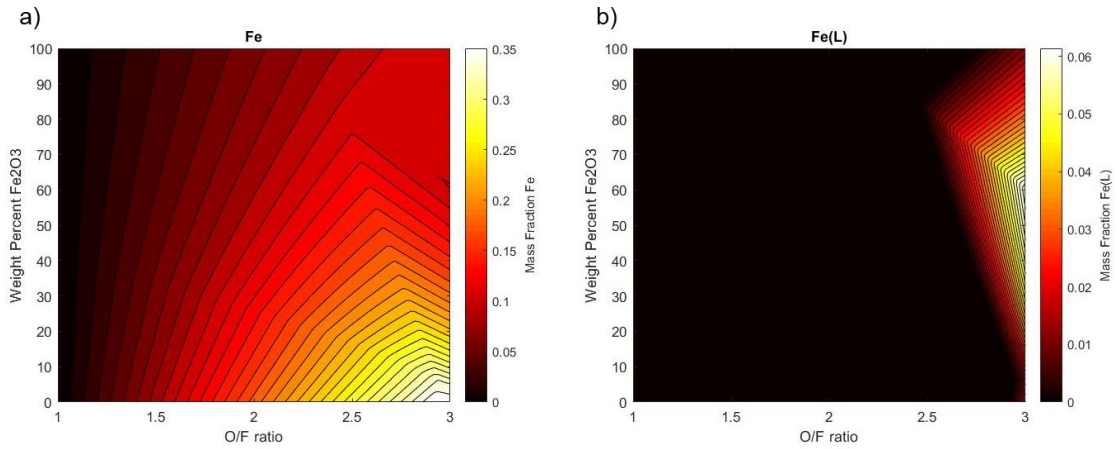

Figure 43 - Mass fraction of species for varying O/F ratios and varying weight percent Fe_2O_3, with a) showing Fe and b) showing Fe(L)

Moving to the plateau of aluminum, a similar process occurs. While the reaction temperature is greater than that required for Al_2O_3 to melt, it is not present in liquid form (and is negligible in solid form). Alternatively, liquid iron forms. At both high reactant mass fractions of Fe_2O_3 and Al, excess energy in the system again causes phase change for pure iron.

Clearly, reaction rate varies with respect to both O/F ratio and with respect to the composition of the fuel. Adiabatic flame temperature varies with respect to O/F ratio and with respect to the composition of the fuel. Ideally, this would result in two guiding surfaces, where an individual could select an O/F In addition, the user can select a mixture to limit products to solid and gaseous states or to form a liquid intermediate compound to increase heat transfer from the reaction. Further experimental data is required to fully validate and mathematically determine reaction rate as a function of both O/F ratio and weight percent Fe_2O_3. Adiabatic flame temperature with respect to O/F ratio and weight percent Fe_2O_3 can be seen in Figure 44.

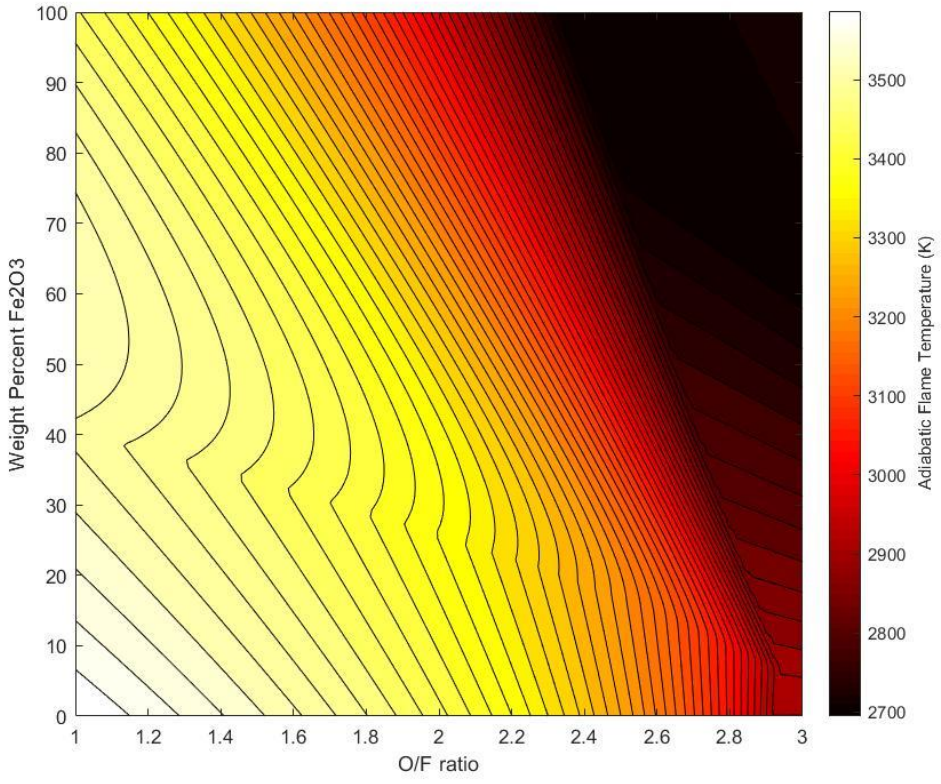

Figure 44 - Adiabatic Flame Temperature (K) with respect to o/f ratio and weight percent Fe_2O_3

Figure 44 creates a guideline for selecting an energetic for temperature related characteristics. An end-user could select an O/F ratio and a weight percent Fe_2O_3 based on desired temperature and desired printing qualities.

Products

NASA CEAM is also capable of predicting the resulting species and mass fractions of said species for a given reaction. Figure 45 shows the predicted species and mass fractions for all thermite compositions listed in Table 7.

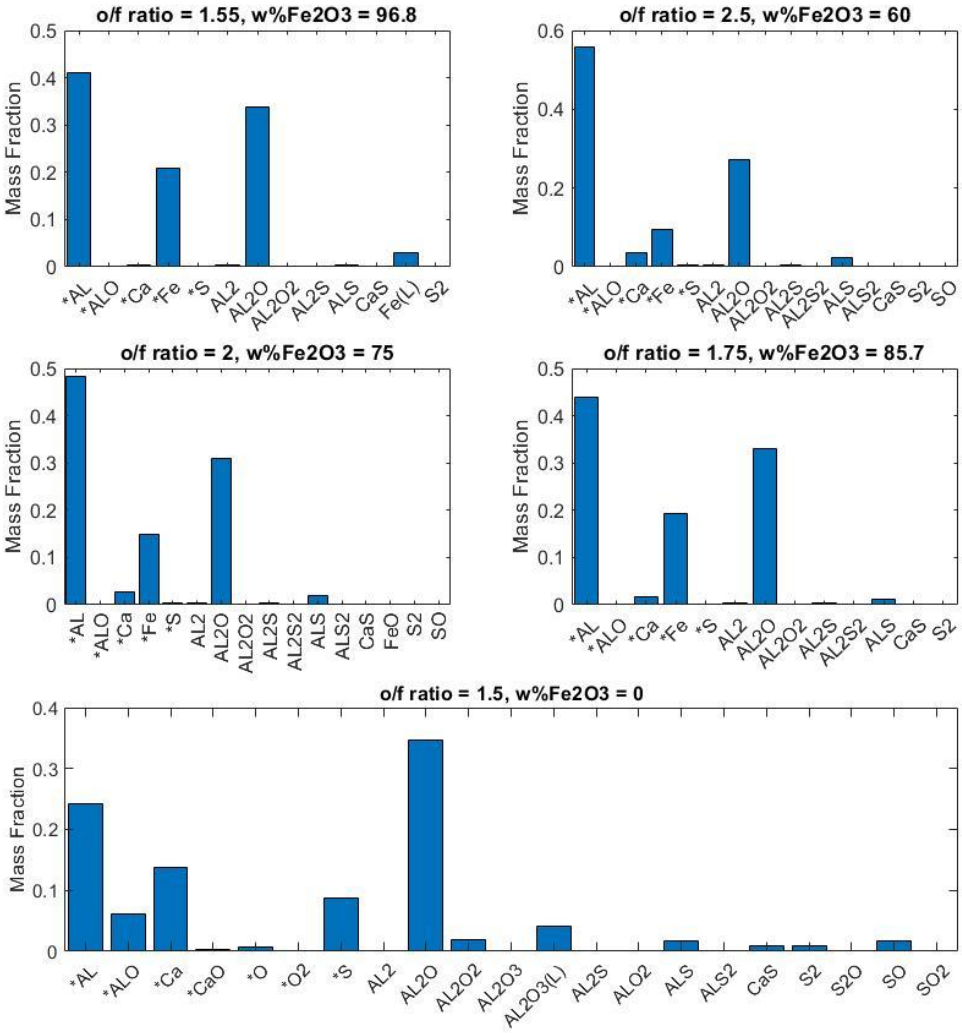

Figure 45 - Predicted species and their corresponding mass fractions for each experimentally tested thermite mixture

The predicted species and their corresponding mass fractions show some notable trends. Aluminum, aluminum (I) oxide (Al_2O), and iron compose the majority of the resulting species in all cases except for the sample with no iron oxide. The sample with 100% weight percent $CaSO_4$

has products that are primarily aluminum, aluminum (II) oxide, aluminum (I) oxide, calcium, and sulfur. This difference is due to the lack of iron oxide in the reaction, which contributes in part to higher reaction temperature and molten products.

The species can be predicted for any combination of O/F ratio and weight percent iron oxide. For brevity, all predicted species and corresponding mass fractions are not depicted in this work.

Conclusion

With the aid of thermochemical equilibrium software like CEAM, a wide range of reaction-specific behavior can be predicted. This data, combined with experimentally derived data like reaction rate, creates a wide range of potential printable, reactive mixtures. Several conclusions can be drawn from this data. First, adiabatic flame temperature is a function of O/F ratio and weight percent Fe_2O_3, and increases as O/F ratio decreases and as weight percent Fe_2O_3 decreases. Second, reaction rate is a function of both O/F ratio and weight percent Fe_2O_3. As weight percent Fe_2O_3 increases, reaction rate increases. As O/F ratio increases, reaction rate decreases. An experimental fit of reaction rate as a function of both O/F ratio and weight percent Fe_2O_3 is not presented in this work, but is possible given sufficient data. Therefore, given a combination of o/f ratio and weight percent Fe_2O_3, it is possible to (1) predict both adiabatic flame temperature and reaction rate and (2) control or limit intermediate phase change for a given mixture. This, combined with reactive material architectures, represents a programmable heat source of a wide range of heat deposition capabilities.

CHAPTER 7: CONCLUSIONS AND FUTURE WORK

Conclusions

Overall, this work represents the foundation of future research in low-cost, novel thermite-based architectures. The processing and applications of the work presented here is not an exhaustive list of applications and possibilities. Rather, this work is an exploration of additive manufacturing techniques presented in the context of energetic materials and their joining applications. This work also shows key design considerations when creating RMA's for any applications, but specifically for multi-material printing and joining applications.

The research presented in Chapter 2 establishes baseline reaction and architecture behavior necessary for every other chapter in this dissertation, and for any future research regarding this composition. First, this chapter details the creation and formulation of a thermite paste. This composition detailed in that chapter is generally considered novel, and to the authors knowledge has never been printed before. A key finding in regards to the formulation is the inclusion of tartaric acid in the mixture to retard curing. Without the tartaric acid, the mixture cures too quickly to print. Additional formulation specific properties include cure time, viscosity, and printing parameters.

Chapter 2 also shows fundamental architecture behavior for a specific thermite composition, namely parallel and series adjacent ignition. Parallel and series adjacent ignition, defined as the propensity of an ignited section of thermite to cross a gap and ignite a non-ignited section in either series or parallel, are a key design parameter. This phenomenon is dependent on thermite composition, cross-sectional area of geometric features, and the spacing of geometric features. End-users can design to avoid this functionality, in the application of precision timed fuses or

tailored heat deposition, or take advantage of this phenomenon and build in redundancy into their reactions. Interestingly, this work also showed that for the range of tested cross-sectional areas the average reaction rate did not change. The variability of the reaction rate decreased as the cross-sectional area increased, which is another important design parameter when creating precisely timed systems.

Part of the research documented in Chapter 3 addressed unique multi-material additive manufacturing techniques to create composite energetics. The quick curing time of the paste, as detailed in Chapter 2, makes multi-material prints difficult. Generally, multi-material prints would consist of multiple syringes and multiple nozzles, each consisting of a different formulation. This work shows the viability of a multi-material print from a single syringe and documents the unique behavior. When two materials are layered in a syringe, three distinct material regions occur created by the fluid flow within the syringe. The first region is entirely material one, the second region is an intermediate phase of both materials, and the third region is entirely the second material. If a sharp transition is needed in the multi-material structure, then the intermediate phase is likely a detriment. However, this region could be used to create a composite with gradient properties at the area of mixed phase flow.

Additionally, Chapter 3 addresses the reaction properties of composite thermite structures. A new thermite mixture is detailed in this section, with titanium as the oxidizer instead of aluminum. The binder mass fraction was altered for both aluminum-based and titanium-based thermite, creating multiple printable mixtures with different reaction rates. These different mixtures were then placed in series and ignited. Each section of the composite retained its unique behavior while still being part of the entire reaction system. The results of Chapter 3 pertain to fundamental printing processes and the behavior of these thermite mixtures with

respect to the entire system, and therefore lay the groundwork for future applications. The combination of thermite compositions into a composite structure expands the flexibility of thermite-based RMA's, and therefore expands the applications of this material. A single structure composed of very fast reacting thermite and very slow reacting thermite could be used to create a variable heat deposition with a simpler architecture or could be used as part of a complex timing circuit. The multi-material printing from a single syringe can also be used as a starting point for any highly viscous multi-material printing, not just energetics.

Chapters 4 and 5 address joining applications using reactive material architectures as a heat source. Chapter 4 shows an initial low-temperature proof of concept. Initial temperature data was measured using a thermocouple through a copper substrate to prevent the thermocouple from being destroyed by the high temperatures reached by the thermite reaction. This data was then used to select masses of thermite for copper joining applications seen in both Chapter 4 and 5. Initial lap joint results showed joints comparable to traditionally soldered joints, but showed minor warping from the rapid heating and cooling of the flat copper plate. However, the pipe joints created in Chapter 5 showed no warping or deformation from temperature.

Chapter 5, in addition to testing high temperature brazing applications, addressed more printing techniques and characteristics for the thermite paste. Very large and high aspect ratio prints were created to test the bounds of the printing capabilities. Traditional syringe printing can result in high aspect ratio prints, but are limited by the volume capacity of the syringe. If a smaller capacity syringe is employed, two different print techniques can be used, sequential-uncured printing and sequential-cured printing. The first is multiple immediately sequential prints, each being leveled at the end height of the previous print, can be used to created larger structures. The second technique is multiple sequential prints, but the previous layers are allowed to fully cure

before starting the second print. These methods could be used to create large, complex structures necessary for the exothermic brazing of unique joints.

The joints created in Chapter 5 were round, therefore needing a round thermite architecture to melt the brazing filler material. This is perhaps the most important result from both Chapter 4 and 5: a brazed joint was successfully created via exothermic brazing without a fixture holding the energetic around the joint. Instead, the thermite architecture provided sufficient structure for the energetic and held it around the joint during ignition. This shows that reactive material architectures greatly simplify exothermic brazing. Instead of creating and installing, and then removing complex fixtures for every exothermically brazed joint, a single reactive material architecture can be used.

Since Chapter 3 showed multiple successful thermite compositions, it opened the door to a wide number of thermite compositions. Rather than experimentally validate every possible existing composition, Chapter 6 uses NASA CEAM to simulate the aluminum-based thermite reaction for a wide range of compositions. A series of plots relating temperature, fuel composition, and O/F ratio can be seen in Chapter 6. This provides a guidance when creating future thermite compositions in regards both maximum temperature and reaction rate. This work, when combined with the printing results seen throughout the dissertation, can be used to create printable thermite compositions with properties tailored by chemical composition and by architecture.

Future Work

Additive Manufacturing

The most unique advancements in additive manufacturing initially discussed in this work are the multi-material printing from a single syringe and the printing of larger structures and structures with higher aspect ratios. Work is still needed in fully quantifying the fluid flow behavior of multiple materials within a single syringe. Changes in syringe design, material viscosity, and syringe coating would result in different fluid flows within the syringe. Changing these parameters could eliminate or elongate the intermediate mixed material phase, depending on the goals of the user. This is in addition to efforts in creating and studying architectures that utilize multiple materials in a single structure. Any work in creating larger or more complex structure would be beneficial, as it would expand the range of potential architectures. Efforts applying in-process height monitoring and other techniques used in concrete 3D printing would likely quickly be proven successful due to the similarities of the materials. The printing limits of this material have only begun to be explored, and advancements in similar AM techniques could be applied.

Thermite Compositions

The thermite compositions used in this work were limited to aluminum- or titanium-based oxidizers, with iron oxide as the primary considered fuel. However, these materials were not selected for specific reaction behavior. They were selected because they're easy to obtain and the resulting thermite mixtures are generally considered safe to handle. There is a wide variety of valid thermite compositions that could be selected for other specific properties, like gas

production or ease of ignition. These new reaction properties will affect processing parameters, but overall could result in new mixtures with new applications. For example, much of the work in this dissertation could be repeated with copper oxide as a fuel, resulting in different reaction rates, maximum temperatures, and architectural behavior. These new behaviors could be used in conjunction with chemical equilibrium software to eventually begin to model or predict some of this new behavior. Ideally, a series of guidelines will be established for designing architectures for similar thermite compositions.

Joining Applications

Joining in austere or remote environments has always been a challenge, but thermite-based RMA's present a potential solution. Any efforts in characterizing heat deposition with respect to individual compositions or specific architectures would greatly advance the joining capabilities. In addition to specific heat generation and deposition characteristics, this work can be combined with existing welding and joining knowledge to study the effects of rapid heating and cooling on the relevant joint. Any work in more application-specific joints would also be valuable. Studies could be conducted using larger masses of thermite to conduct field repair or field expedient armoring. This research was limited to smaller masses of thermite for safety reasons, but larger masses of thermite could be used in higher temperature joining techniques.

REFERENCES

[1]S.H. Fischer MCG. A Survey of Combustible Metals, Thermites, and Intermetallics for Pyrotechnic Applications. AIAA/ASME/SAE/ASEE Jt. Propuls. Conf., 1996.

[2]Calignano F, Manfredi D, Ambrosio EP, Biamino S, Lombardi M, Atzeni E, et al. Overview on additive manufacturing technologies. Proc IEEE 2017;105:593–612. doi:10.1109/JPROC.2016.2625098.

[3]Varotsis AB. Introduction to Binder Jetting 3D printing. 3D Hubs 2017:1–13. https://www.3dhubs.com/knowledge-base/introduction-binder-jetting-3d-printing/.

[4]Miyanaji H, Zhang S, Lassell A, Zandinejad A, Yang L. Process Development of Porcelain Ceramic Material with Binder Jetting Process for Dental Applications. Jom 2016;68:831–41. doi:10.1007/s11837-015-1771-3.

[5]Miyanaji H, Yang L, Zhang S, Zandinejad A. A preliminary study of the graded dental porcelain ceramic structures fabricated via binder jetting 3D printing. Solid Free Fabr Symp 2014:578–89.

[6]Snelling DA, Williams CB, Suchicital CTA, Druschitz AP. Binder jetting advanced ceramics for metal-ceramic composite structures. Int J Adv Manuf Technol 2017;92:531–45. doi:10.1007/s00170-017-0139-y.

[6]Varotsis AB. Introduction to Binder Jetting 3D printing. 3D Hubs 2017:1–13. https://www.3dhubs.com/knowledge-base/introduction-binder-jetting-3d-printing/.

[7]USE INSTRUCTIONS AND FAQ. 2/26/2020. https://www.thevirtualfoundry.com/help.

[8]Varotsis AB. Introduction to Material Jetting 3D Printing 2019:1–12.

[9]Carl B, Brook S. United States patent钻石打标专利. Geothermics 1985;14:595–9.

doi:10.1016/0375-6505(85)90011-2.

[10]Lewis JA. Direct ink writing of 3D functional materials. Adv Funct Mater 2006;16:2193–204. doi:10.1002/adfm.200600434.

[11]Ahn BY, Walker SB, Slimmer SC, Russo A, Gupta A, Kranz S, et al. Planar and three-dimensional printing of conductive inks. J Vis Exp 2011:1–8. doi:10.3791/3189.

[12]Wei TS, Ahn BY, Grotto J, Lewis JA. 3D Printing of Customized Li-Ion Batteries with Thick Electrodes. Adv Mater 2018;30:1–7. doi:10.1002/adma.201703027.

[13]Truby RL, Lewis JA. Printing soft matter in three dimensions. Nature 2016;540:371–8. doi:10.1038/nature21003.

[14]Sochol RD, Sweet E, Glick CC, Venkatesh S, Avetisyan A, Ekman KF, et al. 3D printed microfluidic circuitry via multijet-based additive manufacturing. Lab Chip 2016;16:668–78. doi:10.1039/c5lc01389e.

[15]Jakus AE, Taylor SL, Geisendorfer NR, Dunand DC, Shah RN. Metallic Architectures from 3D-Printed Powder-Based Liquid Inks. Adv Funct Mater 2015. doi:10.1002/adfm.201503921.

[16]Jakus AE, Koube KD, Geisendorfer NR, Shah RN. Robust and Elastic Lunar and Martian Structures from 3D-Printed Regolith Inks. Sci Rep 2017;7:44931. doi:10.1038/srep44931.

[17]Lewis JA, Smay JE, Stuecker J, Cesarano J. Direct ink writing of three-dimensional ceramic structures. J Am Ceram Soc 2006;89:3599–609. doi:10.1111/j.1551-2916.2006.01382.x.

[18]Khoshnevis B. Automated construction by contour crafting - Related robotics and information technologies. Autom Constr 2004;13:5–19. doi:10.1016/j.autcon.2003.08.012.

[19]Wolfs R, Bos F, van Strien E, Salet T. A Real-Time Height Measurement and Feedback System for 3D Concrete Printing. High Tech Concr Where Technol Eng Meet - Proc 2017 Fib Symp 2017;1:v. doi:10.1007/978-3-319-59471-2.

[20]Lim S, Buswell RA, Le TT, Austin SA, Gibb AGF, Thorpe T. Developments in construction-scale additive manufacturing processes. Autom Constr 2012. doi:10.1016/j.autcon.2011.06.010.

[21]Panda B, Paul SC, Mohamed NAN, Tay YWD, Tan MJ. Measurement of tensile bond strength of 3D printed geopolymer mortar. Meas J Int Meas Confed 2018;113:108–16. doi:10.1016/j.measurement.2017.08.051.

[22]Sullivan KT, Zhu C, Duoss EB, Gash AE, Kolesky DB, Kuntz JD, et al. Controlling Material Reactivity Using Architecture. Adv Mater 2016;28:1934–9. doi:10.1002/adma.201504286.

[23]Murray AK, Isik T, Ortalan V, Gunduz IE, Son SF, Chiu GTC, et al. Two-component additive manufacturing of nanothermite structures via reactive inkjet printing. J Appl Phys 2017;122:1–6. doi:10.1063/1.4999800.

[24]Ruz-Nuglo FD, Groven LJ. 3-D Printing and Development of Fluoropolymer Based Reactive Inks. Adv Eng Mater 2018. doi:10.1002/adem.201700390.

[25]Fleck TJ, Murray AK, Gunduz IE, Son SF, Chiu GTC, Rhoads JF. Additive manufacturing of multifunctional reactive materials. Addit Manuf 2017:176–82. doi:10.1016/j.addma.2017.08.008.

[26]Huang C, Jian G, De Lisio JB, Wang H, Zachariah MR. Electrospray deposition of energetic polymer nanocomposites with high mass particle loadings: A prelude to 3D printing of rocket motors. Adv Eng Mater 2015;17:95–101. doi:10.1002/adem.201400151.

[27]Chandru RA, Balasubramanian N, Oommen C, Raghunandan BN. Additive manufacturing of solid rocket propellant grains. J Propuls Power 2018;34:1090–3. doi:10.2514/1.B36734.

[28]McClain MS, Gunduz IE, Son SF. Additive manufacturing of ammonium perchlorate composite propellant with high solids loadings. Proc Combust Inst 2019;37:3135–42. doi:10.1016/j.proci.2018.05.052.

[29]Lonsdale CP. Thermite rail welding: history process developments, current practice and outlook for the 21st century. Proc AREMA 1999 Annu Conf 1999;1895:18. doi:http://citeseerx.ist.psu.edu/viewdoc/download?doi=10.1.1.546.5448&rep=rep1&type=pdf.

[30]Cirino Z. Exothermic Welding 2011:2–6.

[31]ASM (International). Van Nostrand's Sci. Encycl., 2005. doi:10.1002/0471743984.vse0687.

[32]Weare NE, Long RA. Exothermically Brazed Hydraulic Fittings for Aircraft. Proc. AWS Natl. Fall Meet., 1966, p. 28–38.

[33]Masubuchi, K., Anderssen, A. H. (1973, January 1). Underwater Application Of Exothermic Welding. Offshore Technology Conference. doi:10.4043/1910-MS

[34]Siewert TA, Heine RW, Adams CM, Williams JR. The Skylab Brazing Experiment. Weld J 1977.

APPENDIX A: G-CODE

The following is selected g-code files. All g-code shown here was written by the author, not generated by a commercial slicing software.

3 Layer Circle

```
M104 T10  S0
G21     ; use millimeters
G90     ; absolute coordinates
G0 Z5 ; lift head to avoid collisions
G28 X0 Y0 ; home X and Y
G92 X0 Y0 ; reset origin: X and Y
G0 X0 Y0   ; move to desired origin
G92 X0 Y0 ; reset origin: X and Y
M83          ; relative extruder coordinates
;M109 S0  ;wait for temperture to come up.
M756 S0.5  ;set flow for the first layer please

G21 ; set units to millimeters
G90 ; use absolute coordinates
M82 ; use absolute distances for extrusion
G92 E0 ; reset extrusion distance
G01 X10.000 Y10.000 Z2 F500

G01 X80 Y120 Z0 F500; layered circles, changing layer height
G02 X80 Y120 Z0 I13.5 J0 F500
G02 X80 Y120 Z2 I13.5 J0;1.8 mm layer height
G02 X80 Y120 Z4 I13.5 J0;1.8
G02 X80 Y120 Z6 I13.5 J0;1.8

G0 X20 Y20 Z0

G92 E0 ; reset extrusion distance
M107 ; disable fan
M107 T10  ; turn off fans and lasers
M104 S0    ; turn off temperature
M140 S0   ;turn off the hot bed.
G91          ;
G1 Z5.0      ; Drop bed 5mm for extra clearance
G90          ; absolute
G28 X0 Y0  ; home X axis
G92 X0 Y0 ; confirm we are at zero
M84          ; disable motors
M30          ; End ofprogra
```

High Aspect Ratio Wall

```
G0 X0 Y0   ; move to desired origin
G92 X0 Y0 ; reset origin: X and Y
M83         ; relative extruder coordinates
;M109 S0  ;wait for temperture to come up.
M756 S0.5  ;set flow for the first layer please

G21 ; set units to millimeters
G90 ; use absolute coordinates
M82 ; use absolute distances for extrusion
G92 E0 ; reset extrusion distance
G01 X10.000 Y10.000 Z2 F500

G01 X80 Y120 Z0 F500; layered circles, changing layer height

M104 T10  S0
G21     ; use millimeters
G90     ; absolute coordinates
G0 Z5 ; lift head to avoid collisions
G28 X0 Y0 ; home X and Y
G92 X0 Y0 ; reset origin: X and Y
G0 X0 Y0   ; move to desired origin
G92 X0 Y0 ; reset origin: X and Y
M83         ; relative extruder coordinates
;M109 S0  ;wait for temperture to come up.
M756 S0.5  ;set flow for the first layer please

G21 ; set units to millimeters
G90 ; use absolute coordinates
M82 ; use absolute distances for extrusion
G92 E0 ; reset extrusion distance
G01 X10.000 Y10.000 Z2 F500

G01 X70 Y120 Z0 F500; l
G01 X0 Y120;
G01 X70 Y120;
G01 X70 Y120 Z1.8; LAYER 1 COMPLETED
G01 X0 Y120;
G01 X0 Y120 Z3.6; LAYER 2 COMPLETED
G01 X70 Y120;
G01 X70 Y120 Z5.4; LAYER 3 COMPLETED
G01 X0 Y120;
G01 X0 Y120 Z7.2; LAYER 4 COMPLETED
G01 X70 Y120;
G01 X70 Y120 Z9.0; LAYER 5 COMPLETED
```

```
G01 X0 Y120;
G01 X0 Y120 Z10.8; LAYER 6 COMPLETED
G01 X70 Y120;
G01 X70 Y120 Z12.6; LAYER 7 COMPLETED
G01 X0 Y120;
G01 X0 Y120 Z14.4; LAYER 8 COMPLETED
G01 X70 Y120;
G01 X70 Y120 Z16.2; LAYER 9 COMPLETED
G01 X0 Y120;
G01 X0 Y120 Z18; LAYER 10 COMPLETED
G01 X70 Y120;
G01 X70 Y120 Z19.8; LAYER 11 COMPLETED
G01 X0 Y120;
G01 X0 Y120 Z21.6; LAYER 12 COMPLETED
G01 X70 Y120;
G01 X70 Y120 Z23.4; LAYER 13 COMPLETED
G01 X0 Y120;
G01 X0 Y120 Z25.2; LAYER 14 COMPLETED
G01 X70 Y120;
G01 X70 Y120 Z27; LAYER 15 COMPLETED
G01 X0 Y120;
G01 X0 Y120 Z28.8; LAYER 16 COMPLETED
G01 X70 Y120;
G01 X70 Y120 Z30.6; LAYER 17 COMPLETED
G01 X0 Y120;
G01 X0 Y120 Z32.4; LAYER 18 COMPLETED
G01 X70 Y120;
G01 X70 Y120 Z34.2; LAYER 19 COMPLETED
G01 X0 Y120;
G01 X0 Y120 Z36; LAYER 20 COMPLETED
G01 X70 Y120;
G01 X70 Y120 Z37.8; LAYER 21 COMPLETED
G01 X0 Y120;
G01 X0 Y120 Z39.6; LAYER 22 COMPLETED
G01 X70 Y120;
G01 X70 Y120 Z41.4; LAYER 23 COMPLETED
G01 X0 Y120;
G01 X0 Y120 Z43.2; LAYER 24 COMPLETED
G01 X70 Y120;
G01 X70 Y120 Z45; LAYER 25 COMPLETED
G01 X0 Y120;
G01 X0 Y120 Z46.8; LAYER 26 COMPLETED
G01 X70 Y120;
G01 X70 Y120 Z48.6; LAYER 27 COMPLETED
G01 X0 Y120;
G01 X0 Y120 Z50.4; LAYER 28 COMPLETED
```

```
G01 X70 Y120;
G01 X70 Y120 Z52.2; LAYER 29 COMPLETED
G01 X0 Y120;
G01 X0 Y120 Z54; LAYER 30 COMPLETED
G01 X70 Y120;
G01 X70 Y120 Z55.8; LAYER 31 COMPLETED
G01 X0 Y120;
G01 X0 Y120 Z57.6; LAYER 32 COMPLETED
G01 X70 Y120;
G01 X70 Y120 Z59.4; LAYER 33 COMPLETED
G01 X0 Y120;
G01 X0 Y120 Z61.2; LAYER 34 COMPLETED
G01 X70 Y120;
G01 X70 Y120 Z63; LAYER 35 COMPLETED
G01 X0 Y120;
G01 X0 Y120 Z64.8; LAYER 36 COMPLETED
G01 X70 Y120;
G01 X70 Y120 Z66.6; LAYER 37 COMPLETED (THE DEVIL'S LAYER)
G01 X0 Y120;
G01 X0 Y120 Z68.4; LAYER 38 COMPLETED
G01 X70 Y120;
G01 X70 Y120 Z70.2; LAYER 39 COMPLETED
G01 X0 Y120;
G01 X0 Y120 Z72; LAYER 40 COMPLETED
G01 X70 Y120;
G01 X70 Y120 Z73.8; LAYER 41 COMPLETED
G01 X0 Y120;
G01 X0 Y120 Z75.6; LAYER 42 COMPLETED
G01 X70 Y120;
G01 X70 Y120 Z77.4; LAYER 43 COMPLETED
G01 X0 Y120;
G01 X0 Y120 Z79.2; LAYER 44 COMPLETED
G01 X70 Y120;
G01 X70 Y120 Z81; LAYER 45 COMPLETED
G01 X0 Y120;
G01 X0 Y120 Z82.8; LAYER 46 COMPLETED
G01 X70 Y120;
G01 X70 Y120 Z84.6; LAYER 47 COMPLETED
G01 X0 Y120;
G01 X0 Y120 Z86.4; LAYER 48 COMPLETED
G01 X70 Y120;
G01 X70 Y120 Z88.2; LAYER 49 COMPLETED
G01 X0 Y120;
G01 X0 Y120 Z90; LAYER 50 COMPLETED
G01 X70 Y120;
G01 X70 Y120 Z91.8; LAYER 51 COMPLETED
```

```
G01 X0 Y120;
G01 X0 Y120 Z93.6; LAYER 52 COMPLETED
G01 X70 Y120;
G01 X70 Y120 Z95.4; LAYER 53 COMPLETED
G01 X0 Y120;
G01 X0 Y120 Z97.2; LAYER 54 COMPLETED
G01 X70 Y120;
G01 X70 Y120 Z99; LAYER 55 COMPLTED
G01 X0 Y120;
G01 X0 Y120 Z100.8; LAYER 56 COMPLETED
G01 X70 Y120;
G01 X70 Y120 Z102.6; LAYER 57 COMPLETED
G01 X0 Y120;
G01 X0 Y120 Z104.4; LAYER 58 COMPLETED
G01 X70 Y120;
G01 X70 Y120 Z106.2; LAYER 59 COMPLETED
G01 X0 Y120;
G01 X0 Y120 Z108; LAYER 60 COMPLETED
G01 X70 Y120;
G01 X70 Y120 Z109.8; LAYER 61 COMPLETED
G01 X0 Y120;
G01 X0 Y120 Z111.6; LAYER 62 COMPLETED
G01 X70 Y120;
G01 X70 Y120 Z113.4; LAYER 63 COMPLETED
G01 X0 Y120;
G01 X0 Y120 Z115.2; LAYER 64 COMPLETED
G01 X70 Y120;
G01 X70 Y120 Z117; LAYER 65 COMPLETED
G01 X0 Y120;
G01 X0 Y120 Z118.8; LAYER 66 COMPLETED
G01 X70 Y120;
G01 X70 Y120 Z120.6; LAYER 67 COMPLETED
G01 X0 Y120;
G01 X0 Y120 Z122.4; LAYER 68 COMPLETED
G01 X70 Y120;
G01 X70 Y120 Z124.2; LAYER 69 COMPLETED
G01 X0 Y120;
G01 X0 Y120 Z126; LAYER 70 COMPLETED
G01 X70 Y120;
G01 X70 Y120 Z127.8; LAYER 71 COMPLETED
G01 X0 Y120;
G01 X0 Y120 Z129.6; LAYER 73 COMPLETED
G01 X70 Y120;
G01 X70 Y120 Z131.4; LAYER 74 COMPLTED
G01 X0 Y120;
G01 X0 Y120 Z133.2; LAYER 75 COMPLETED
```

```
G01 X70 Y120;
G01 X70 Y120 Z135; LAYER 76 COMPLETED
G01 X0 Y120;
G01 X0 Y120 Z136.8;
G01 X70 Y120;
G01 X70 Y120 Z138.6;
G01 X0 Y120;
G01 X0 Y120 Z140.4;
G01 X70 Y120;
G01 X70 Y120 Z142.2;
G01 X0 Y120;
G01 X0 Y120 Z144;
G01 X70 Y120;
G01 X70 Y120 Z145.8;
G01 X0 Y120;
G01 X0 Y120 Z147.6;
G01 X70 Y120;
G01 X70 Y120 Z149.4;
G01 X0 Y120;
G01 X0 Y120 Z151.2;

G92 E0 ; reset extrusion distance
M107 ; disable fan
M107 T10  ; turn off fans and lasers
M104 S0    ; turn off temperature
M140 S0   ;turn off the hot bed.
G91          ;
G1 Z5.0     ; Drop bed 5mm for extra clearance
G90          ; absolute
G28 X0 Y0  ; home X axis
G92 X0 Y0 ; confirm we are at zero
M84          ; disable motors
M30          ; End ofprogram
```

Layered Print for Soldering

```
M104 T10  S0
G21     ; use millimeters
G90     ; absolute coordinates
G0 Z5 ; lift head to avoid collisions
G28 X0 Y0 ; home X and Y
G92 X0 Y0 ; reset origin: X and Y
G0 X0 Y0   ; move to desired origin
G92 X0 Y0 ; reset origin: X and Y
M83          ; relative extruder coordinates
;M109 S0  ;wait for temperture to come up.
M756 S0.5  ;set flow for the first layer please

G21 ; set units to millimeters
G90 ; use absolute coordinates
M82 ; use absolute distances for extrusion
G92 E0 ; reset extrusion distance
G0 Z5
G0 X80.000 Y100.000     F2500

G0 Z0.5 F250

;LAYER 1 POSITION 2
G1 X10 Y90 Z0
G1 X60 Y90
G1 X60 Y92.4
G1 X10 Y92.4
G1 X10 Y94.8
G1 X60 Y94.8
G1 X62.4 Y94.8
G1 X62.4 Y90

;LAYER 2 POSITION 2
G1 X10 Y90 Z1.4
G1 X60 Y90
G1 X60 Y92.4
G1 X10 Y92.4
G1 X10 Y94.8
G1 X60 Y94.8
G1 X62.4 Y94.8
G1 X62.4 Y90


G92 E0 ; reset extrusion distance
M107 ; disable fan
```

```
M107 T10  ; turn off fans and lasers
M104 S0    ; turn off temperature
M140 S0   ;turn off the hot bed.
G91          ;
G1 Z5.0      ; Drop bed 5mm for extra clearance
G90          ; absolute
G28 X0 Y0  ; home X axis
G92 X0 Y0 ; confirm we are at zero
M84          ; disable motors
M30          ; End ofprogram
```

Army Star

```
M104 T10  S0
G21     ; use millimeters
G90     ; absolute coordinates
G0 Z5 ; lift head to avoid collisions
G28 X0 Y0 ; home X and Y
G92 X0 Y0 ; reset origin: X and Y
G0 X0 Y0   ; move to desired origin
G92 X0 Y0 ; reset origin: X and Y
M83          ; relative extruder coordinates
;M109 S0  ;wait for temperture to come up.
M756 S0.5  ;set flow for the first layer please


G21 ; set units to millimeters
G90 ; use absolute coordinates
M82 ; use absolute distances for extrusion
G92 E0 ; reset extrusion distance
G0 Z5
G0 X80.000 Y100.000     F2500

G0 Z0.5 F250

G1 X48.5 Y134.25 Z0.00
G1 X58.25 Y102.75
G1 X32.25 Y81.75
G1 X64.25 Y81.75
G1 X74 Y52.25
G1 X84 Y81.75
G1 X117.5 Y81.75
G1 X92 Y102.75
G1 X101.25 Y134.25
G1 X74 Y115.25
G1 X46 Y138
G1 X56 Y104
G1 X27.5 Y79.5
G1 X63.25 Y79.5
G1 X74 Y48
G1 X84 Y79.5
G1 X122 Y79.5
G1 X94.5 Y103.5
G1 X104 Y138
G1 X74 Y117.5
G1 X46 Y138
```

```
G1 X48.5 Y134.25 Z1.4
G1 X58.25 Y102.75
G1 X32.25 Y81.75
G1 X64.25 Y81.75
G1 X74 Y52.25
G1 X84 Y81.75
G1 X117.5 Y81.75
G1 X92 Y102.75
G1 X101.25 Y134.25
G1 X74 Y115.25
G1 X46 Y138
G1 X56 Y104
G1 X27.5 Y79.5
G1 X63.25 Y79.5
G1 X74 Y48
G1 X84 Y79.5
G1 X122 Y79.5
G1 X94.5 Y103.5
G1 X104 Y138
G1 X74 Y117.5
G1 X46 Y138

G1 X48.5 Y134.25 Z2.8
G1 X58.25 Y102.75
G1 X32.25 Y81.75
G1 X64.25 Y81.75
G1 X74 Y52.25
G1 X84 Y81.75
G1 X117.5 Y81.75
G1 X92 Y102.75
G1 X101.25 Y134.25
G1 X74 Y115.25
G1 X46 Y138
G1 X56 Y104
G1 X27.5 Y79.5
G1 X63.25 Y79.5
G1 X74 Y48
G1 X84 Y79.5
G1 X122 Y79.5
G1 X94.5 Y103.5
G1 X104 Y138
G1 X74 Y117.5
G1 X46 Y138

G92 E0 ; reset extrusion distance
```

```
M107 ; disable fan
M107 T10  ; turn off fans and lasers
M104 S0    ; turn off temperature
M140 S0   ;turn off the hot bed.
G91          ;
G1 Z5.0      ; Drop bed 5mm for extra clearance
G90          ; absolute
G28 X0 Y0  ; home X axis
G92 X0 Y0 ; confirm we are at zero
M84          ; disable motors
M30          ; End ofprogram
```

VUWAL

```
M104 T10  S0
G21     ; use millimeters
G90     ; absolute coordinates
G0 Z5 ; lift head to avoid collisions
G28 X0 Y0 ; home X and Y
G92 X0 Y0 ; reset origin: X and Y
G0 X0 Y0   ; move to desired origin
G92 X0 Y0 ; reset origin: X and Y
M83          ; relative extruder coordinates
;M109 S0  ;wait for temperture to come up.
M756 S0.5  ;set flow for the first layer please


G21 ; set units to millimeters
G90 ; use absolute coordinates
M82 ; use absolute distances for extrusion
G92 E0 ; reset extrusion distance
G0 Z5
G0 X80.000 Y100.000     F2500

G0 Z0.5 F250

G1 X10.000 Y60.000 Z0.0
G1 X17.600 Y60.000
G1 X10.000 Y110.000
G1 X12.400 Y110.000
G1 X20.000 Y62.400
G1 X27.600 Y110.000
G1 X30.000 Y110.000
G1 X22.400 Y60.000
G1 X42.600 Y60.000
G1 X37.000 Y70.000
G1 X37.000 Y110.000
G1 X39.400 Y110.000
G1 X39.400 Y72.400
G1 X45.000 Y64.800
G1 X50.600 Y72.400
G1 X50.600 Y110.000
G1 X53.000 Y110.000
G1 X53.000 Y70.000
G1 X47.400 Y60.000
G1 X67.000 Y60.000
G1 X60.000 Y110.000
G1 X62.400 Y110.000
```

G1 X69.400 Y70.000
G1 X73.000 Y85.000
G1 X76.600 Y70.000
G1 X81.200 Y110.000
G1 X83.600 Y110.000
G1 X78.400 Y60.000
G1 X90.000 Y60.000
G1 X97.600 Y110.000
G1 X100.000 Y110.000
G1 X107.600 Y60.000
G1 X115.000 Y60.000
G1 X115.000 Y110.000
G1 X117.400 Y110.000
G1 X117.400 Y62.400
G1 X127.400 Y62.400
G1 X127.400 Y60.000
G1 X135.000 Y60.000
G1 X135.000 Y57.600
G1 X7.600 Y57.600
G1 X7.600 Y60.000

G1 X10.000 Y60.000 Z1.4
G1 X17.600 Y60.000
G1 X10.000 Y110.000
G1 X12.400 Y110.000
G1 X20.000 Y62.400
G1 X27.600 Y110.000
G1 X30.000 Y110.000
G1 X22.400 Y60.000
G1 X42.600 Y60.000
G1 X37.000 Y70.000
G1 X37.000 Y110.000
G1 X39.400 Y110.000
G1 X39.400 Y72.400
G1 X45.000 Y64.800
G1 X50.600 Y72.400
G1 X50.600 Y110.000
G1 X53.000 Y110.000
G1 X53.000 Y70.000
G1 X47.400 Y60.000
G1 X67.000 Y60.000
G1 X60.000 Y110.000
G1 X62.400 Y110.000
G1 X69.400 Y70.000
G1 X73.000 Y85.000
G1 X76.600 Y70.000

G1 X81.200 Y110.000
G1 X83.600 Y110.000
G1 X78.400 Y60.000
G1 X90.000 Y60.000
G1 X97.600 Y110.000
G1 X100.000 Y110.000
G1 X107.600 Y60.000
G1 X115.000 Y60.000
G1 X115.000 Y110.000
G1 X117.400 Y110.000
G1 X117.400 Y62.400
G1 X127.400 Y62.400
G1 X127.400 Y60.000
G1 X135.000 Y60.000
G1 X135.000 Y57.600
G1 X7.600 Y57.600
G1 X7.600 Y60.000

G1 X10.000 Y60.000 Z2.8
G1 X17.600 Y60.000
G1 X10.000 Y110.000
G1 X12.400 Y110.000
G1 X20.000 Y62.400
G1 X27.600 Y110.000
G1 X30.000 Y110.000
G1 X22.400 Y60.000
G1 X42.600 Y60.000
G1 X37.000 Y70.000
G1 X37.000 Y110.000
G1 X39.400 Y110.000
G1 X39.400 Y72.400
G1 X45.000 Y64.800
G1 X50.600 Y72.400
G1 X50.600 Y110.000
G1 X53.000 Y110.000
G1 X53.000 Y70.000
G1 X47.400 Y60.000
G1 X67.000 Y60.000
G1 X60.000 Y110.000
G1 X62.400 Y110.000
G1 X69.400 Y70.000
G1 X73.000 Y85.000
G1 X76.600 Y70.000
G1 X81.200 Y110.000
G1 X83.600 Y110.000
G1 X78.400 Y60.000

```
G1 X90.000 Y60.000
G1 X97.600 Y110.000
G1 X100.000 Y110.000
G1 X107.600 Y60.000
G1 X115.000 Y60.000
G1 X115.000 Y110.000
G1 X117.400 Y110.000
G1 X117.400 Y62.400
G1 X127.400 Y62.400
G1 X127.400 Y60.000
G1 X135.000 Y60.000
G1 X135.000 Y57.600
G1 X7.600 Y57.600
G1 X7.600 Y60.000



G92 E0 ; reset extrusion distance
M107 ; disable fan
M107 T10  ; turn off fans and lasers
M104 S0    ; turn off temperature
M140 S0   ;turn off the hot bed.
G91          ;
G1 Z5.0      ; Drop bed 5mm for extra clearance
G90          ; absolute
G28 X0 Y0  ; home X axis
G92 X0 Y0 ; confirm we are at zero
M84          ; disable motors
M30          ; End ofprogram
```